

COMPUTATIONAL MODELING OF HIGH FREQUENCY COMBUSTION  
INSTABILITY IN A SINGLE-ELEMENT LIQUID ROCKET ENGINE

A Thesis

Submitted to the Faculty

of

Purdue University

by

Randolph Jedediah Smith

In Partial Fulfillment of the

Requirements for the Degree

of

Master of Science in Engineering

August 2006

Purdue University

West Lafayette, Indiana

To my wonderful wife and loving parents

## ACKNOWLEDGMENTS

I would first like to thank Dr. Charles Merkle, my advisor, and Dr. Venke Sankaran for their continual guidance during this research. They were instrumental in helping this research progress and I am very appreciative of their support. I owe a great deal to Matt Ellis, who worked on this project before me. His hard work laid the foundation for the research in this thesis. I would like to thank Dr. Guoping Xia for helping me to understand the computational model and for his continual assistance with coding issues. I am also grateful to the combustion instability group that was formed this past year under Dr. Sankaran, which included Dr. William Anderson, Jim Sisco, Enrique Portillo, and Yen Yu. The weekly meetings and constant collaboration greatly increased my understanding of combustion instability. It was also very helpful to see the many approaches that are possible for dealing with this difficult problem. I would like to thank Kevin Miller and everyone else that worked on the Purdue instability experiments on which the computational model is based. This research would not be nearly as useful or enjoyable without a successful experiment to compare my results with. I want to thank Dr. Steven Heister for his instruction in the classroom and for serving on my committee. I would also like to thank Dr. John Abraham and Dr. Carl Wassgren for adding to my understanding of propulsion. This research would not be possible without the NASA Constellation University Institutes Project. I want to thank Claudia Meyer and Jeff Rybak for managing that program and for their interest in this research.

## TABLE OF CONTENTS

	Page
LIST OF TABLES .....	vii
LIST OF FIGURES .....	viii
ABSTRACT .....	xv
CHAPTER 1. INTRODUCTION .....	1
1.1. Combustion Instability in Rocket Engines.....	1
1.1.1. Rayleigh’s Criterion .....	2
1.1.2. Types of Instability .....	5
1.1.3. Acoustic Mode Analysis.....	6
1.1.4. Heat Release Mechanisms and Response Functions .....	9
1.2. Modeling Approaches .....	11
1.2.1. Generalized Wave Equation Analysis.....	12
1.2.2. Euler/RANS Computations .....	14
1.2.3. Detailed Unsteady Dynamics Computations .....	14
1.3. Purdue Single-Element Combustion Instability Experiment.....	16
1.3.1. Experimental Objectives and Design Considerations .....	16
1.3.2. Experimental Configuration .....	19
1.3.3. Discussion of Experimental Results .....	22
1.4. Study Objectives and Outline .....	26
CHAPTER 2. COMPUTATIONAL MODEL .....	29
2.1. Governing Equations .....	29
2.2. Source Term for Steady Combustion .....	31
2.3. Computational Domain .....	35
2.3.1. Geometry.....	35
2.3.2. Nozzle Configuration .....	38
2.3.3. Grid Placement and Convergence.....	40

	Page
2.3.4. Boundary Conditions .....	44
2.4. Inputs and Steady-State Solutions .....	45
2.5. Broadband Mass-flow Forcing .....	48
CHAPTER 3. SMALL AMPLITUDE, LINEAR FORCING .....	52
3.1. Cold Flow, Constant Area Duct Trials.....	52
3.1.1. Low Mach Number Verification.....	53
3.1.2. Effects of Mean Flow on Acoustic Modes .....	58
3.2. Low Mach number, Simplified Computational Model .....	66
3.2.1. Results of the Simplified Computational Model .....	67
3.2.2. Comparison with an Analytical Model.....	71
3.3. Full Computational Model Results .....	75
3.3.1. Results of the 25 inch Chamber Case .....	75
3.3.2. Variation of Frequency Resolution.....	82
3.3.3. Decay Studies .....	84
3.3.4. Results of the 15, 20, and 35 inch Chamber Cases .....	86
3.4. Acoustic Validation .....	93
3.4.1. Validation of the 25 inch Chamber Case .....	93
3.4.2. Validation of all Chamber Length Cases .....	97
CHAPTER 4. LARGE AMPLITUDE, NON-LINEAR FORCING .....	102
4.1. Results of Large Amplitude Forcing.....	102
4.1.1. 25 inch Chamber Case.....	103
4.1.2. Oscillation in the Throat Region.....	110
4.1.3. 15, 20, and 35 Inch Chamber Cases .....	113
4.2. Validation of Non-linear Results .....	115
4.2.1. Validation of the 25 inch Chamber Case .....	116
4.2.2. Validation of All Chamber Length Cases .....	118
CHAPTER 5. BOUNDARY CONDITION STUDIES.....	121
5.1. Traditional Boundary Conditions.....	122
5.1.1. Inflow Boundary Conditions.....	122
5.1.2. Outflow Boundary Conditions .....	123

	Page
5.2. Approximate Downstream Boundary Conditions .....	123
5.2.1. Choked Downstream Boundary ( $u' = 0$ ).....	124
5.2.2. Downstream Nozzle Admittance Boundary Condition .....	127
5.3. Upstream Boundary Condition and Source Term .....	131
5.3.1. Upstream Wall Boundary Condition.....	131
5.3.2. Oxidizer Mass Flow Source Formulation .....	132
5.3.3. Upstream Boundary Solution Comparisons.....	134
CHAPTER 6. INSTABILITY STUDIES USING RESPONSE FUNCTIONS .....	142
6.1. Simplified Response Function .....	142
6.2. Formulation of a Simple Heat Release Source.....	144
6.3. Application of the Response Function .....	146
6.3.1. Initial Trials with an Inflow Boundary .....	147
6.3.2. Results with an Injector Head-end Wall Boundary.....	149
6.4. Instability Validation.....	159
CHAPTER 7. SUMMARY AND CONCLUSIONS .....	163
7.1. Summary of Results .....	163
7.2. Recommendations for Future Work.....	166
LIST OF REFERENCES .....	168
APPENDICES	
Appendix A. Tabulated Acoustic Modes (for an Inflow BC) .....	172
Appendix B. Acoustic Analysis (for a Wall BC) .....	175

## LIST OF TABLES

Table	Page
Table 1-1: Summary of conditions and results for the Purdue experiment .....	22
Table 2-1: Input properties and conditions for the 25 inch chamber base case..	45
Table 2-2: Specific input properties for different chamber length cases .....	46
Table 2-3: Steady-state constant solutions in the injector and chamber regions for the 25 inch chamber case .....	48
Table 3-1 Analytical and computational modes for the constant area configuration .....	61
Table 3-2: Comparison between the analytical and simplified computational models for a 25 inch chamber length.....	71
Table 3-3: Acoustic modes for the 25 inch chamber case for frequency resolutions of 25, 50, and 100 Hz .....	83
Table 3-4 Mode comparison using the zero mean flow analytical model, the full computational model, and the experimental PSD plots .....	95
Table 3-5: Comparison of unstable modes as shown by the experiments and as predicted by the analytical and computation models .....	99
Appendix Table	
Table A.1 Acoustic modes up to 7000 Hz for a 15 inch chamber with an inflow boundary condition. Output locations are specified in Figure A.1.....	172
Table A.2 Acoustic modes up to 7000 Hz for a 20 inch chamber with an inflow boundary condition. Output locations are specified in Figure A.1.....	173
Table A.3 Acoustic modes up to 7000 Hz for a 25 inch chamber with an inflow boundary condition. Output locations are specified in Figure A.1.....	173
Table A.4 Acoustic modes up to 7000 Hz for a 35 inch chamber with an inflow boundary condition. Output locations are specified in Figure A.1.....	174
Table B.1 Acoustic modes up to 7000 Hz for a 15 inch chamber with a wall boundary condition. Output locations are specified in Figure A.1.....	175
Table B.2 Acoustic modes up to 7000 Hz for a 20 inch chamber with a wall boundary condition. Output locations are specified in Figure A.1.....	176
Table B.3 Acoustic modes up to 7000 Hz for a 25 inch chamber with a wall boundary condition. Output locations are specified in Figure A.1.....	177
Table B.4 Acoustic modes up to 7000 Hz for a 35 inch chamber with a wall boundary condition. Output locations are specified in Figure A.1.....	178

## LIST OF FIGURES

Figure	Page
Figure 1.1: Pressure and heat release oscillations that are exactly in-phase (left) and growth of the pressure oscillations over time due to this condition (right)	3
Figure 1.2: Pressure and heat release oscillations that are exactly out-of-phase (left) and decay of the pressure oscillations over time due to this condition (right)	3
Figure 1.3: The first (left) and second (right) pure longitudinal modes for a closed chamber, where pressure is shown in blue and velocity in red	8
Figure 1.4: The first (left) and second (right) pure tangential pressure modes	8
Figure 1.5: The first (left) and second (right) pure radial pressure modes	8
Figure 1.6: Combustion processes which may influence the heat release oscillations in liquid rocket engine systems <sup>9</sup>	10
Figure 1.7: Turbulent vorticity computation of flow exiting an injector element for $Re = 12000$ <sup>21</sup>	15
Figure 1.8: Acoustic coupling between the injector 1L mode and the chamber 2L mode at 2200 Hz. Oxidizer flow is represented with the green arrow while fuel flow is represented with red arrows. <sup>10</sup>	18
Figure 1.9: Gas centered, liquid swirl coaxial injector element, based on the Russian RD-170 <sup>10</sup>	19
Figure 1.10: Purdue experimental setup with a 25 inch chamber length. The locations of high frequency pressure transducers are specified with red dots. <sup>10</sup>	20
Figure 1.11: Picture of the fully instrumented configuration of the Purdue longitudinal experiment for the 15 inch chamber length <sup>10</sup>	21
Figure 1.12: Mean pressure (DC) and oscillating pressure (AC) traces for test 25D1r <sup>10</sup>	23
Figure 1.13: PSD plots for tests 10D1, 15D1, 20D1r, 25D1r, and 35D1 (early and late) <sup>11</sup>	25
Figure 2.1: The top plot shows the S distribution, as defined by Equation 2.11. The bottom plot shows the resultant temperature profile.	34
Figure 2.2: Computational domain shown with a proportional view of the geometry (top) and a radially stretched and dimensioned version of the geometry (bottom)	36
Figure 2.3: The output locations for frequency analysis, corresponding to axial positions of -6.82, 0.5, 2.5, 4.5, 7.5, 18.0, and 22.0 inches	37



Figure	Page
Figure 2.4: Comparison between nozzle geometry for the experiment (left) and the computational model (right). The experiment only has a converging section, while the computational model has both converging and diverging sections. ....	39
Figure 2.5: Steady-state solutions of velocity, pressure, temperature, and the oxidizer mass fraction for 250, 500, 1000, and 2500 grid points .....	41
Figure 2.6: FFT plot comparison for 500 and 1000 grid points for a 25 inch chamber at position 1. Broadband mass flow forcing was used at 0.01% of the mean mass flow-rate. ....	42
Figure 2.7: Mode shape comparisons for 950 Hz and 1650 Hz for 500 grid points (left) and 1000 grid points (right).....	43
Figure 2.8: Axial geometry of the computational domain.....	46
Figure 2.9: Steady-state solutions for the 25 inch chamber case .....	47
Figure 2.10: Pressure history at position 2 with broadband forcing at 0.01% of the mass flow-rate. The frequency interval is 50 Hz. ....	51
Figure 3.1: 25 inch straight duct configuration.....	53
Figure 3.2: FFT plot taken at various locations of the duct for small amplitude broadband forcing for a chamber length of 25 inches and a Mach number of 0.01 .....	54
Figure 3.3: FFT plot of small amplitude broadband forcing taken at the head end of the duct for a chamber length of 25 inches and a Mach number of 0.01 (left). To illustrate the frequency resolution of the broadband plot, a close-up view of the 1 <sup>st</sup> peak is shown in the right plot. ....	55
Figure 3.4: Mode shape plots for a closed/open constant area duct configuration with low Mach number ( $M = 0.01$ ) at 400 Hz, 1250 Hz, 2100 Hz, and 2950 Hz .....	56
Figure 3.5: Pressure (blue) and velocity (red) mode shapes at 1250 Hz (plots are at different amplitude scales).....	57
Figure 3.6: Pressure and velocity time traces at the injector head-end position. ....	58
Figure 3.7: FFT plot of a small amplitude broadband forced, 25 inch straight duct with a Mach number of 0.38, taken at various positions in the duct.....	59
Figure 3.8: FFT plot of a small amplitude broadband forced, 25 inch constant area duct with Mach numbers of 0.38 (left) and 0.01 (right), taken at the head end of the duct.....	60
Figure 3.9 Mode shape comparisons for the first mode of a low Mach number flow (left) and a higher Mach number flow (right).....	61
Figure 3.10: Mode shape comparisons for and second mode of a low Mach number flow (left) and a higher Mach number flow (right) .....	62
Figure 3.11: Pressure and velocity time traces for the second mode at the injector head-end for both the low and high Mach number cases.....	63
Figure 3.12: Output locations for pressure and velocity for the second mode (1100 Hz) for the high Mach number case .....	64
Figure 3.13: Pressure and velocity time traces at positions 1-4 (refer to figure 3.9) with small amplitude forcing at the second mode (1100 Hz) .....	65

Figure	Page
Figure 3.14: Simplified computational model with an outflow $u' = 0$ boundary condition and decreased Mach number flow .....	66
Figure 3.15: FFT plot of the simplified computational model forced with broadband small amplitude forcing. The chamber length is 25 inches. ....	67
Figure 3.16: First four mode shapes of the simplified computational model for single frequency small amplitude forcing and a 25 inch chamber length.....	69
Figure 3.17: Pressure and velocity mode shape comparison for the 1750 Hz mode .....	70
Figure 3.18: Pressure mode shapes using the analytical model (763 Hz, left) and the low Mach number, simplified computational model (750 Hz, right).....	72
Figure 3.19: Pressure mode shapes using the analytical model (1055 Hz, left) and the low Mach number, simplified computational model (1050 Hz, right) .....	73
Figure 3.20: Pressure mode shape comparison between the analytical model (at 1718 Hz, left) and the low Mach number, simplified computational model (1750 Hz, right).....	73
Figure 3.21: Velocity mode shape comparison between the analytical model (at 1718 Hz, left) and the low Mach number, simplified computational model (1750 Hz, right).....	74
Figure 3.22: FFT plot of the 25 inch chamber case with small amplitude broadband forcing at positions 1, 2, 3, and 5.....	76
Figure 3.23: Mode shape comparison for the mode indicated by position 1 (650 Hz) and the mode indicated by position 2 (750 Hz) .....	77
Figure 3.24: Mode shapes at 650 Hz, 950 Hz, 1650 Hz, and 2250 Hz for a 25 inch chamber .....	78
Figure 3.25: Pressure (blue) and velocity (red) mode shapes for a 25 inch chamber forced at 1650 Hz with small amplitude forcing .....	80
Figure 3.26: Mode shape comparison for the simplified computational model at 1750 Hz and the full computational model at 1650 Hz. The chamber length is 25 inches. ....	81
Figure 3.27: Growth and decay of pressure for forcing at 0.001% and 1650 Hz for a 25 inch chamber .....	84
Figure 3.28: Decay of the pressure oscillation for forcing at 0.001% and 1650 Hz .....	85
Figure 3.29: Exponential curve-fit for the conditions of Figure 3.28.....	85
Figure 3.30: FFT plot of the 15 inch chamber case forced with small amplitude, broadband mass flow forcing.....	86
Figure 3.31: Mode shapes at 800 Hz, 1450 Hz, 2300 Hz, and 2800 Hz for a 15 inch chamber .....	87
Figure 3.32: Pressure (blue) and velocity (red) mode shapes for a 15 inch chamber forced at 1450 Hz with small amplitude forcing .....	88
Figure 3.33: FFT plot of the 20 inch chamber case forced with small amplitude, broadband mass-flow forcing.....	88
Figure 3.34: Mode shapes at 700 Hz, 1150 Hz, 1950 Hz, and 2450 Hz for a 20 inch chamber .....	89

Figure	Page
Figure 3.35: Pressure (blue) and velocity (red) mode shapes for a 20 inch chamber forced at 1150 Hz with small amplitude forcing .....	90
Figure 3.36: FFT plot of the 35 inch chamber case forced with small amplitude, broadband mass-flow forcing.....	90
Figure 3.37: Mode shapes at 500 Hz, 800 Hz, 1250 Hz, and 1750 Hz for a 35 inch chamber .....	91
Figure 3.38: Pressure (blue) and velocity (red) mode shapes for a 35 inch chamber forced at 1750 Hz (early instability) and 1250 Hz (late instability) with small amplitude forcing.....	92
Figure 3.39: Comparison of the experimental PSD for test 25D1r (left) and the computational FFT (right) for a 25 inch chamber.....	94
Figure 3.40: P'rms experimental data points at transducer locations of test 25D1r at 1660 Hz are shown in red. The computational mode shape with small amplitude forcing at 1650 Hz for a 25 inch chamber is shown in blue. ....	96
Figure 3.41: Comparison of experimental and computational chamber modes for chamber lengths of 15, 20, 25, and 35 inches corresponding to tests 15D1, 20D1r, 25D1r, and 35D1 .....	98
Figure 3.42: Computational (blue) and experimental (red) pressure mode shape comparisons for the unstable modes corresponding to chamber lengths of 15, 20, 25, 35 inches. The 35 inch plots include early and late unstable frequencies. ....	100
Figure 4.1: PSD plot of the 25 inch chamber forced at 1650 Hz and 0.001% of the mass-flow rate .....	103
Figure 4.2: PSD plot of the 25 inch chamber forced at 1650 Hz and 1% of the mass-flow rate .....	104
Figure 4.3: PSD plot of the 25 inch chamber forced at 1650 Hz and 10% of the mass-flow rate .....	105
Figure 4.4: PSD plot of the 25 inch chamber forced at 1650 Hz and 50% of the mass-flow rate .....	106
Figure 4.5: Pressure history for a 25 inch chamber forced at 1650 Hz and 50% of the mean mass flow-rate .....	107
Figure 4.6: Comparison of pressure history traces for small (left) and large (right) amplitude forcing at 1650 Hz for a 25 inch chamber .....	108
Figure 4.7: Mode shapes forced at 1650 Hz and 0.1%, 10%, 20%, and 50%. .	109
Figure 4.8: Mach number plotted at the throat grid point for a 501 point grid with a mass flow forcing of 0.1%.....	111
Figure 4.9: Mach number plotted at the throat grid point for a 5001 point grid with a mass flow forcing of 0.1%.....	111
Figure 4.10: Mach number plotted at the throat grid point for a 5001 point grid with a mass flow forcing of 50% .....	112
Figure 4.11: The PSD plots at positions one, two, and five are shown below for chamber lengths of 15, 20, and 35 inches. Each is forced at its unstable frequency and at 50% of the mean mass flow-rate.....	113

Figure	Page
Figure 4.12: Mode shape results for 50% forcing of each chamber length (15, 20, and 35 inch) at the respective unstable frequency .....	114
Figure 4.13: Comparison of experimental (left) and computational (right) PSD plots for the 25 inch chamber case with 70% forcing applied to the computational mass flow at position two .....	116
Figure 4.14: Comparison between experimental (left) and computational (right) pressure history traces for a 25 inch chamber. The computations have been forced at 1650 Hz and 70% of the mean mass-flow rate. ....	117
Figure 4.15: Comparison between experimental data and the computational mode shape for 70% forcing.....	118
Figure 4.16: PSD experimental (left) and computational (right) plots for chamber lengths of 15 inches (1502 Hz), 20 inches (1184 Hz), and 25 inches (1660 Hz).....	119
Figure 4.17: PSD experimental (left) and computational (right) plots for the 35 inch chamber length for the early (1721 Hz) and late (1233 Hz) instabilities .....	120
Figure 5.1: FFT comparisons between the nozzle and $u' = 0$ boundary conditions at position 2 for small amplitude broadband forcing in a 25 inch chamber .	125
Figure 5.2: Mode shape comparison between $u' = 0$ boundary condition and the full nozzle configuration for a small amplitude forcing. ....	126
Figure 5.3: FFT comparison between the nozzle and $u' = 0$ boundary conditions at position 2 for high amplitude forcing at 1650 Hz with a 25 inch chamber length.....	127
Figure 5.4: Comparison between full nozzle, $u' = 0$ boundary condition, and nozzle admittance boundary condition for an FFT performed with linear broadband forcing at position 2 for a 25 inch chamber.....	128
Figure 5.5 Mode shape comparison between $u' = 0$ boundary condition and the admittance boundary condition for small amplitude forcing. ....	129
Figure 5.6: Comparison of nozzle configuration, $u' = 0$ boundary condition, and nozzle admittance condition for an FFT performed at position 2 with high amplitude forcing at 1650 Hz and a 25 inch chamber length.....	130
Figure 5.7: Schematic of the computational domain, showing the upstream wall boundary, the oxidizer source, and part of the chamber (the nozzle is not shown). The oxidizer source distribution is shown inside the injector for $\sigma = 0.964$ inches. ....	132
Figure 5.8: Axial geometry and output locations of the computational domain.	134
Figure 5.9: Steady-state velocity solutions (full domain and close-up) for an inflow boundary condition and for the oxidizer source/wall boundary configuration .....	135
Figure 5.10: Steady-state pressure solutions (full domain and close-up) for an inflow boundary condition and for the oxidizer source/wall boundary configuration .....	136

Figure	Page
Figure 5.11: Steady-state temperature solutions (full domain and close-up) for an inflow boundary condition and for the oxidizer source/wall boundary configuration .....	137
Figure 5.12: FFT plot of the 25 inch chamber case with broadband small amplitude forcing and the wall boundary/oxidizer source applied.....	137
Figure 5.13: Pressure mode shape comparison between the inflow boundary condition and the wall BC/source for small amplitude forcing at 750 Hz ....	138
Figure 5.14: Pressure mode shape comparison between the inflow boundary condition and the wall BC/source for small amplitude forcing at 1650 Hz ..	139
Figure 5.15: PSD plot of high amplitude (50%) forcing at 1650 Hz with a 25 inch chamber length.....	140
Figure 6.1: Schematic showing the heat release envelope at the injector/chamber interface. Note that the envelope shows both positive and negative heat release.....	145
Figure 6.2: Pressure history plot for an inflow boundary with small amplitude mass-flow forcing (first region), a response function applied (second region), and neither mass-flow forcing nor the response function applied (third region) .....	147
Figure 6.3: Pressure history plots for $\beta = 100$ (left) showing decay, and $\beta = 2000$ (right) showing growth and limit cycle behavior .....	148
Figure 6.4: Variation of beta values for an upstream wall boundary condition, resulting in 1) decay, 2) 'converged' conditions, 3) growth and limit cycle, 4) numerical divergence .....	150
Figure 6.5: Growth and limit cycle due to the application of the response function. The chamber length is 25 inches, $\beta = 2050$ , and broadband forcing was used to simulate the initial noise. ....	151
Figure 6.6: PSD plot of the limit cycle region in Figure 6.5 for positions 1, 2, and 5 .....	152
Figure 6.7: Time slices taken during the small amplitude forcing (0.084 seconds), the growth region (0.14 and 0.16 seconds), and the limit cycle region (0.18 and 0.24 seconds) for PSD analysis.....	152
Figure 6.8: PSD plot at 0.084 seconds in the noise region of the pressure trace of Figure 6.5 for positions 1, 2, and 5 .....	153
Figure 6.9: PSD plot at 0.14 seconds in the growth region of the pressure trace of Figure 6.5 for positions 1, 2, and 5 .....	154
Figure 6.10: PSD plot at 0.16 seconds in the growth region of the pressure trace of Figure 6.5 for positions 1, 2, and 5 .....	154
Figure 6.11: PSD plot at 0.18 seconds of the pressure trace of Figure 6.5 for positions 1, 2, and 5 .....	155
Figure 6.12: Pressure history plot (left) and PSD plot (right) for a 15 inch chamber and $\beta = 2000$ . The unstable frequency is 1400 Hz. ....	157
Figure 6.13: Pressure history plot (left) and PSD plot (right) for a 20 inch chamber and $\beta = 2050$ . The unstable frequency is 2000 Hz. ....	157

Figure	Page
Figure 6.14: Pressure history plot (left) and PSD plot (right) for a 35 inch chamber and $\beta = 2050$ . The unstable frequency is 550 Hz. ....	158
Figure 6.15: Experimental (left) and computational (right) PSD plots at position 2 for the 15, 20, and 25 inch cases. A response function was applied to the computational model to cause instability. ....	160
Figure 6.16: Experimental (left) and computational (right, repeated) PSD plots at position 2 for the 35 inch case. The experimental PSD plots show both the early and late instabilities. A response function was applied to the computational model to cause instability. ....	161
Appendix Figure	
Figure A.1: Axial output locations for acoustic frequency analysis .....	172
Figure B.1: FFT plot of the 15 inch chamber case forced with small amplitude, broadband mass-flow forcing. The upstream wall boundary condition is applied with an oxidizer source term. ....	175
Figure B.2: FFT plot of the 20 inch chamber case forced with small amplitude, broadband mass-flow forcing. The upstream wall boundary condition is applied with an oxidizer source term. ....	176
Figure B.3: FFT plot of the 25 inch chamber case forced with small amplitude, broadband mass-flow forcing. The upstream wall boundary condition is applied with an oxidizer source term. ....	177
Figure B.4: FFT plot of the 35 inch chamber case forced with small amplitude, broadband mass-flow forcing. The upstream wall boundary condition is applied with an oxidizer source term. ....	178



## ABSTRACT

Smith, Randolph Jedediah. M. S. E., Purdue University, August 2006.  
Computational Modeling of High Frequency Combustion Instability in a Single-Element Liquid Rocket Engine. Major Professor: Charles L. Merkle.

A one-dimensional CFD model was designed to investigate and simulate high frequency longitudinal combustion instability. The geometry and conditions of the model were based on a single-element liquid rocket engine experiment performed at Purdue which successfully produced spontaneous combustion instability over a range of frequencies. The frequencies of the experimental unstable acoustic modes were matched within 4% for each chamber length. The computational mode shapes showed fairly good agreement with the experimental data inside of the chamber, especially near the injector/chamber interface. Also, Mach number effects on the acoustic modes were shown to be significant. Increasing the Mach number decreased the frequency of the mode while also changing the mode shape.

The capability of the computational model to simulate non-linear behavior was investigated by comparing the power spectral density (PSD) plots of the experiments to PSD plots of computations forced at 70% of the mean mass flow-rate. These results compared well, showing the same non-linear behavior of higher harmonic excitation. The amplitudes of the computational power peaks were within an order of magnitude of the experimental results for all chamber lengths. The pressure history plots were also compared, showing similar wave steepening behavior.

A basic response function was developed where the heat release was assumed to be exactly in phase with the pressure oscillations, which meant that only one parameter was necessary to define the relationship between heat release and pressure. Depending on the size of this parameter, the small amplitude pressure oscillation decayed, grew to a limit cycle, or caused the code to diverge. The general behavior of spontaneous combustion instability was shown with the computational model.

The response function was also applied with initial broadband small amplitude noise. The resulting PSD analysis of the limit cycle region showed that in each case, a particular acoustic mode dominated the frequency response with its accompanying higher harmonics. The computational model predicted the same unstable acoustic mode as the experiment in two of the four chamber length cases. Although the computational power peaks were somewhat lower in amplitude (by about an order of magnitude), the qualitative behavior was very similar.



## CHAPTER 1. INTRODUCTION

### 1.1. Combustion Instability in Rocket Engines

The large amount of energy generated in a rocket engine combustion chamber, combined with the confined space in which this energy is generated, produces very favorable conditions for instability. Pressure oscillations in the chamber may start out as low amplitude noise. Because of the confined geometry, these pressure oscillations can reflect back into the system and couple with the combustion, possibly growing to destructive levels. Although these oscillations may eventually reach a limit cycle, the thermal and mechanical loads that are created are often large enough to cause severe damage to the rocket. In some cases, failure may even occur. This phenomenon is referred to as combustion instability and is traditionally defined as oscillations greater than  $\pm 5\%$  of the mean pressure.<sup>1</sup> Its occurrence is difficult to predict due to the complex combustion processes involved and the associated non-linear behavior. Combustion instability remains a serious impediment to rocket engine development.

The problem of combustion instability has plagued rocket engine design programs since the 1930's, resulting in extensive testing and analysis in order to produce stable rocket engine designs.<sup>2</sup> One example of this was in the development of the F-1 rocket engine, which was used as part of the Apollo program. Over the course of four years, more than 2000 full-scale tests were required to ensure the stability of the engine.<sup>3</sup> The very expensive nature of this testing has hampered the design of new rocket engines. The development of

most new rockets has relied on empirical information obtained from past 'heritage' designs, limiting the amount of innovation that can be done.

Computational fluid dynamics (CFD) algorithms and computing hardware are both advancing to the point where computational modeling is becoming an attractive tool to aid in engine design. Attempts have been made to incorporate complex physics into CFD models in order to analyze combustion instability.<sup>19,20</sup> While CFD has successfully been able to simulate the mean-flow of multi-phase and reacting flow-fields in combustion, its capabilities for simulating unsteady dynamics has not yet been fully realized. Because of its limitations, any computational modeling must be validated with experimental studies to ensure accuracy.<sup>4</sup> The objective of this thesis is to assess the role computational models can have in simulating combustion instability using experimental data as a source for validation.

Section 1.1 gives a brief overview and description of combustion instability, especially as it relates to the type of instability being modeled in this research. The four sections describe the necessary conditions for instability to occur, the types of combustion instability, the acoustics feeding the pressure oscillations, and the heat release mechanisms. A comprehensive review of the combustion instability problem up to 1974 can be found in NASA SP-194.<sup>2</sup> A more recent review was also compiled in 1995 to summarize the developments since 1974.<sup>5</sup>

### 1.1.1. Rayleigh's Criterion

Rayleigh's criterion describes conditions under which combustion instability can occur.<sup>6,7</sup> If the heat release oscillation due to combustion,  $Q'$ , is at a maximum (minimum) when the pressure oscillation,  $p'$ , is at a maximum (minimum), the pressure oscillation will increase in magnitude. In other words, if the heat release and pressure oscillations are close to being in-phase, constructive interference will occur and the pressure oscillation will grow. The

pressure oscillation will decrease if the heat release and pressure oscillations are close to being out-of-phase. In-phase behavior (leading to growth) is shown in Figure 1.1. Out-of-phase behavior (leading to decay) is shown in Figure 1.2.

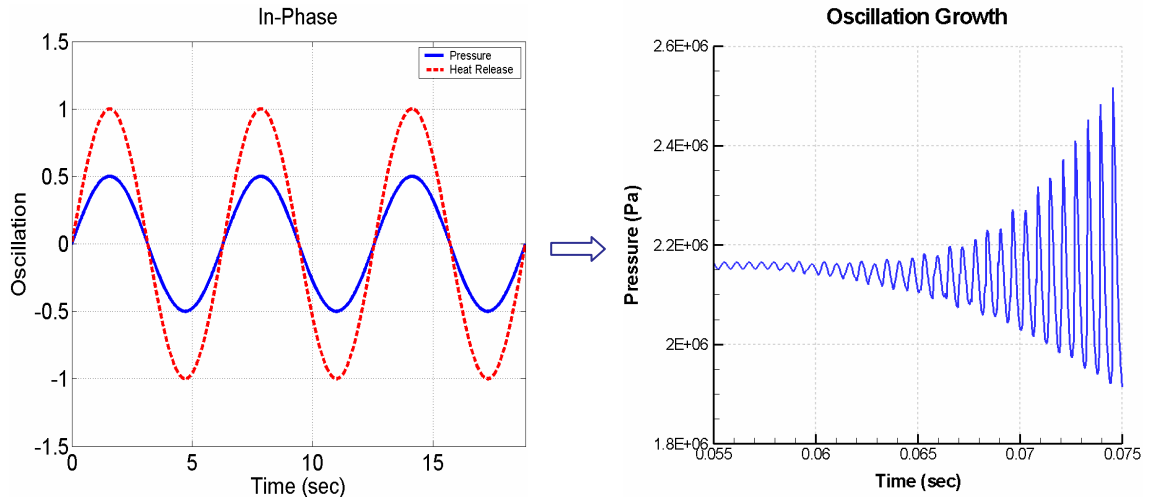


Figure 1.1: Pressure and heat release oscillations that are exactly in-phase (left) and growth of the pressure oscillations over time due to this condition (right)

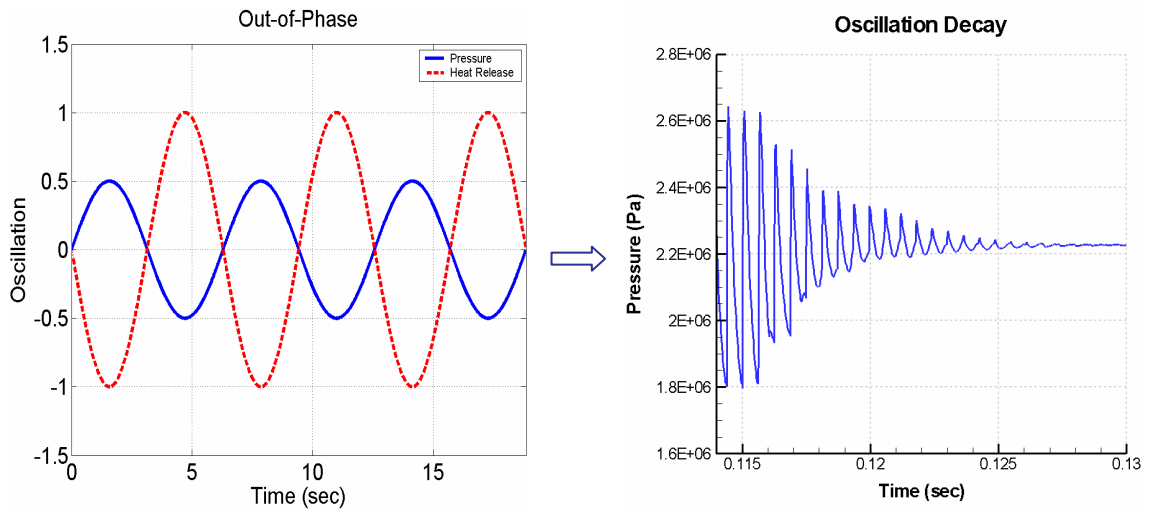


Figure 1.2: Pressure and heat release oscillations that are exactly out-of-phase (left) and decay of the pressure oscillations over time due to this condition (right)

The pressure and heat release coupling inherent in Raleigh's criteria can be expressed mathematically as the integral of the product of the pressure and heat release oscillations, as shown in Equation 1.1.<sup>8</sup> Note that the pressure and heat release oscillations are spatially and temporally varying.

$$\int_0^{t_{\text{cycle}}} p'(\vec{r}, t) \dot{Q}'(\vec{r}, t) dt \quad \text{Eq. 1.1}$$

If the above integral is greater than zero, the pressure oscillations will grow and the system will be unstable. Because of non-linear effects, a limit cycle may eventually be reached. Models for combustion instability often begin with some form of the Rayleigh criterion. Response functions are models that describe how the heat release,  $Q'$ , is governed by certain mechanisms in the flow.<sup>18</sup> These combustion mechanisms and the accompanying response functions are discussed further in Section 1.1.4.

Along with the heat release oscillation term, successful prediction of instability must include the damping in the system. There may be boundaries or energy sinks in the system which can dissipate energy. For example, the nozzle has been found to have a damping effect on longitudinal oscillations.<sup>41</sup> Even if the pressure and heat release are in phase, instability may still not occur due to energy being taken out of the system faster than it can be added. Predicting combustion instability requires finding a balance between the amount of energy driving and damping the pressure oscillations. Knowing both the phase relationship and gain between the pressure and heat release oscillations is essential to accurate modeling of combustion instability.

### 1.1.2. Types of Instability

Different types of combustion instability are generally classified by the frequency at which the instability occurs. These are often categorized into low and high frequency instability. Intermediate frequency instability, which represents the gray area between high and low instability, may also be included.<sup>1</sup> Low frequency instabilities are on the order of 10-100 Hz and are non-acoustic in nature. This instability can cause structural damage. High frequency instabilities are on the order of 1000 Hz and are strongly coupled to the acoustics of the system. Most of the damage done by this type of instability is due to high thermal loads placed on the system.

Low frequency instability can be separated into two classes. The first involves structural coupling of the entire engine. In this case, structural accelerations of the vehicle couple with mass flow oscillations in the propellant feed system. This occurs on the order of 10 Hz and is referred to as chugging. The second class involves the coupling of the injected flow and the combustion oscillations with the residence time oscillations of the chamber. This is referred to as bulk mode coupling or pogo instability and occurs on the order of 100 Hz.<sup>1</sup> The causes of low frequency instability are well understood, as are potential methods for controlling it.<sup>9</sup>

High frequency instability, referred to as screeching, can also be separated into two classes, both involving a strong dependence on the chamber acoustics. In the first class, the characteristic acoustic times are coupled with the injection flow oscillations, causing them to have a strong effect on the heat release of the system. In the second class, the characteristic acoustic times are coupled with one or many of the various combustion processes. Since both of these cases occur on the order of 1000 Hz, it may be very difficult to determine which mechanism is coupling with the characteristic acoustic times.

The research conducted in this thesis focuses on high frequency instability. This type of instability is quite prevalent in liquid rocket engines and is

not well understood, because of to the complexity of the injector dynamics and combustion processes. It continues to represent a major obstacle to the efficient design of new rocket engines. This is also the type of instability which is addressed in the Purdue longitudinal experiment, introduced in Section 1.3. The experiment was designed to produce high frequency instability that was coupled with the longitudinal acoustic modes of the system.<sup>10,11</sup> The data obtained from this experiment is used for validation purposes.

The modeling of high frequency combustion instability requires careful attention to the system acoustics, the injection mechanism, and the combustion processes. Section 1.1.3 discusses the analytical models which are used to determine the acoustic modes for simple geometries and conditions. Section 1.1.4 discusses the relevant combustion processes which may interact with the acoustics to produce high frequency instability.

### 1.1.3. Acoustic Mode Analysis

Because acoustic coupling plays such an important role in high frequency combustion instability, it is necessary to have an understanding of how the acoustic modes are sustained and of the coupling behavior. High frequency instabilities are usually classified as longitudinal or transverse, depending on the type of acoustic mode that is being excited. In cylindrical chambers, the transverse modes can be tangential or radial. In addition, mixed modes can also exist which combine the motions of various simple acoustic modes.<sup>12</sup>

Acoustic analyses generally begin with the derivation of a wave equation. For the simple isentropic case with no mean flow, a pressure wave equation can be derived by combining the equations of mass, momentum, and energy for inviscid conditions.<sup>13</sup> The homogeneous wave equation is shown in Equation 1.2,

$$\nabla^2 p - \frac{1}{a^2} \frac{\partial^2 p}{\partial t^2} = 0 \quad \text{Eq. 1.2}$$

where  $a$  is the speed of sound and  $p$  is the pressure.

Equation 1.2 can be rewritten as the Helmholtz equation by putting the pressure in terms of a velocity potential (see Morse<sup>13</sup> for the complete derivation). The Helmholtz equation and its boundary condition are shown in Equations 1.3 and 1.4,

$$\nabla^2 \psi_n - k_n^2 \psi_n = 0 \quad \text{Eq. 1.3}$$

$$\vec{n} \cdot \nabla \psi_n = 0 \quad \text{Eq. 1.4}$$

where  $\psi_n$  represents the normal mode shape for the  $n$ th mode,  $k_n$  is the wave number ( $k_n = \omega_n/a$ ), and  $\omega_n$  is the frequency of the  $n$ th mode.

Equation 1.3 can be solved for  $\psi_n$  for a cylindrical closed chamber by using separation of variables and applying the appropriate boundary conditions. These boundary conditions correspond to zero velocity oscillation at all walls ( $u' = 0$ ) and a finite velocity at the centerline. The solution for the normal mode  $\psi_n$  and the wave number  $k_n$  is shown in Equations 1.5 and 1.6.

$$\psi_n = \cos\left[\left(\frac{\pi l}{L}\right)x\right] J_m(\kappa_{ms}r) \begin{cases} \cos(m\theta) \\ \sin(m\theta) \end{cases} \begin{cases} l = 0, 1, 2, \dots \\ m = 0, 1, 2, \dots \\ s = 0, 1, 2, \dots \end{cases} \quad \text{Eq. 1.5}$$

$$k_n^2 = \frac{\omega_n^2}{a^2} = \left(\frac{\pi l}{L}\right)^2 + (\kappa_{ms})^2 \quad \text{Eq. 1.6}$$

In Equation 1.5, there are two possible normal modes shown by the cosine and sine terms corresponding to each frequency. The various modes are obtained by choosing different values for  $l$  (longitudinal modes),  $m$  (tangential modes), and  $s$  (radial modes). For example, a pure longitudinal mode would be obtained by choosing  $l = 1$  and  $m = s = 0$ . The  $J_m$  function refers to the Bessel function and  $(\kappa_{ms}R)$  is the  $s^{\text{th}}$  positive zero of the  $dJ_m(r)/dr$  function for  $s \neq 0$ . For  $s = 0$ ,  $\kappa_{ms} = 0$ . This result allows both pure and mixed modes to be represented.<sup>12</sup>

The first and second pure longitudinal, tangential, and radial modes are shown in Figure 1.3 - Figure 1.5. The longitudinal pressure and velocity mode shapes are shown with 2-D plots looking lengthwise at the horizontally oriented cylindrical chamber. The tangential and radial pressure mode shapes are shown with 3-D plots, where the vertically oriented cylindrical chamber is only implied.

### Pure Longitudinal Modes

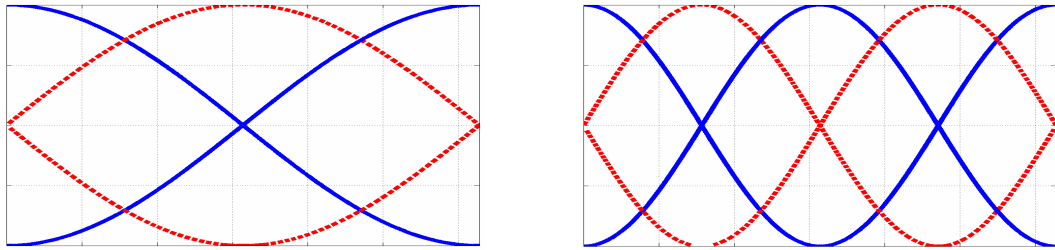


Figure 1.3: The first (left) and second (right) pure longitudinal modes for a closed chamber, where pressure is shown in blue and velocity in red

### Pure Tangential Modes

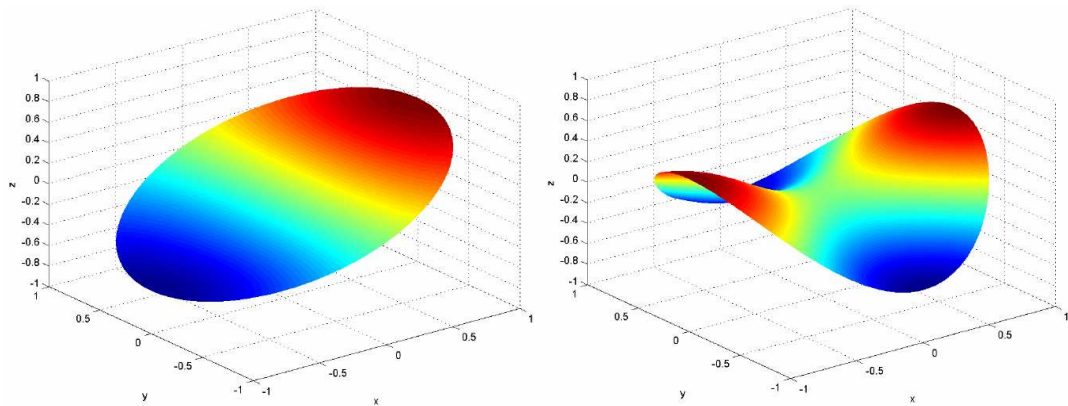


Figure 1.4: The first (left) and second (right) pure tangential pressure modes

### Pure Radial Modes

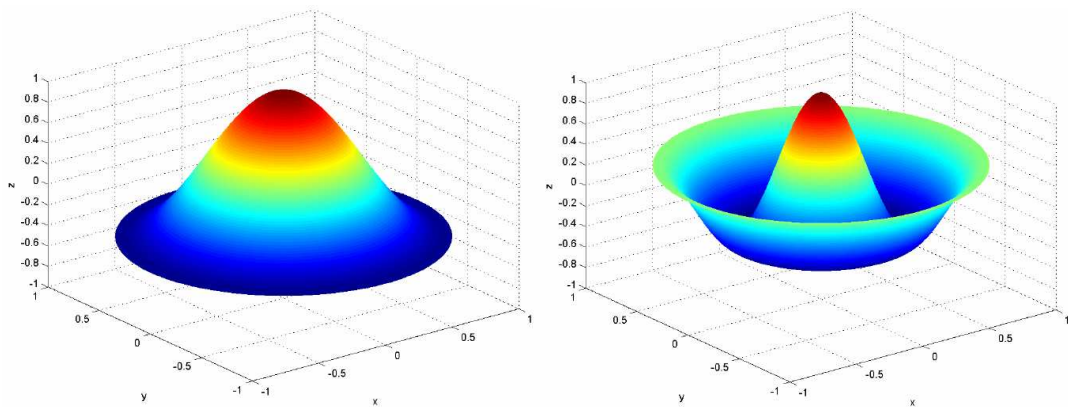


Figure 1.5: The first (left) and second (right) pure radial pressure modes



As mentioned in the previous section, the Purdue experiment is designed to produce high frequency, longitudinal instabilities. This simplifies acoustic analysis considerably because the longitudinal modes can be found using one-dimensional analysis. Assuming that  $m = s = 0$ , Equation 1.5 simplifies to:

$$\psi_n = \cos\left[\left(\frac{n\pi}{L}\right)x\right] \quad \{n = 0, 1, 2, \dots\} \quad \text{Eq. 1.7}$$

$$k_n^2 = \frac{\omega_n^2}{a^2} = \left(\frac{n\pi}{L}\right)^2 \quad \text{Eq. 1.8}$$

where  $l$  (in Equations 1.5 and 1.6) has been replaced with  $n$ . Since  $\omega_n = 2\pi F_n$ , the mode frequency in Hertz for the  $n$ th mode,  $F_n$ , can be solved as,

$$F_n = \frac{na}{2L} \quad \text{Eq. 1.9}$$

Throughout this thesis, acoustic modal analysis will be restricted to determining and validating longitudinal modes, since these are the modes which are driving the instabilities in the experiment. Because of the non-simple geometry and flow conditions in the experiment, the acoustic frequencies and mode shapes are determined through CFD analysis (although these results are compared to an analytical model for verification<sup>14</sup>). These results, along with accompanying experimental validation, are shown in CHAPTER 3.

#### 1.1.4. Heat Release Mechanisms and Response Functions

According to Rayleigh's criterion, combustion instability is caused by interactions between the pressure and heat release oscillations (see Equation 1.1). For high frequency instability, the pressure oscillations depend on the system acoustics (see Section 1.1.3). The heat release is influenced by various

dynamic combustion processes, many of which are controlled by the injection mechanisms. These processes can be loosely separated into the mechanisms of injection, atomization, vaporization, mixing, and reaction. Expansion in the nozzle is also very important for creating the necessary thrust in rocket engines, but has little effect on instability other than to damp longitudinal oscillations. These processes (and accompanying descriptions) are shown in Figure 1.6. They are touched on very briefly in this section in order to demonstrate the complexity of the combustion process. Note that not all of these mechanisms are necessarily pertinent to the experimental injection configuration discussed in Section 1.3.

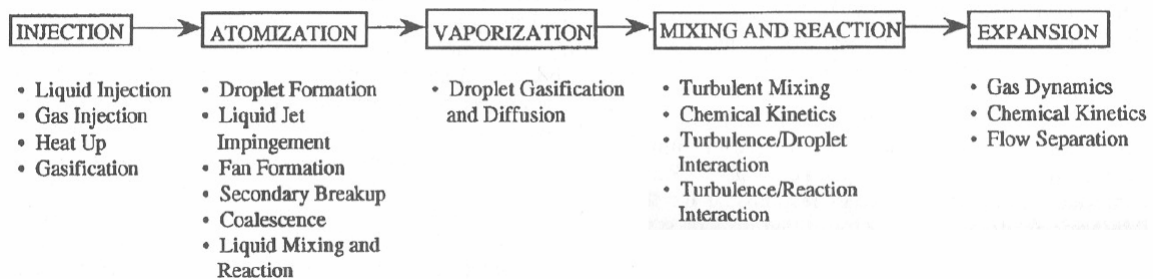


Figure 1.6: Combustion processes which may influence the heat release oscillations in liquid rocket engine systems<sup>9</sup>

The coupling between the pressure and heat release oscillations is thought to occur with the combustion process which has a similar characteristic response time as the system acoustics.<sup>10</sup> Each of these processes has been studied to various degrees in connection with combustion instability. The injection and vaporization processes have received the most attention, but atomization has also been studied greatly. The chemical kinetics mechanism generally has characteristic times much shorter than the other processes, meaning that it occurs relatively fast. Because of this and due to its complexity, chemical kinetics has not received much attention with respect to combustion instability. The mixing process may have a very significant effect on stability.<sup>10</sup>

These processes are largely governed by the injection mechanism that feeds the propellants into the chamber. Historically, three main types of injectors have been used in liquid rocket engines designed in the United States. These correspond to impinging jets, concentric jets (coaxial injection), and jet/sheet injection (non-coaxial).<sup>9</sup> The Purdue longitudinal experiment was designed for coaxial injection, as discussed in Section 1.3. The computational model will also focus on this type of injection system.

Due to the complex turbulent nature of these processes, the oscillating heat release introduced by combustion is usually modeled using response functions. An early response function that was applied to combustion instability was the sensitive time lag model developed by Crocco in the 1950's.<sup>16,17,27</sup> Also known as the 'n- $\tau$ ' model, this function relates the heat release to pressure by using empirically determined growth (n) and phase ( $\tau$ ) parameters. Various heat release response functions have been developed since then which relate the heat release to flow conditions such as pressure, velocity, mass flow-rate, and vorticity.<sup>28-31</sup> These response functions can be set in either the time or frequency domains. Those which are functions of time have a similar form to Crocco's time lag model. Those which are set in the frequency domain take the form of a transfer function.<sup>18</sup> The heat release response functions are combined with other modeling approaches of the system (which account for the acoustics and flow properties) in order to model combustion instability.

## 1.2. Modeling Approaches

The problem of combustion instability can be approached at various levels of modeling. Simple analytical models can be used to approximate the basic mode shapes of the system depending on the geometry and speed of sound (see Section 1.1.3). More complicated analytical models use response functions with the equations of motion to gain a qualitative understanding of the relationship

between linear instability growth and heat release mechanisms.<sup>15</sup> This type of analysis is discussed in more detail in Section 1.2.1.

Due to increasing computational capability and the limitations of analytical modeling, computational models are becoming increasingly useful in characterizing combustion instability. These can be used in one, two, or three-dimensions and can handle geometric complexities much more easily than analytical models. Computational models also have the potential to model non-linear behavior and complex fluid dynamics. However, computations can be very expensive and time consuming, and can only give solutions for particular cases. Despite these shortcomings, computations may be the most accurate means of simulating the complex fluid and combustion mechanisms leading to combustion instability.

Regardless of what level of modeling is used, experimental testing is necessary to validate these models. The complexity of combustion instability is such that no model is yet able to accurately predict instability from first principles.<sup>15</sup> Experimental data can be used to refine and validate models, while models can be used to give understanding and guidance in focusing the experimental studies. Some level of experimentation will always be necessary to ensure the safety and proper functionality of any new rocket engine design.

The following sections give a broad overview of some of the levels of modeling that have been used to understand combustion instability. The level of modeling that is being used for this research is discussed in Section 1.2.2.

#### 1.2.1. Generalized Wave Equation Analysis

One analytical model that has been shown to be useful is the generalized model for unsteady motions in two-phase flow that was developed by Culick.<sup>15</sup> The objective of this model is to approximate combustion instability behavior for a general propulsion system. By focusing on the common aspects of combustion instability, the analysis can be applied to various propulsion systems. Because it

models various types of heat release mechanisms, these mechanisms can be compared quickly to determine their relative impact on instability. The model can also be narrowed to a specific propulsion system by retaining only the relevant terms. One version of this model has recently been developed using Matlab and has been used to evaluate instability in both rocket and augmentor systems.<sup>18</sup>

A very brief overview of the model derivation is given here. Classical acoustic analysis is used to obtain the spatially-varying normal modes. These are dependent on the specific geometry of the propulsion system, but the generalized model can accept any normal mode shape as an input. The perturbed forms of the equations of motion are then used for instability analysis. Two-phase flow is assumed and the flow properties are mass-averaged. The equations of motion are combined to obtain an inhomogeneous version of the wave equation for the pressure perturbation. The accompanying boundary conditions are also inhomogeneous.

The model then analyzes the question of how the source terms affect the temporal growth or decay of the corresponding modes. Various source terms are modeled using response functions, corresponding to the different combustion processes and fluid mechanisms occurring in the system. Admittance and impedance conditions are also defined for the boundaries to account for any damping or feed-back of energy. Both the response functions and admittance conditions are put in terms of a decay constant ( $\alpha$ ). The final result is obtained by placing all of the source terms together and solving the system numerically for the given conditions. If the decay constant is greater than zero, combustion instability is predicted for the propulsion system. If it is less than zero, stable operation is predicted. The model essentially balances the sources of energy amplification and attenuation to determine whether the normal mode will grow or decay over time.

### 1.2.2. Euler/RANS Computations

Euler or RANS modeling is based on using either the Euler or Reynolds Averaged Navier-Stokes (RANS) equations as the governing equations for the system. Computational fluid dynamics (CFD) is then employed to solve for the accurate mean conditions of the propulsion system. The unsteady behavior is approximated through heat release response functions. Combustion instability is predicted if the amount of energy introduced by the response function is greater than the amount of damping in the computational domain.

This level of modeling is advantageous in that complicated geometry can be applied and non-linear behavior can be accurately simulated. Also, the acoustical mode analysis is not limited to a simple analytical model and therefore can incorporate such real conditions as mean flow. However, the added expense of computations will require more time to obtain solutions. Parametric studies and combustion process comparisons cannot be done as quickly as with analytical models.

The research that is being performed in this thesis uses CFD solutions of the one-dimensional Euler equations to investigate instabilities in a combustor, which includes an injector, combustion chamber, and nozzle. A source term is used to model the steady combustion. Mass flow forcing and response functions are applied to model the unsteady behavior of the system. A detailed description of the computational model is given in CHAPTER 2.

### 1.2.3. Detailed Unsteady Dynamics Computations

While CFD cannot obtain exact solutions for the complex conditions in a liquid rocket engine, certain processes can be simulated fairly well. Detailed unsteady dynamics computations can be used to model the behavior of the combustion processes that lead to instability. The turbulent vorticity of flow

exiting an injector element is shown in Figure 1.7 for a Reynolds number of 12,000.

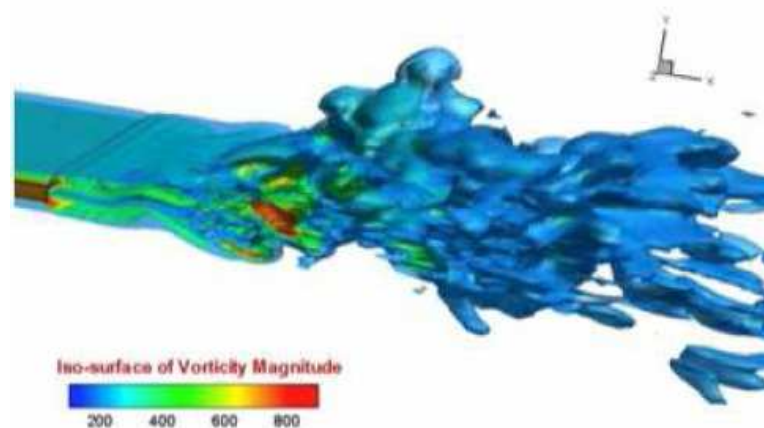


Figure 1.7: Turbulent vorticity computation of flow exiting an injector element for  $Re = 12000$  <sup>21</sup>

Because these computations are often expensive, obtaining solutions may be a time consuming process and it may be difficult to use this level of modeling for rapid parametric studies or quick comparisons. Instead, these computations are used most effectively as means of validating and guiding the derivation of response functions for lower order models. The detailed calculations are able to simulate a particular combustion mechanism. The response function for this mechanism can then be calibrated or modified based on the detailed computational results. This response function can then be used in conjunction with an analytical, Euler, or RANS model to predict instability. This approach is similar to using experimental data to characterize parameters for analytical models. The computations, while expensive, are generally much less expensive than full scale experimental tests.

### 1.3. Purdue Single-Element Combustion Instability Experiment

Combustion instability experiments for liquid rocket engines are performed on various levels, depending on the objectives of the experiment. These can be categorized into research or lab scale tests, sub-scale tests, and full-scale tests. Research or lab scale tests use simplified geometry and conditions and can be highly instrumented to obtain detailed data of the combustion processes. Sub-scale tests use scaled down geometry and conditions from the actual engine design. This allows for a less expensive experimental setup and for more instrumentation, while still providing results which can be scaled up to the full-scale engine design. Full-scale tests use the actual engine design for experimentation. While this provides the best indication of how the engine will operate, it allows for little instrumentation and is expensive.<sup>10</sup>

The Purdue experiment is comprised of lab scale tests. This scale allows for heavy instrumentation, which can be used to gain detailed understanding of the combustion instability behavior. It also provides a wealth of validation data for computational models. Because of the success of the experiment in producing combustion instability, the computational research of this thesis closely follows the Purdue experiment. The instability in the experiment was coupled with longitudinal acoustic modes, which allows the computational model to be one-dimensional. This simplifies the model considerably and allows results to be obtained quickly. This section summarizes the objectives, configuration, and results of the experiment. For a complete description of the experiment and results, see <sup>10-11</sup>.

#### 1.3.1. Experimental Objectives and Design Considerations

The two main objectives of the Purdue experiment were to: 1) obtain useful data which would provide insight into the complex combustion dynamics of a liquid rocket engine injector and 2) develop a tool which could be used for



stability rating of injector elements of full-scale rocket engines. To achieve this, it was important that the experiment provide sufficient instrumentation to obtain detailed data. It was necessary that some range of combustion instability be exhibited in the experiment.

A single element coaxial swirl injector was chosen for the experiment. A coaxial injector is inherently less reliant on multi-element interactions than are impinging jet injectors. This allows for detailed observation of the complex combustion injection dynamics occurring in the injector (such as mixing and reaction), which would not be possible if a multi-element injector were used. The injector was designed so that it gives an accurate representation of the injection behavior of a full-scale rocket engine. This was done by matching the scale and acoustics of a full-scale injector while reducing the size of the chamber to an appropriate length scale corresponding to a stream tube.

Because transverse instabilities are the most prevalent type in liquid rocket engines, the geometry of the injector is designed to exhibit longitudinal acoustic modes which are in the same frequency range as the first two transverse modes. To understand how the combustion response is affected by changing acoustics, the combustion chamber length is discreetly varied through a range of 10 to 35 inches. This will change the natural acoustic modes of the chamber and should affect the combustion instability response.

Combustion instability can occur through two distinct means, designated as spontaneous instability and triggered instability.<sup>9</sup> Spontaneous instability occurs as small perturbations grow linearly until a non-linear limit cycle is achieved. Triggered instability requires an initially large disturbance (such as a bomb) to start the instability. Once it begins, the instability perpetuates itself through feedback of pressure oscillation in the system. Spontaneous instability is the preferred means of inducing instability for the experiment because it allows the oscillation growth to be observed from small amplitude perturbations to a non-linear limit cycle. Also, this simplifies the experimental and computational

configurations because no artificial forcing is required and data analysis does not require extraction of the forcing function.

To help promote some range of spontaneous instability, certain destabilizing characteristics are integrated into the design. The oxidizer is injected radially into the injector, allowing for a hard wall boundary at the injector head-end. A wall boundary produces the largest amount of wave reflection, allowing for maximum feed-back of pressure oscillations into the system. Also, the nozzle was made relatively short with only a converging section. This limits the damping capability of the nozzle for longitudinal acoustic modes.

Because stronger acoustic modes increase the likelihood of instability, an attempt was made to match the injector and chamber modes so that coupling would occur. Specifically, the first injector mode was matched with the second chamber mode for a chamber length of 20 inches and 2200 Hz. This is shown in Figure 1.8 with the injector and chamber geometry. A baseline frequency of 2200 Hz was chosen because it is in the range of transverse acoustic modes.

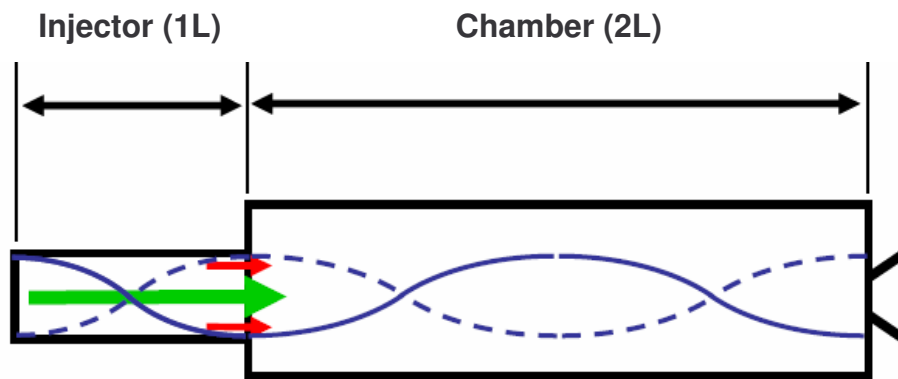


Figure 1.8: Acoustic coupling between the injector 1L mode and the chamber 2L mode at 2200 Hz. Oxidizer flow is represented with the green arrow while fuel flow is represented with red arrows.<sup>10</sup>

Note that there is a pressure anti-node at the injector/chamber interface. Much of the mixing and reaction is thought to occur in this region, producing a significant amount of heat release. Then, according to Rayleigh's criterion, there

is a strong possibility of pressure oscillations (due to acoustics) coupling with the heat release (due to combustion) to produce spontaneous combustion instability.

### 1.3.2. Experimental Configuration

A modified version of the Russian RD-170 injector was chosen as the single-element injector.<sup>36,37</sup> This is a gas centered, liquid swirl coaxial injector that has been primarily used with high pressure, oxygen/kerosene propellants. For the Purdue experiment, 90% by weight hydrogen peroxide ( $\text{H}_2\text{O}_2$ ) was used instead of oxygen so that the hardware would not have to be chilled prior to testing and so that auto-ignition between the fuel and oxidizer would occur.<sup>11</sup> As it passes through the catalyst bed, the hydrogen peroxide is decomposed to 42% superheated oxygen and 58% superheated water vapor by weight, where it is injected radially into the injector. The oxidizer and swirling JP-8 fuel begin to mix before entering the combustion chamber. A schematic of the injector element is shown in Figure 1.9.

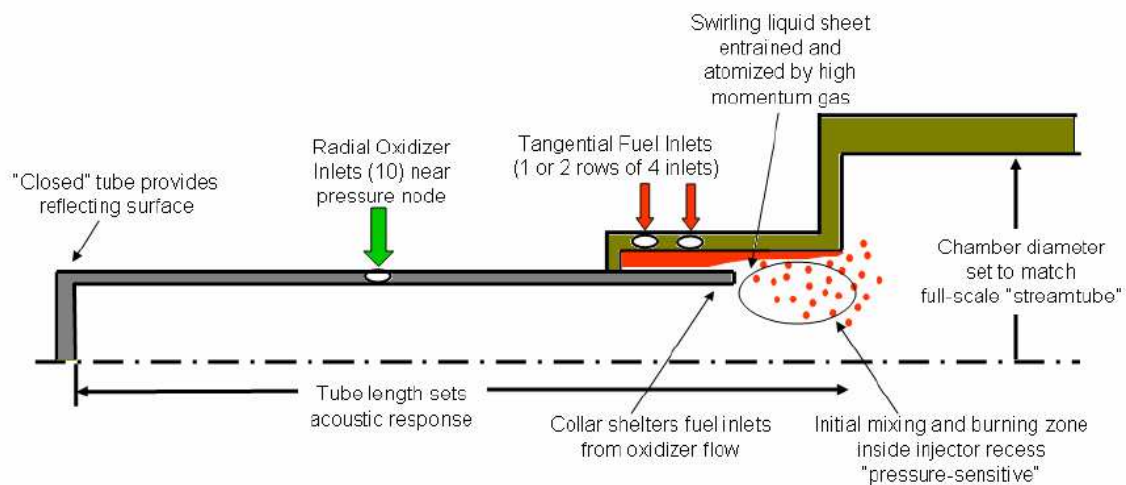


Figure 1.9: Gas centered, liquid swirl coaxial injector element, based on the Russian RD-170<sup>10</sup>

The schematic shows oxidizer being introduced into the injector at the injector midway point (large green arrow). This orifice is sized to create a choked condition, thereby acoustically decoupling the oxidizer manifold from the rest of the system. Notice that there is a solid wall at the injector head-end to maximize pressure oscillation reflection. The fuel is introduced through four tangential inlets close to the injector/chamber interface (small red arrows). Two different fuel injection configurations were used. The first (shown in Figure 1.9) has two rows of inlets and a pressure drop of 33 psi. The second has only one row with a pressure drop of 127 psi. As the high velocity oxidizer passes the fuel film, fuel droplets are stripped off, leading to mixing and reaction. A collar separates the oxidizer and fuel until they are close to the injector/chamber interface.

The entire experimental configuration is shown in Figure 1.10 for a chamber length of 25 inches. To investigate the effects of changing acoustics on instability, the length of the combustion chamber was discretely varied throughout the experiments to 10, 15, 20, 25, and 35 inches. The high frequency pressure transducer locations are shown by the red dots (not all chamber pressure transducers are shown). Low frequency pressure transducers and thermocouples were also used.

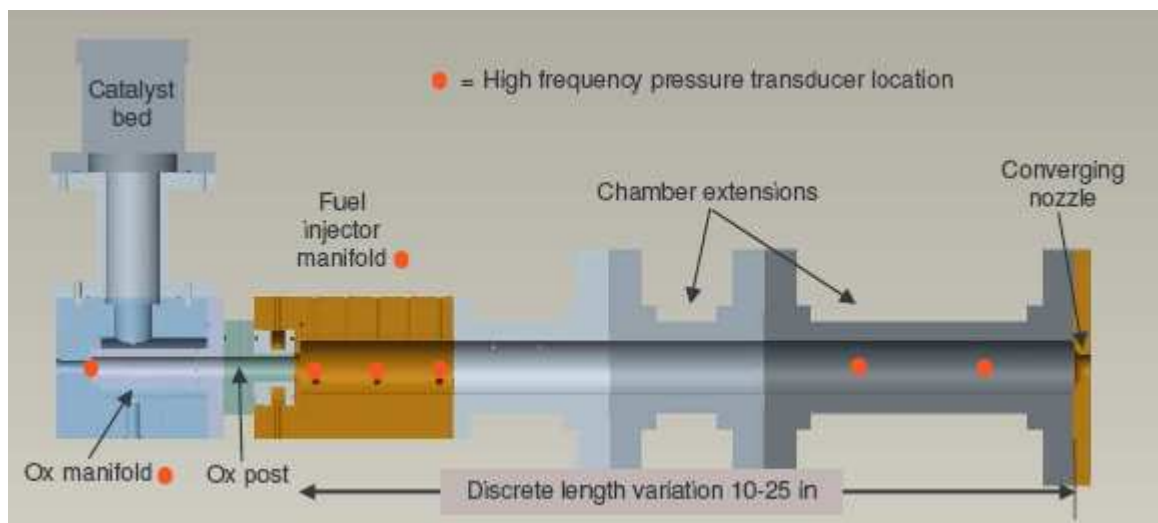


Figure 1.10: Purdue experimental setup with a 25 inch chamber length. The locations of high frequency pressure transducers are specified with red dots.<sup>10</sup>

The important dimensions for the one-dimensional computational model are given here. All dimensions, including parts drawings, can be found in Miller<sup>10</sup>. The injector diameter is 2.05 cm (0.806 in) and its length is 17.1 cm (6.72 in). The oxidizer is introduced in the middle of the injector, at 8.64 cm (3.40 in). The approximate temperature of the oxidizer in the injector is 1029 K (1852 °R). The flow-rate of the oxidizer is within 0.459 - 0.477 kg/s (1.01 - 1.05 lb/s). The chamber diameter is 4.65 cm (1.83 in) and the length is discretely varied from 25.4 to 88.9 cm (10 to 35 in). The nozzle length is 1.27 cm (0.5 in). A picture of the fully instrumented experimental configuration is shown in Figure 1.11, on the test stand at the High Pressure Laboratory at Purdue.

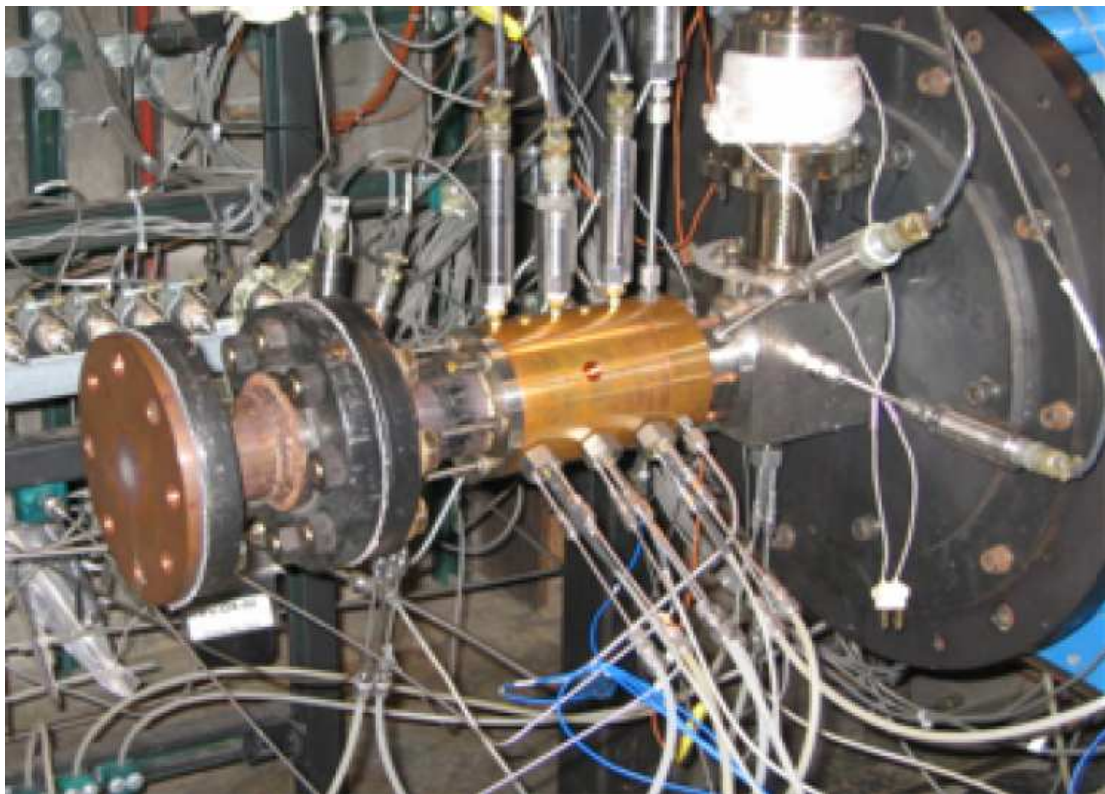


Figure 1.11: Picture of the fully instrumented configuration of the Purdue longitudinal experiment for the 15 inch chamber length<sup>10</sup>

### 1.3.3. Discussion of Experimental Results

A summary of the experimental conditions and results is shown in Table 1-1 for ten of the experimental tests. The test designation (1<sup>st</sup> column) is explained as follows. The first two digits correspond to the length of the combustion chamber in inches. The next digit corresponds to the level of fuel flow-rate used, with D = design ( $\sim 0.074$  kg/s), L = low (0.058 kg/s), and H = high (0.092 kg/s). The fourth digit refers to which fuel injector was used, either the first (1) with two rows of injection and a low pressure drop or the second (2) with only one row of injection and a high pressure drop. The r at the end means that it was a repeated test. So, for example, test 25D1r means that the test had a chamber length of 25 inches at the design flow-rate with the low pressure drop fuel injector and was a repeat. Although the data from each pressure transducer was analyzed, only the results from the 0.5 inch chamber transducer location (the first transducer location in the chamber) are shown in this section.

Table 1-1: Summary of conditions and results for the Purdue experiment

Test Designation	Chamber Length (cm)	Oxidizer Flow-rate (kg/s)	Fuel Flow-rate (kg/s)	O/F	$\eta_c$	$P_c$ (MPa)	Unstable Frequency (Hz)	$P'$ (kPa)
10D1	25.4	0.461	0.073	6.3	94.2	2.38	Stable	13
15D1	38.1	0.462	0.074	6.2	87.4	2.21	1502	295
20D1	50.8	0.479	0.073	6.5	86.3	2.21	1184	151
20D1r	50.8	0.464	0.074	6.3	90.1	2.29	1184	167
25H1	63.5	0.479	0.092	5.2	83.4	2.16	1672	431
25L2	63.5	0.466	0.058	8.0	88.4	2.19	1648	156
25D1	63.5	0.478	0.074	6.5	83.8	2.14	1709	328
25D1r	63.5	0.459	0.074	6.2	87.3	2.19	1660	258
25D2	63.5	0.461	0.073	6.3	86.5	2.18	1672	266
35D1 (early)	88.9	0.464	0.074	6.3	86.0	2.18	1721	244
35D1 (late)	88.9	0.463	0.074	6.3	87.7	2.22	1233	148



In the above table, O/F is the oxidizer to fuel ratio,  $\eta_c$  is the combustion efficiency, and  $P_c$  is the mean chamber pressure. Test 35D1 has two entries in the table because it went unstable at 1721 Hz early in the test and then transitioned to 1233 Hz late in the test. The  $P'$  parameter corresponds to the root-mean-square of the mean-to-peak pressure oscillation, and thus gives an indication of the instability of the test (a larger  $P'$  value indicates greater instability). It was obtained by integrating and summing the power of the first four peaks of the PSD plot for the corresponding test (see Figure 1.13). Then the square root was taken and this quantity was multiplied by the square root of two.

Using the low and high frequency pressure gauges, mean pressure (DC) and oscillating pressure (AC) traces were obtained for each test. The mean and oscillating pressure traces for test 25D1r are shown in Figure 1.12.

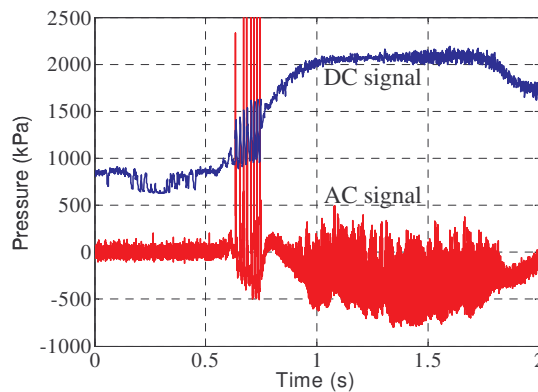


Figure 1.12: Mean pressure (DC) and oscillating pressure (AC) traces for test 25D1r<sup>10</sup>

The fuel valve was opened at time zero in Figure 1.12. For about the first 0.6 seconds, constant pressure is seen in the DC signal and low amplitude pressure noise is seen in the AC signal. The high amplitude spikes at around 0.7 seconds are the initial ignition event, common in liquid rocket engines. Note that after the ignition event, the DC signal steadily increases until it starts to level off to the mean pressure at about 0.85 seconds. During this same period, the AC

signal is increasing in amplitude and has reached a limit cycle by 1.1 seconds. The pressure amplitude in the limit cycle is about 800 Hz peak to peak, or about 40% of the mean pressure. This is characteristic of spontaneous, non-linear combustion instability behavior. The fuel valve was typically closed between 1.5-2 seconds, at which point the mean pressure started to decrease and the amplitude of the oscillating pressure decayed.

To obtain the frequency response, 200 ms time slices were taken during the limit cycle oscillation for each test. Power spectral density (PSD) analysis was then performed over this time interval to obtain the power ( $\text{kPa}^2/\text{Hz}$ ) amplitude at each frequency. In other words, a relative magnitude was calculated for each frequency to determine which modes are contributing to the signal. As was shown in Section 1.1, determining the unstable acoustic modes (and the frequencies at which these modes occur) is important in understanding combustion instability. The Fast Fourier Transform (FFT), which has been in use since 1965, is an efficient algorithm for determining the frequency response of a signal. Various texts describe the derivation and applications of this algorithm.<sup>38-40,44</sup> The FFT algorithm is applied in this thesis to analyze the small amplitude computational data in CHAPTER 3. In order to make quantitative comparisons with the experimental data, PSD analysis is used for all large amplitude computational results. The only difference in the output of the PSD and FFT analyses is the scaling of the signal amplitude.<sup>38</sup>

PSD plots are shown in Figure 1.13 for each chamber length at the design fuel flow-rate and with the first fuel injector. These correspond to experimental tests 10D1, 15D1, 20D1r, 25D1r, and 35D1 (early and late).



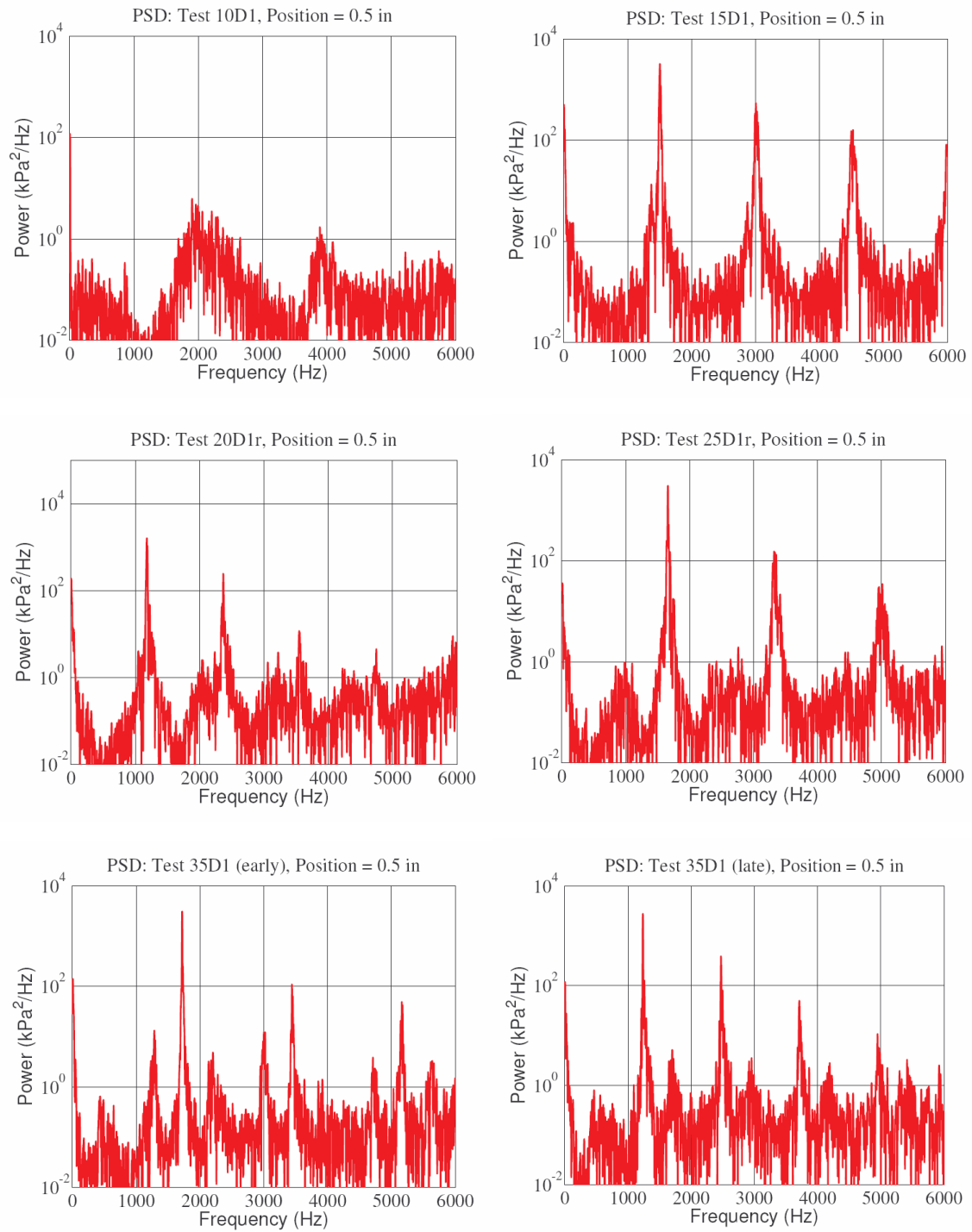


Figure 1.13: PSD plots for tests 10D1, 15D1, 20D1r, 25D1r, and 35D1 (early and late) <sup>11</sup>

All of these tests showed instability (defined as oscillations greater than 5% of the mean pressure), except the 10 inch chamber test (10D1). The unstable frequency for each test is the frequency at which the dominant (highest amplitude) power peak occurs. Non-linear behavior is observed for each unstable test, as the next highest peaks after the unstable frequency are always integral multiples of the original unstable frequency. These correspond to higher harmonics of the unstable frequency. For certain tests (especially test 35D1) other unstable modes are also apparent, as distinct peaks can be seen at frequencies other than the unstable mode (or its higher harmonics). Note also the change in test 35D1 from the unstable mode of 1721 Hz early in the test to 1233 Hz later in the test. Not only does the dominant peak change from one mode to the other, but the higher harmonics also switch.

#### 1.4. Study Objectives and Outline

The primary objective of this research is to use computational analysis and experimental validation to obtain a better understanding of high frequency combustion instability. Eventually, it is anticipated that computational models will be used as design tools for the prediction of combustion instability in rocket engine development. This research is designed to work towards that goal. This research should also aid in the design and interpretation of future experiments dealing with high frequency combustion instability.

Because of the complexity inherent in combustion instability, the computational model closely follows the Purdue experiment that was summarized in Section 1.3. At each step of the research, the computational conditions and results are closely compared to the experimental data in order to verify that there is appropriate agreement.

The thesis is outlined as follows. Chapter two explains the computational model, clarifying the various assumptions and simplifications that have been employed. This includes using a one-dimensional model with a source term to

simulate the steady combustion of the experiment. The geometry and mean conditions of the model are matched to the experimental conditions and a means of unsteady forcing is developed.

In chapter three, small amplitude forcing is employed to ensure that the computational model can accurately predict the acoustic modes of the experimental configuration. To verify this, the frequency response and mode shapes of the computational and experimental results are compared. With this level of forcing, only the frequencies of the unsteady pressure are being validated.

In chapter four, the forcing is increased to large amplitudes in order to simulate the non-linear behavior of the experimental data. At this point the objective is not to predict instability, but to show that the same limit cycle behavior can be produced by specifying an appropriate amount of forcing. Power spectral density (PSD) plots of the computational and experimental data are compared in order to validate both frequency and power amplitude for each chamber length case.

Chapter five examines the effects of modifying the boundary conditions of the computational domain. The results of using simplified boundary conditions (such as those used in analytical models) can be compared against the original boundary condition results to determine their accuracy. This can give an indication of how much confidence to place in the analytical models that use these simplified boundary conditions. Using simplified boundary conditions may also allow computational results to be obtained more quickly for a comparable amount of accuracy. This is investigated using admittance conditions for the downstream boundary. Another reason for modifying the boundary conditions is to attempt to better match the conditions of the experimental configuration. This is explored for the upstream boundary.

Chapter six begins developing and testing basic response functions for combustion instability prediction. This entails adding a source term to simulate the unsteady heat release of combustion. The instability behavior is then

observed for various levels of heat release. The computations are also forced with initial broadband forcing to simulate acoustic noise. This is then turned off and the response function is turned on so that the instability can occur at any acoustic mode. These results are validated with the experimental data for each chamber length case.

The final chapter summarizes and concludes the research. It also gives recommendations for how the research should be extended for possible future work. The acoustic modes for all chamber lengths and all output positions are shown in the appendices. Appendix A shows the acoustic modes corresponding to the inflow boundary configuration. Appendix B shows the acoustic modes corresponding to the wall boundary condition with an oxidizer source configuration.

## CHAPTER 2. COMPUTATIONAL MODEL

The computational code that is used for this research was derived from a research code designated as GEMS (General Equation and Mesh Solver). Although based in computational fluid dynamic analysis, the code has also been applied in various applications such as combustion and conjugate heat transfer. The code is written in Fortran95 and uses MPI for parallel processing. GEMS can do computations in one, two, or three dimensions. Along with the Navier-Stokes equations, GEMS can also apply combustion kinetics equations and the Maxwell equations. The numerical algorithm and computational code for GEMS are discussed in greater detail in refs.<sup>22-24</sup>.

### 2.1. Governing Equations

The relevant equations for this research are the unsteady Navier-Stokes equations supplemented by pertinent species conservation equations. Any number of species equations can be accommodated in the GEMS code. The unsteady, three-dimensional Navier-Stokes equations combined with the species equations are,

$$\frac{\partial Q}{\partial t} + \frac{\partial E_i}{\partial x_i} = H + \frac{\partial V_i}{\partial x_i} \quad \text{Eq. 2.1}$$

where

$$Q = \begin{pmatrix} \rho \\ \rho u_i \\ e \\ \rho Y_m \end{pmatrix} \quad \text{Eq. 2.2}$$

$$E_i = \begin{pmatrix} \rho u_i \\ \rho u_i u_j + \delta_{ij} p \\ (e + p) u_i \\ \rho u_i Y_m \end{pmatrix} \quad \text{Eq. 2.3}$$

The  $H$  vector in Equation 2.1 is a source term and is defined in Section 2.2. The  $dV/dx$  term represents the viscous diffusion in the system.

From the experimental results that were discussed in Section 1.3.3, it was shown that combustion instability was due to longitudinal modes, or modes that oscillate in the same direction as the flow. Even though the geometry of the system is axially-symmetric, the essential acoustic excitation can be captured using one-dimensional analysis. The one-dimensional unsteady Euler equations can be employed to simplify the computational grid and greatly decrease the computational cost. In the one-dimensional approximation, Equation 2.1 simplifies to,

$$\frac{\partial Q}{\partial t} + \frac{\partial E}{\partial x} = H \quad \text{Eq. 2.4}$$

where the subscripts in the  $Q$  and  $E$  vectors simplify to  $i = j = 1$ .

One-dimensional analysis cannot capture the complex turbulent behavior governing combustion in the domain. The combustion must be accounted for by using lower order models which simulate the heat release of the system. To simplify the modeling of combustion, the steady (mean) heat release is modeled separately from the unsteady (oscillating) heat release. This greatly decreases the computational expense because the steady-state solutions need only be solved for once for each chamber length and can then be input as the initial

condition for all subsequent unsteady runs. The unsteady run will converge much more rapidly because the mean properties have already converged, leaving only the unsteady oscillations that need to converge. The steady heat release, which affects the mean flow conditions, is addressed in this section and in Section 2.2. The unsteady heat release, which is an essential part of accurately predicting combustion instability, is addressed in CHAPTER 6.

For the steady heat release, a single step, two species model is chosen for ease of implementation. This means that  $m = 1$  in the fourth term of Equation 2.3, since there is only one additional species. Using only two species for the steady combustion model is justified since the main objective of the research is to investigate unsteady behavior leading to combustion instability. The steady combustion model need only match the steady-state mean conditions of the experiment.

In the experimental configuration, fuel was added near the injector/chamber interface (see Section 1.3.2). In order to match the experiment, the fuel in the computational model should be added near the same axial location. Since the computational model is one-dimensional, the only boundaries are the inlet and outlet boundaries. The only way to add fuel at the injector/chamber interface is to use a source term. The two species can then be defined as unburned oxidizer and burned products, and the fuel addition can be accounted for by using the source term. This source term is shown in Equation 2.4 as the  $H$  vector. The formulation of this source term is described in the next section.

## 2.2. Source Term for Steady Combustion

In order to decrease the expense in modeling combustion, the heat release of combustion has been split into steady and unsteady components. The spatially varying, steady combustion only influences the steady-state mean solutions. This is modeled using a source term, designated as  $H$  in Equation

2.4. The source term is necessary because the fuel is being introduced at an axial location other than the boundaries. The spatially varying, unsteady combustion affects the oscillation of the flow conditions and is modeled using heat release response functions. The first steps in formulating and using response functions are examined in Section 6.1. The current section deals with the development of the  $H$  source term.

The equilibrium mixture ratio between the fuel and the oxidizer is obtained from the CEA equilibrium code for the experimental conditions. This is given as an input into the computational model. The relationship between the fuel and oxidizer is defined as,

$$\dot{\omega}_f = C_{f/o} \dot{\omega}_{ox} \quad \text{Eq. 2.5}$$

where  $\dot{\omega}_f$  is the fuel mass concentration consumption rate,  $\dot{\omega}_{ox}$  is the oxidizer mass concentration consumption rate, and  $C_{f/o}$  is the equilibrium mixture ratio.

Although the addition of the fuel will be accounted for by the source term, the fuel itself is not introduced as a separate species. This means that the source term does not add an independent species to the system. Instead, the source term controls the reaction process (including the consumption of the oxidizer species) and adds representative fuel properties to the flow. This is equivalent to saying that as soon as the fuel is added it reacts with the oxidizer to form combustion products. Only two species need be represented in the governing equations, so the following mass fraction relationship is still valid,

$$Y_{Pr} = 1 - Y_{ox} \quad \text{Eq. 2.6}$$

where  $Y_{Pr}$  is the product mass fraction and  $Y_{ox}$  is the oxidizer mass fraction.

The use of Equation 2.5 allows the influence of the fuel to be defined in terms of the oxidizer species. Using the equilibrium mixture ratio, the combustion source term vector can be defined as,

$$H = \begin{pmatrix} \dot{\omega}_f \\ \dot{\omega}_f u \\ \dot{\omega}_f h_0 \\ -\dot{\omega}_{ox} \end{pmatrix} = \begin{pmatrix} C_{f/o} \dot{\omega}_{ox} \\ C_{f/o} \dot{\omega}_{ox} u \\ C_{f/o} \dot{\omega}_{ox} h_0 \\ -\dot{\omega}_{ox} \end{pmatrix} \quad \text{Eq. 2.7}$$



where all chamber conditions (such as  $u$  and  $h_0$ ) are mean quantities.

The first three terms in Equation 2.7 account for the addition of fuel mass, momentum, and energy into the flow. The last term accounts for the chemical conversion of oxidizer into products. Note that Equation 2.5 has been applied so that only the oxidizer mass production rate is used. The stagnation enthalpy in the third term is defined as,

$$h_0 = h + \frac{1}{2}u^2 = h_{ox} Y_{ox} + h_{Pr} Y_{Pr} + \frac{1}{2}u^2 \quad \text{Eq. 2.8}$$

where the enthalpies of the oxidizer and products are,

$$\begin{aligned} h_{ox} &= h_{f,ox}^0 + c_{p,ox} (T - T_{ref}) = c_{p,ox} (T - T_{ref}) \\ h_{Pr} &= h_{f,Pr}^0 + c_{p,Pr} (T - T_{ref}) \end{aligned} \quad \text{Eq. 2.9}$$

The  $c_{p,ox}$  and  $c_{p,Pr}$  terms in Equation 2.9 are the constant pressure specific heats, which are assumed to be constant for the current formulation.

For the model, the heat of formation of the oxidizer has been arbitrarily set to zero. The heat of formation of the products has been set so as to match the flame temperature in the experimental setup. To obtain the experimental flame temperature of about 2450 K, the heat of formation,  $h_{f,Pr}^0$ , is equal to 4.47e6 J/kg. The oxidizer consumption rate from the combustion source term is defined as:

$$\dot{\omega}_{ox} = k_f \rho Y_{ox} S \quad \text{Eq. 2.10}$$

where  $k_f$  is the global rate coefficient and

$$S = 1 + \sin\theta = 1 + \sin\left(-\frac{\pi}{2} + \frac{x - l_s}{l_f - l_s} 2\pi\right) \quad \text{Eq. 2.11}$$

The global rate coefficient,  $k_f$ , is determined through empirical means to give an appropriate temperature profile. The spatial extent of the fuel addition (and thus the combustion zone) is controlled through the use of the  $S$  term in Equation 2.11. The distribution of the  $S$  term uses a sine wave function which approximates a normal distribution. This causes the oxidizer mass fraction to be equal to one at the start of the combustion zone and almost equal to zero at the end of the combustion zone. The  $l_s$  and  $l_f$  parameters designate the start and finish of the combustion zone, respectively. For all of the computational studies in

this thesis,  $l_s = 6.62$  inches (0.1681 m, near the injector/chamber interface) and  $l_f = 12.0$  inches (0.3048 m, or 5.18 inches into the chamber region). The  $S$  distribution (top) and resultant temperature profile (bottom) are shown in Figure 2.1 for a 25 inch chamber. Note that the axial position has been plotted so that the injector/chamber interface occurs at the zero axial position.

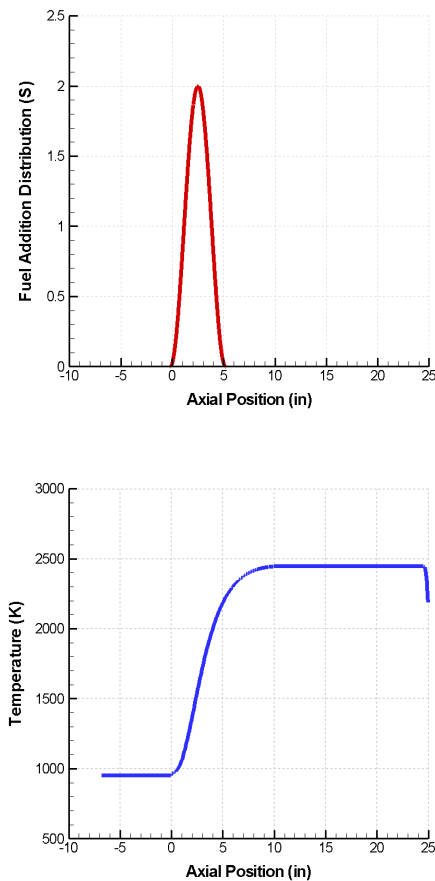


Figure 2.1: The top plot shows the  $S$  distribution, as defined by Equation 2.11. The bottom plot shows the resultant temperature profile.

Using this combustion source term allows the steady-state conditions in the chamber to be closely matched to the mean experimental conditions.

## 2.3. Computational Domain

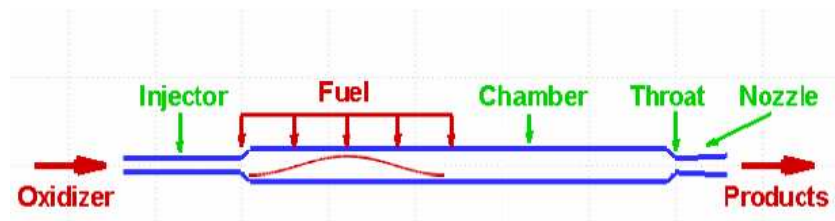
This section explains the geometry, grid spacing, and nozzle configuration of the system, along with a brief explanation of the boundary conditions. A more detailed discussion of the boundary conditions can be found in CHAPTER 5. Note that in the code, the injector head-end corresponds to the zero position and the mode shape results are output in meters. In order to be consistent with the experiment, for post processing the injector/chamber interface is designated as the zero position and the units are changed to inches (see Figure 2.2). This causes the injector to be in the negative axial position region.

### 2.3.1. Geometry

The geometric domain has been designed to include the important elements of the experimental configuration. In the experiment, such elements as the oxidizer and fuel manifolds were designed to be decoupled from the main injector/chamber response. This was done by creating a relatively large pressure drop from the manifolds to the injector. From power spectral density (PSD) analysis performed on the experimental results, it was found that the response in the fuel and oxidizer manifolds were much smaller than the response in the injector and chamber.<sup>10</sup> Therefore, the fuel and oxidizer manifolds were assumed to have a negligible impact on the factors leading to combustion instability, and were left out of the computational domain.

The computational domain includes the injector, the chamber, and the nozzle. The geometric extent of the domain is shown in Figure 2.2 in inches for a 25 inch chamber section. The top drawing shows a scaled down, but proportional, version of the geometry. For ease in dimensioning, the bottom drawing of Figure 2.2 shows a radially stretched version of the geometry. In other words, the x and y axes of the bottom drawing have different scales, even though they are both in inches.

## Proportional Geometry



## Radially Stretched Geometry

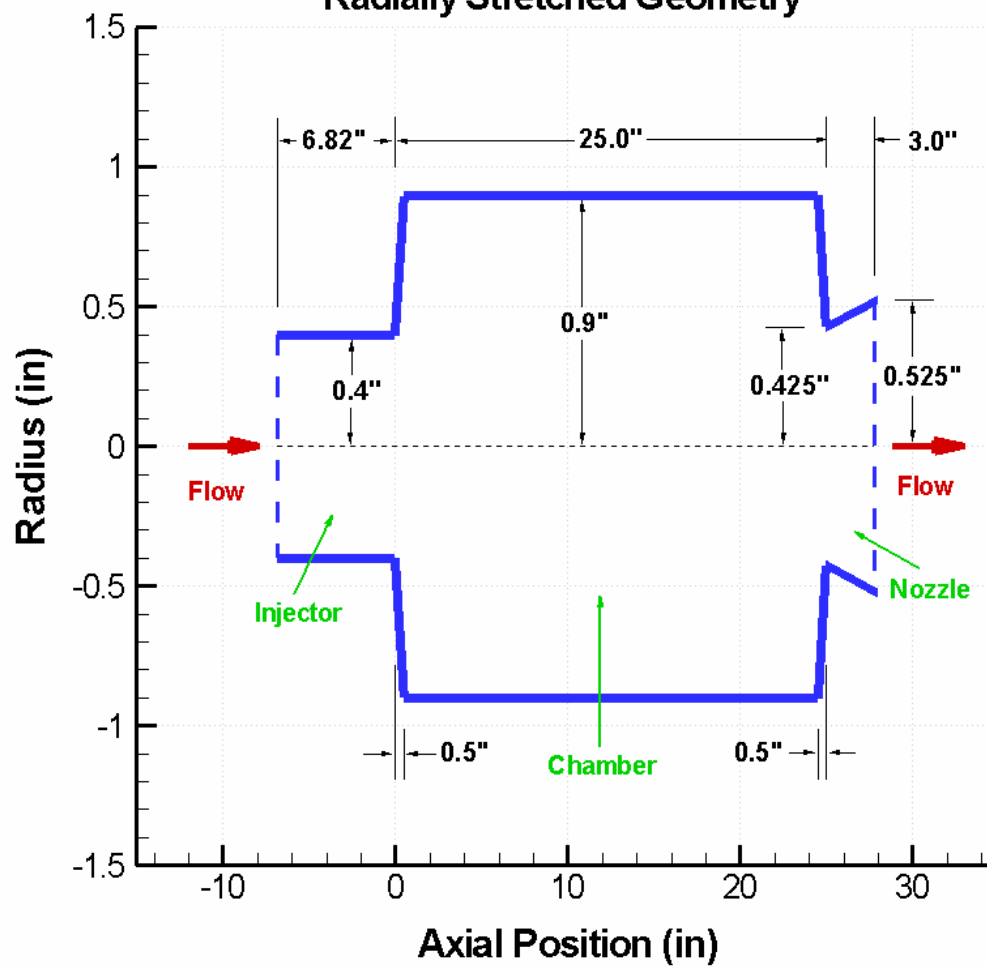


Figure 2.2: Computational domain shown with a proportional view of the geometry (top) and a radially stretched and dimensioned version of the geometry (bottom)

Note that in Figure 2.2, the injector/chamber interface has been placed at the axial location corresponding to zero. This was employed to match the nomenclature of the experiment. It also has the advantage that the injector/chamber interface is always at the same coordinate, regardless of the injector or chamber lengths. This same designation will be used in plotting the mode shapes in later chapters. The chamber length varies according to the experimental tests from 15, 20, 25, and 35 inches (0.381, 0.508, 0.635, and 0.889 meters respectively). The injector length was held constant for this research, although it has been varied in other studies.<sup>25</sup>

The output locations for frequency analysis are shown in Figure 2.3. These were chosen to match the experimental transducer locations.

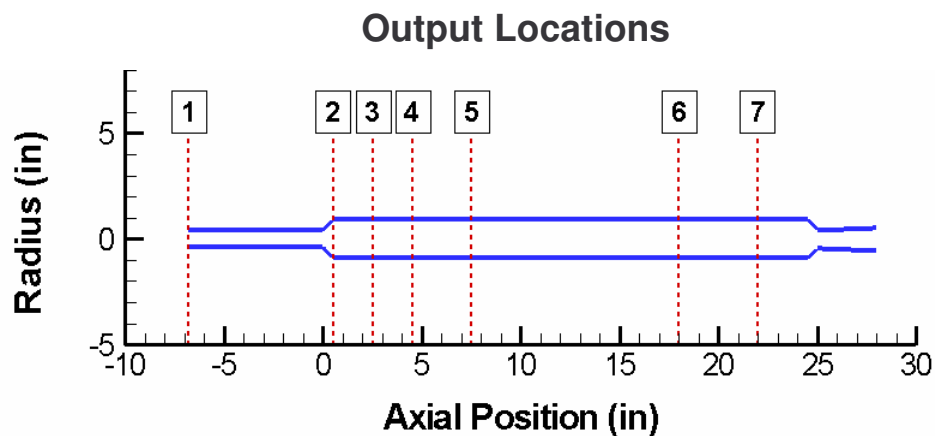


Figure 2.3: The output locations for frequency analysis, corresponding to axial positions of -6.82, 0.5, 2.5, 4.5, 7.5, 18.0, and 22.0 inches

The output locations in Figure 2.3 allow pressure data to be collected at a single axial position for any given amount of time. Frequency analysis, such as fast Fourier transform (FFT) or power spectral density (PSD) analysis, can then be applied to determine the amplitude and frequency of the oscillating pressure. Since the objective of this research is to validate the computational results with the experiment data, the output locations shown are the primary locations used

throughout this thesis. The output at locations one (the injector head-end) and two (injector/chamber interface) are used most frequently to analyze the computational results.

Any number of locations (not exceeding the number of grid points) can be designated as output locations in the computational domain. For mode shape analysis, pressure is output to every grid point along the axial position at a given time. This is done for multiple times during the period of the oscillation. The full mode shape is constructed by putting all of these together on the same plot. Through this approach, the oscillation of pressure (or velocity) in the system can be viewed. For this research, the axial data was always output at 32 times during the cycle. This value was chosen because it gives a close approximation to the envelope of the mode shape while still allowing the individual lines to be distinguishable. Representative mode shapes are shown in Figure 2.7. For linear analysis, mode shapes are usually obtained at a particular frequency. For non-linear analysis, multiple frequencies (corresponding to higher harmonics) may be present in the mode shape.

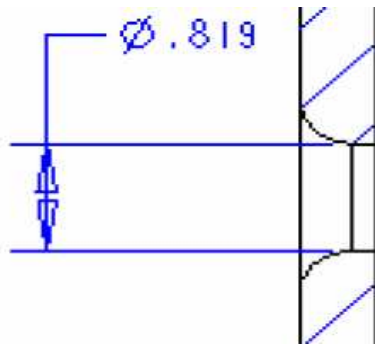
In the actual experimental setup, the interface between the injector and chamber exists as a step change (a vertical wall). However, for one-dimensional calculations, it is convenient to have some finite length in changing from one diameter to another. This minimizes the need for excessive grid points in order to resolve the solution at the interface. As shown in Figure 2.2, the diameter changes linearly from the injector diameter to the chamber diameter over an axial distance of 0.5 inches (0.0127 m). This length corresponds to 2% of the entire chamber length for a 25 inch chamber. Because this is such a small percentage, it is not expected to have a significant effect on the solutions.

### 2.3.2. Nozzle Configuration

The computational nozzle is a converging/diverging DeLaval nozzle. The nozzle is the only element that does not match the experiment closely in its

geometric dimensions. In the experiment, the nozzle is very short (only 0.5 inches) and only contains the converging section. The converging portion of the computational nozzle matches the axial length of the experiment (0.5 inches), but does not have the same profile. Instead of a rounded contour, the computational nozzle varies linearly from the chamber radius to the throat radius. The length of the computational diverging section (which is non-existent in the experiment) is 3 inches (0.0762 m) long and varies linearly over this distance. The throat radius of the nozzle is 0.425 inches (0.0108 m) and the exit radius is 0.525 inches (0.0133 m). The nozzle geometries are shown together in Figure 2.4. Note that the computational nozzle is bounded by the red dashed lines.

### Experimental Nozzle



### Computational Nozzle

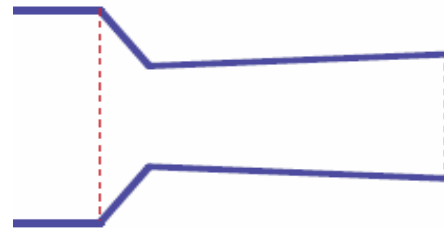


Figure 2.4: Comparison between nozzle geometry for the experiment (left) and the computational model (right). The experiment only has a converging section, while the computational model has both converging and diverging sections.

The extra diverging section helps to ensure that the flow remains choked throughout the entire run. As will be shown in Section 4.1.2, the Mach number at the throat oscillates about 1.0 during the unsteady calculations. This means that the flow at the throat is continually going back and forth between subsonic and supersonic flow. If only the converging section were present, the exit boundary condition would continually be oscillating between being dependent on the back pressure and being independent of the back pressure (see Section 5.1.2). The

diverging portion of the nozzle causes the Mach number at the exit to always be supersonic and thus be independent of the back pressure. Having just a converging nozzle would also require adding an external computational domain, which is impractical for one-dimensional computations.

The effect of the nozzle on combustion instability is mainly to define the boundary conditions of the waves in the chamber and as a source of damping of the longitudinal waves.<sup>41</sup> Although the addition of the diverging section may have some impact on the overall damping of the system, it does not affect the chamber or injector acoustics. For acoustic analysis, the results in the nozzle section are ignored. There are no pressure output locations in the nozzle and the mode shapes stop at the end of the combustion chamber. The effect of the additional diverging section should be taken into account when quantifying the amount of damping in the system. Because of the additional section, the damping of longitudinal waves may be greater in the computational model than in the experimental configuration.

### 2.3.3. Grid Placement and Convergence

Grid convergence studies were done for the same geometry and conditions and found second-order accuracy as the grid points were increased.<sup>25</sup> Further comparisons were also done to ensure that the number of grid points was sufficient to accurately represent the solution. The steady-state solutions for a 25 inch chamber are shown in Figure 2.5 for velocity, pressure, temperature, and the oxidizer mass fraction for 250, 500, 1000, and 2500 grid points. The input parameters necessary to obtain these solutions are given in Section 2.4. The accuracy of these solutions (with regards to the experiment) is also discussed in that section. At this time the solutions are shown only for grid convergence purposes.



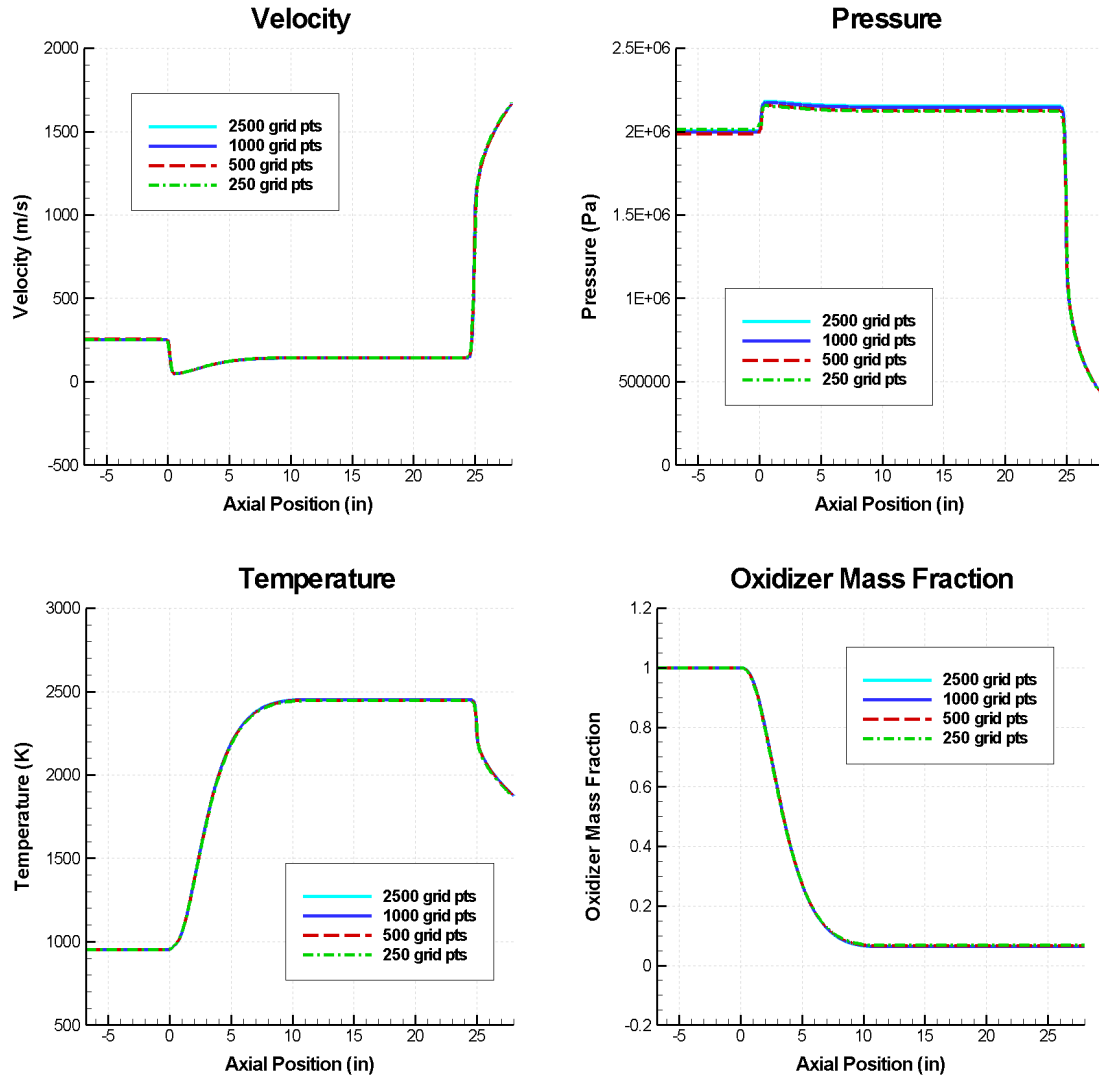


Figure 2.5: Steady-state solutions of velocity, pressure, temperature, and the oxidizer mass fraction for 250, 500, 1000, and 2500 grid points

All of the solutions shown in Figure 2.5 appear grid converged except the pressure plot. Even for the steady-state pressure solution, the maximum relative error between the 250 and 2500 grid point cases is less than 1.5% at any axial location.

Grid convergence studies were also done using unsteady forcing, as described in Section 2.5. Since instability is the main focus of this research, most of the solutions shown in this thesis are unsteady solutions. These include

frequency response and mode shape plots of the oscillating pressure in the computational domain. A more detailed discussion of these solutions is given in CHAPTER 3. In this section, the unsteady solutions are shown only for grid resolution purposes. A 25 inch chamber was used with broadband mass flow forcing at 0.01% of the mean mass flow-rate. The fast Fourier transform (FFT) of the pressure response at the injector head-end (position 1) is shown in Figure 2.6 for 500 and 1000 grid points.

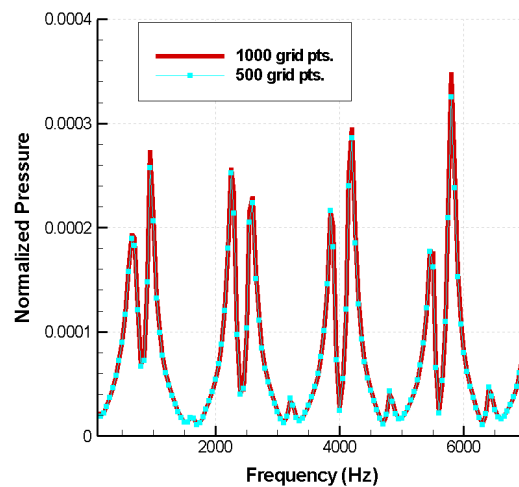


Figure 2.6: FFT plot comparison for 500 and 1000 grid points for a 25 inch chamber at position 1. Broadband mass flow forcing was used at 0.01% of the mean mass flow-rate.

There is very good agreement between the two different grid resolutions at this axial position. Mode shape plots are also compared in Figure 2.7 for frequencies of 950 Hz and 1650 Hz (the second and third peaks in Figure 2.6). The 500 grid point solutions are shown on the left, the 1000 grid point solutions on the right.

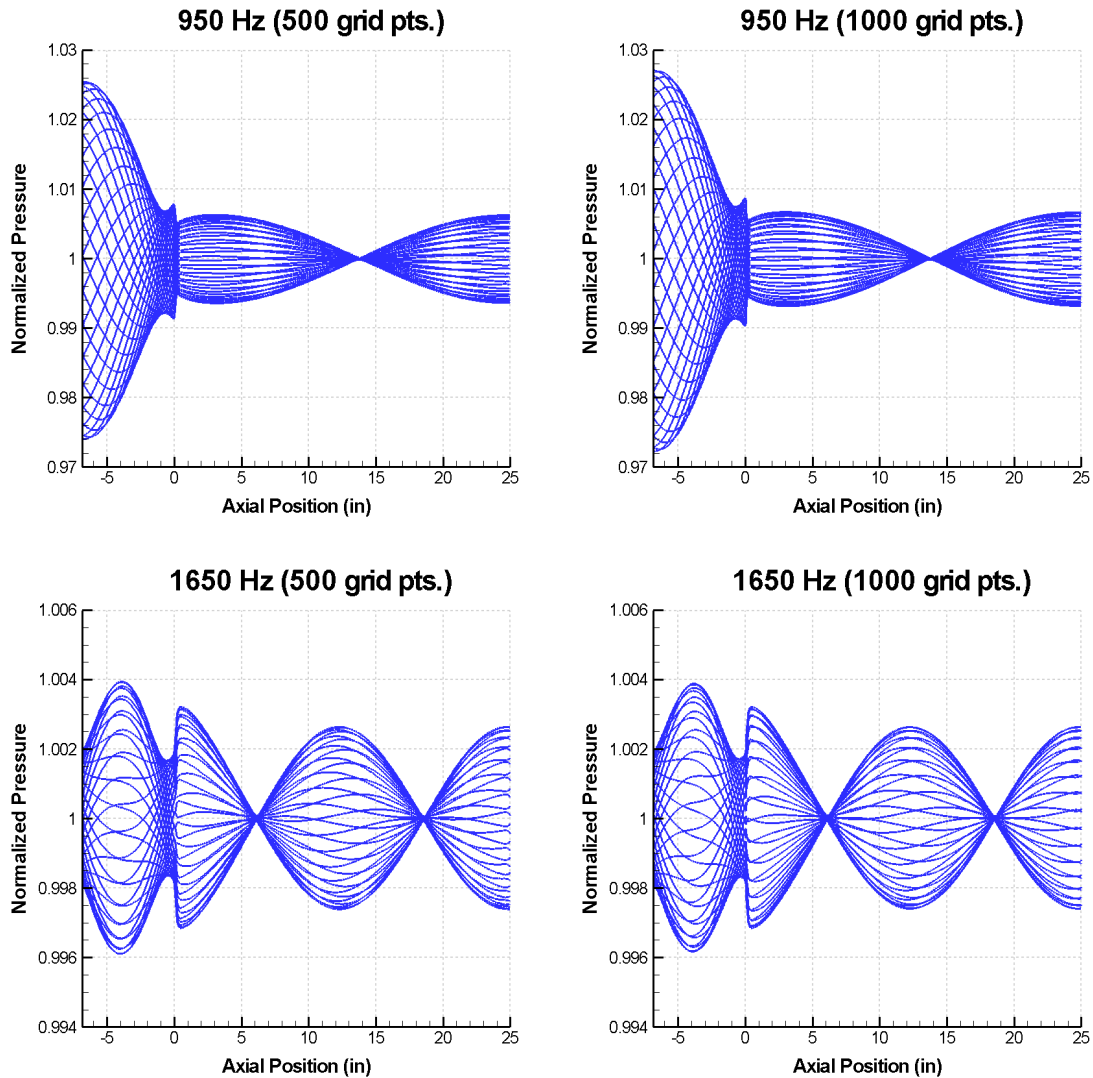


Figure 2.7: Mode shape comparisons for 950 Hz and 1650 Hz for 500 grid points (left) and 1000 grid points (right)

The mode shapes are almost identical for the two different grid resolutions. From Figure 2.6 and Figure 2.7, the unsteady solutions appear to be grid converged for 500 grid points. Because the computations become more expensive as the number of grid points increases, the accuracy of the solution is balanced by the cost of the computations. For the research in this thesis, a 500 point grid was chosen for the 25 inch chamber case. With this grid spacing, there

is a maximum relative error of about 1% in the steady-state solutions shown in Figure 2.5. The error in the unsteady solutions is less than 1%.

For parametric studies of the chamber length, a fixed grid point spacing was chosen and held fixed for all chamber lengths. For the 500 point base case (25 inch chamber length), the spacing between grid points is 0.0696 inches (1.77 mm). The number of grid points for each chamber length case was then set according to this spacing. An additional grid point was also added outside of the domain, corresponding to a 'ghost cell'. This extra cell allows for a wider range of possible boundary conditions, such as a derivative at the domain boundary. For the 15, 20, 25, and 35 inch chamber cases, the number of grid points used for each case is 357, 429, 501, and 645 points, respectively. All other geometry and conditions remain the same as the chamber lengths are varied.

Because all of the steady-state solutions level out to constant values by the 15 inch mark, changing the chamber length corresponds to simply adding or subtracting grid points in this constant value section. The grid convergence behavior doesn't change since the spacing in all of the other regions is the same. This ensures that the accuracy for each of the chamber length cases is also the same as the 500 point grid case.

#### 2.3.4. Boundary Conditions

Because the computational model is one-dimensional, boundary conditions need only be specified at the inlet and exit of the flow. As shown in the previous sections, this corresponds to the injector head-end and the nozzle exit. For inlet subsonic flow, two boundary conditions must be specified. These are traditionally either stagnation pressure and stagnation temperature, or stagnation temperature and the mass flow-rate. In the experiment, the oxidizer enters the injector through a choked orifice. This corresponds physically with specifying the stagnation temperature and the mass flow-rate. In order to match the experiment, these two conditions are chosen as the inlet boundary condition inputs. For the

outflow boundary, the flow is supersonic due to the diverging nozzle. For exiting supersonic flow in a one-dimensional model, no boundary inputs are specified because the flow conditions at the outflow boundary are completely controlled by the upstream flow. Therefore, the outflow conditions are determined by the governing equations. The computational reasons for using these boundary conditions are discussed in greater detail in CHAPTER 5 and in Merkle<sup>26</sup>.

#### 2.4. Inputs and Steady-State Solutions

The base case for the computational studies corresponds to experimental test 25D1r (also designated as test 11) in Table 1-1. This has a chamber length of 25 inches and an unstable frequency of 1660 Hz. The input properties and conditions for the 25 inch chamber case length are shown below in SI units.

Table 2-1: Input properties and conditions for the 25 inch chamber base case

<b>Input Parameter</b>	<b>Injector</b>	<b>Chamber</b>
Molecular Weight (kg/kmol)	22.1	21.3
Ratio of Specific Heats	1.27	1.19
Dynamic Viscosity (N*s/m <sup>2</sup> )	4.0e-4	4.0e-4
Length	0.1732 m (6.82 in)	0.635 m (25 in)
Stagnation Temperature (K)	970	—
Oxidizer Flow-rate (kg/s)	0.459	—
O/F Ratio	—	6.20

For the various studies performed in this thesis, the base case is run and analyzed first. The computations are extended to the other chamber length cases (15, 20, and 35 inches) when experimental validation is desired. The inputs for the other chamber length cases are similar to the values in Table 2-1. Along with

varying the chamber lengths, the oxidizer flow-rates and O/F ratios have been modified for each case to more closely match the values from the experimental tests. All other inputs are identical to the values in Table 2-1.

Table 2-2: Specific input properties for different chamber length cases

<b>Experimental Test</b>	<b>Chamber Length (in)</b>	<b>Oxidizer Flow-rate (kg/s)</b>	<b>O/F Ratio</b>
15D1 (15)	15	0.462	6.24
20D1r (16)	20	0.464	6.27
25D1r (11)	25	0.459	6.2
35D1 (17)	35	0.464	6.27

Using the computational model and the input conditions, steady-state solutions were obtained for all chamber lengths. The steady-state solutions for the 25 inch chamber case are shown in Figure 2.9 for pressure, velocity, temperature and oxidizer mass-fraction. The top part of Figure 2.2 has been repeated in Figure 2.8 for convenience in interpreting the steady-state solutions. The axial location before zero corresponds to the injector region. The injector/chamber interface is located at zero. The convergent section of the nozzle begins at the axial position of 24.5 inches.

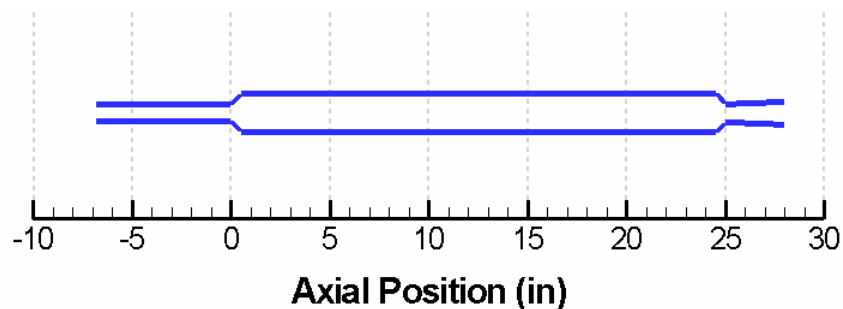


Figure 2.8: Axial geometry of the computational domain

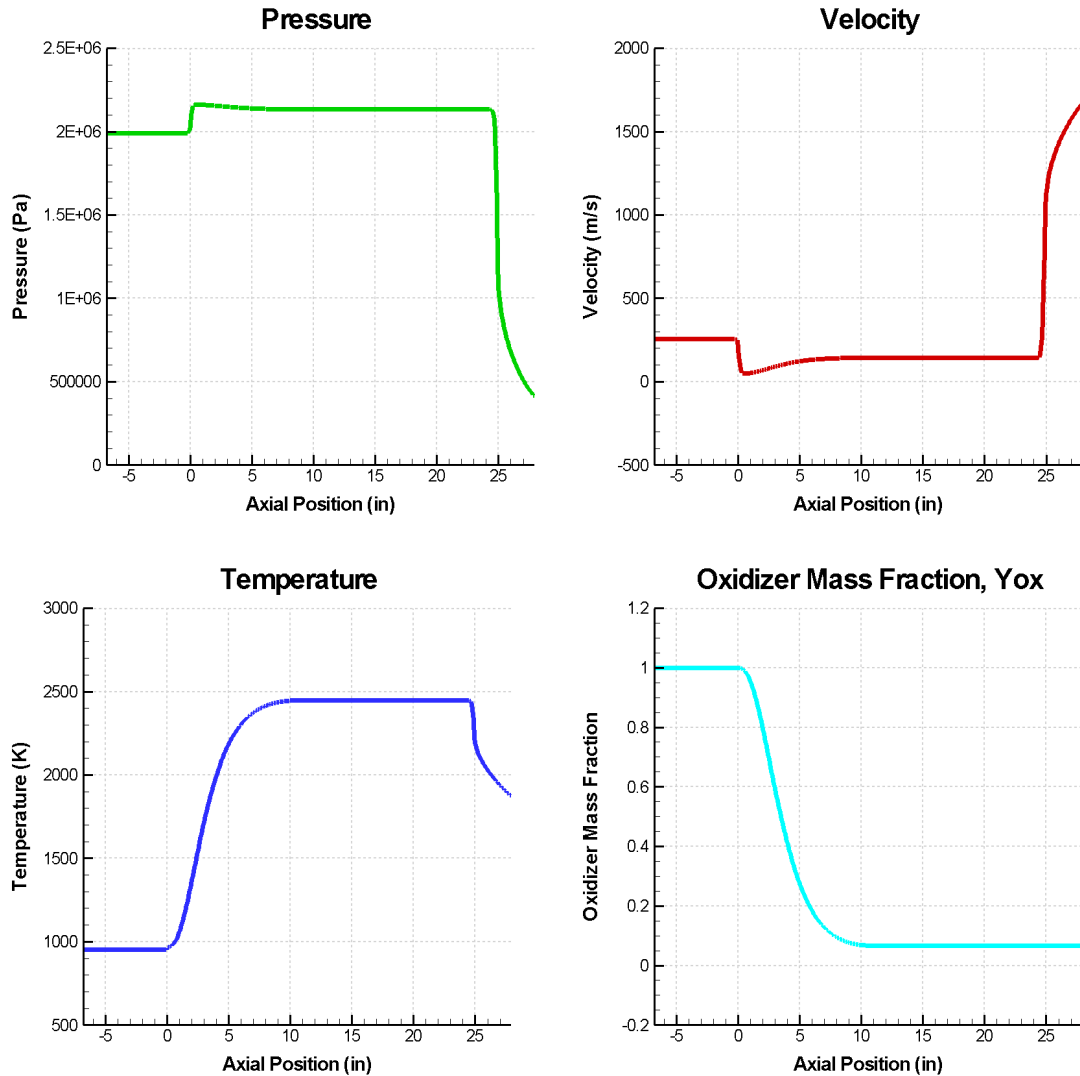


Figure 2.9: Steady-state solutions for the 25 inch chamber case

The steady-state solutions appear as expected. The largest gradients are seen at the injector/chamber interface and in the converging section of the nozzle. The combustion source term appears to accurately model steady heat release, as the temperature profile increases from the injector temperature to the constant chamber temperature and the oxidizer mass-fraction decreases from one to less than 0.1. The constant values in the injector and chamber are tabulated below for various flow conditions.

Table 2-3: Steady-state constant solutions in the injector and chamber regions for the 25 inch chamber case

	<b>Injector</b>	<b>Chamber</b>
Pressure (Pa)	1.990e6	2.133e6
Velocity (m/s)	254.6	143.7
Temperature (K)	951.7	2449
Mass Flow-rate (kg/s)	0.459	0.527
Mach Number	0.378	0.135

Validation for the steady-state solutions can be done by comparing Table 2-3 with the experimental mean conditions in Table 1-1. The computational steady-state solutions match the experimental mean conditions fairly well, although the computational chamber pressure is at the lower end of the range of experimental chamber pressures. The rest of the thesis will deal with the dynamic solutions that are obtained by introducing an initial perturbation into the flow. The forcing of this perturbation is described in the next section.

## 2.5. Broadband Mass-flow Forcing

In actual rocket engines, perturbations in the flow occur at a range of frequencies due to various transient phenomena, such as atomization, vaporization, combustion kinetics, etc. Acoustic modes are then excited by some of those frequencies, dependent on the geometry and conditions of the system. The resonance of those acoustic modes can then couple with the heat release to cause instability in the flow. Because combustion instability involves the coupling of acoustic modes and combustion heat release, the determination of these acoustic modes is essential in modeling instability.

Because the detailed unsteady dynamics of the flow (such as atomization, vaporization, etc) are not characterized by the present one-dimensional



computational model, the perturbations which include the various frequencies must be introduced in some other way. The easiest way to introduce these perturbations is through an inlet boundary condition. Otherwise, another source term would have to be added to the model to produce the perturbations. As discussed in Section 2.3.4, the stagnation temperature and mass flow-rate are specified as the inlet boundary conditions. The mass flow-rate is a function of the pressure, temperature, and velocity, so any oscillation in these variables will also cause an oscillation in the mass flow-rate. Because of its susceptibility to perturbations, the mass flow-rate is chosen as the oscillatory input.

Introducing a range of frequencies into the perturbation can be done using random forcing. However, random forcing requires an excessively long run time to approximate a “white” Fourier spectrum. If the random forcing is not run for long enough, the acoustic mode frequencies will not be equally represented. Random forcing is then either very computationally expensive or potentially inaccurate.

A more efficient method is to introduce a range of frequencies through broadband forcing. An infinite number of frequencies cannot be represented, so a frequency resolution must be chosen. The various frequencies then occur at integral multiples of this specified frequency resolution. This means that the mode frequency can only be determined to the precision of the mode resolution. For example, if a frequency resolution of 50 Hz is specified, then the broadband forcing will excite frequencies of 50 Hz, 100 Hz, 150 Hz, etc. A frequency of 75 Hz could not be obtained with this resolution, although the frequency resolution can, in principle, be changed to obtain the degree of desired precision. Broadband forcing also guarantees that all frequencies within the frequency range are equally represented. For the computational model, the broadband forcing will be introduced by using the following definition,

$$\dot{m}(t) = \dot{m}_{\text{mean}} \sum_{n=1}^N (1 + \varepsilon \sin[2\pi(f_0 + n\Delta f)t]) \quad \text{Eq. 2.12}$$

In the above,  $f_0$  is the initial frequency,  $\Delta f$  is the frequency interval, and  $\epsilon$  is the magnitude of the perturbation. The perturbation takes the form of a sine wave. The N integer specifies the total number of forced modes and sets the maximum frequency that will be forced. For all of the experimental results, the unstable frequencies were below 2000 Hz, and 6000 Hz was high enough to capture the first two higher harmonics of the unstable frequency. The maximum frequency that will be forced for the computational model is chosen to be 7000 Hz. The N integer is determined by dividing the maximum frequency (7000 Hz) by the frequency interval (50 Hz). This results in an N of 140 modes. For most of the computations in this thesis, the  $\omega_0$  value has been set equal to zero and a frequency interval ( $\Delta f$ ) of 50 Hz has been used. Section 3.3.2 examines the effects of varying the frequency interval. The frequency interval determines the frequency resolution, so the acoustic modes are not determined any more precisely than within 50 Hz when this resolution is applied.

The non-linearity of the response is determined by the size of the  $\epsilon$  term. If  $\epsilon$  is equal to zero, there is no perturbation in the flow and the steady-state solutions will be obtained. By running cases at a range of  $\epsilon$  values, the general effects of higher amplitude perturbations were determined. Up to an  $\epsilon$  of about 0.1% of the mean mass flow-rate, the dynamic response has essentially linear characteristics. Mass flow forcing below 0.1% is defined as “small” amplitude forcing. Above an  $\epsilon$  of 1% of the mean mass flow-rate, the dynamic response exhibits non-linear characteristics. Mass flow forcing above 1% is defined as “large” amplitude forcing. The range from 0.1% to 1% is transitional in nature and is difficult to characterize one way or the other. Single mode forcing with a range of  $\epsilon$  values is demonstrated in Section 4.1.1 to clarify these results.

A representative broadband forced pressure history plot is shown in Figure 2.10 for a 25 inch chamber with 0.01% mass flow forcing. The frequency interval is 50Hz, so the period of the oscillations is 0.02 seconds. The pressure trace was taken at the injector/chamber interface (position 2). Multiple frequencies are clearly evident in the oscillations.

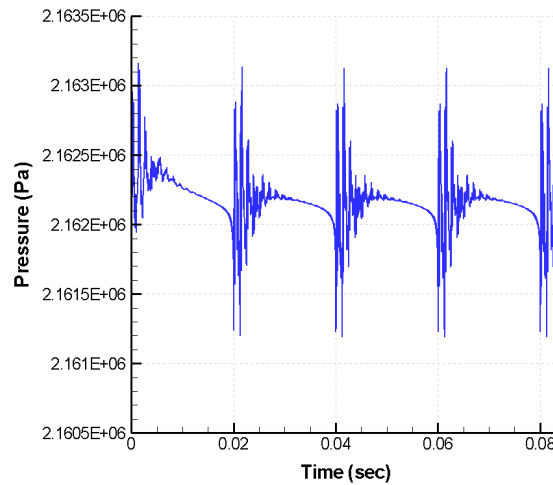


Figure 2.10: Pressure history at position 2 with broadband forcing at 0.01% of the mass flow-rate. The frequency interval is 50 Hz.

CHAPTER 3 will apply small amplitude, broadband forcing to find the acoustic modes of the system. Single frequency forcing at each of these modes is then applied in order to obtain the mode shapes. CHAPTER 4 will apply large amplitude, single frequency forcing to test how well the model is able to handle non-linear behavior. In the experiment, one of the linear acoustic modes couples with the heat release and subsequently grows to a large amplitude limit cycle. This causes the combustion instability to show non-linear characteristics in the pressure response. The application of both small and large amplitude forcing is necessary to accurately model combustion instability.

## CHAPTER 3. SMALL AMPLITUDE, LINEAR FORCING

For high frequency combustion instability to occur, the heat release must couple with the acoustic modes (see Section 1.1). These acoustic modes are obtained by performing small amplitude, broadband forcing, as described in Section 2.5. The mode shapes for each particular mode can then be obtained by using small amplitude, single frequency forcing. Once these linear modes are found, large amplitude forcing can be employed to simulate the non-linear behavior of combustion instability. Large amplitude forcing is described in CHAPTER 4. After it has been demonstrated that the model can replicate non-linear behavior, response functions can be added to simulate the unsteady heat release. Modeling of the acoustics and heat release makes it possible for spontaneous combustion instability to be examined directly. This is done in CHAPTER 6. Validation with the experimental data is conducted at each step.

### 3.1. Cold Flow, Constant Area Duct Trials

Subsonic flow in a constant area duct without combustion is first employed to verify the one-dimensional code and to analyze the effects of parameters such as Mach number on the chamber acoustics. The length of the duct is 25 inches and the radius is 0.9 inches. This corresponds to the dimensions of the chamber region in the full computational model. The constant area duct geometry is shown in Figure 3.1.

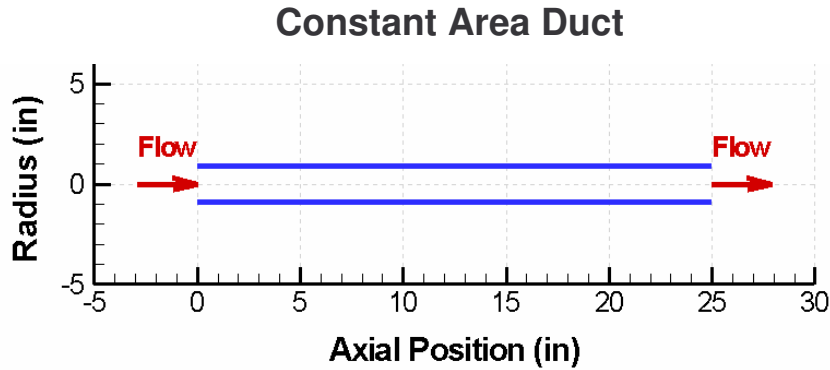


Figure 3.1: 25 inch straight duct configuration

Most of the flow properties and conditions in the duct are the same as the constant conditions in the chamber region of the full computational model, as shown in Table 2-3. The only exception is the mass-flow rate, which has been set as a parameter in order to vary the Mach number.

### 3.1.1. Low Mach Number Verification

The mass flow-rate is first set to obtain a low Mach number flow ( $M = 0.01$ ). This will most closely approximate a classical acoustic analysis in which there is no mean flow, as discussed in Section 1.1.3. The longitudinal acoustic modes can be obtained from the following equation, repeated for convenience:

$$F_{\text{modes}} = \frac{nc}{2L_c} \quad \text{Eq. 3.1}$$

where  $c$  is the speed of sound,  $L_c$  is the length of the chamber (25 inches in this case) and  $n$  is an integer which is dependent on the boundary conditions.

For a closed/closed system,  $n = 1, 2, 3, 4$ , etc. For a closed/open system,  $n = 1/2, 3/2, 5/2, 7/2$ , etc.<sup>13</sup> For the closed/open system represented by the straight duct configuration,  $L_c = 0.635$  m (25 in) and  $c = 1066.8$  m/s. The first four acoustic modes are calculated as 420 Hz, 1260 Hz, 2100 Hz, and 2940 Hz.

To verify the code, linear broadband forcing is performed with the standard frequency interval of 50 Hz. An FFT is taken to obtain the frequency content of the broadband forcing at various locations along the duct. This FFT plot is shown in Figure 3.2 for positions one, two, and three. Position one corresponds to the head-end of the duct, position two is at about 4 inches, and position three is halfway down the duct (12.5 inches).

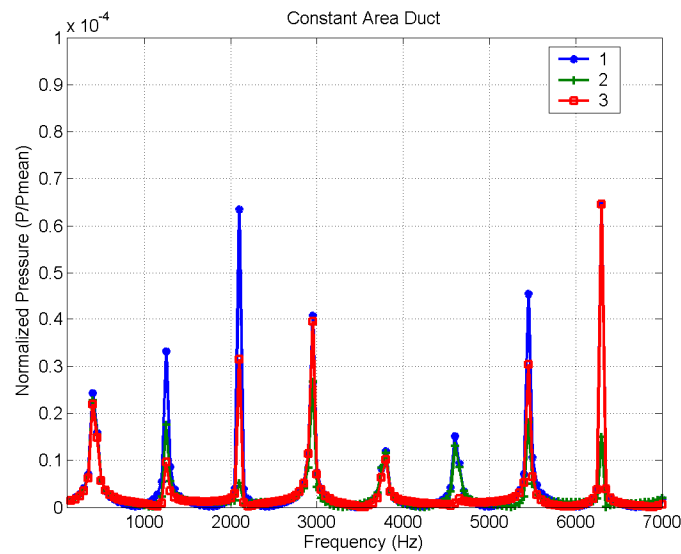


Figure 3.2: FFT plot taken at various locations of the duct for small amplitude broadband forcing for a chamber length of 25 inches and a Mach number of 0.01

The peaks of Figure 3.2 are very well defined (relatively narrow) and occur at identical frequencies for all of the axial locations in the duct. The response at position one (the head-end of the duct) is always higher than or equal to the responses at the other two positions. This can be understood more fully once the mode shapes are plotted (see Figure 3.4). The response at position one is repeated below in the left plot. The right plot shows a close-up view of the first peak in order to illustrate the 50 Hz frequency resolution. Note that frequencies can only be excited at intervals of 50 Hz.

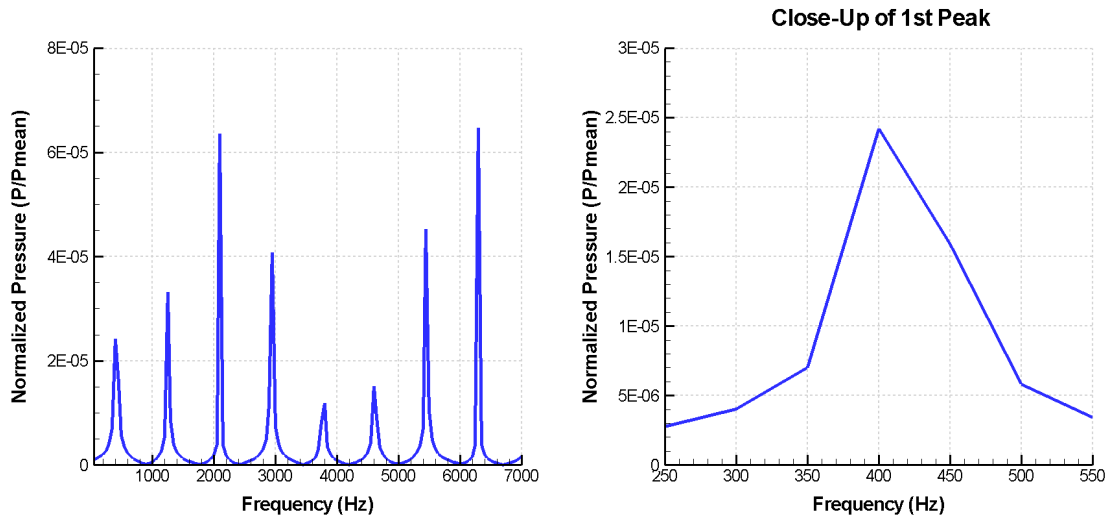


Figure 3.3: FFT plot of small amplitude broadband forcing taken at the head end of the duct for a chamber length of 25 inches and a Mach number of 0.01 (left). To illustrate the frequency resolution of the broadband plot, a close-up view of the 1<sup>st</sup> peak is shown in the right plot.

The first four peaks of Figure 3.3 occur at 400 Hz, 1250 Hz, 2100 Hz, and 2950 Hz. These frequencies correspond closely to the acoustic modes obtained by the classical acoustic analysis. All of the peak frequencies of Figure 3.3 match the classical acoustic modes within the specified frequency resolution. The amplitudes of the peaks depend on the axial location where the FFT was taken. In other words, the amplitudes vary continuously with the axial distance along the duct. To investigate the spatial variation of the oscillating pressure for each mode, a mode shape analysis was also performed. Mode shapes were obtained by forcing the flow at small amplitude at the selected mode frequency obtained from the broadband forcing. The pressure was output at every spatial location at 32 time intervals during the complete oscillation cycle. The mode shapes of the first four modes are plotted in Figure 3.4.

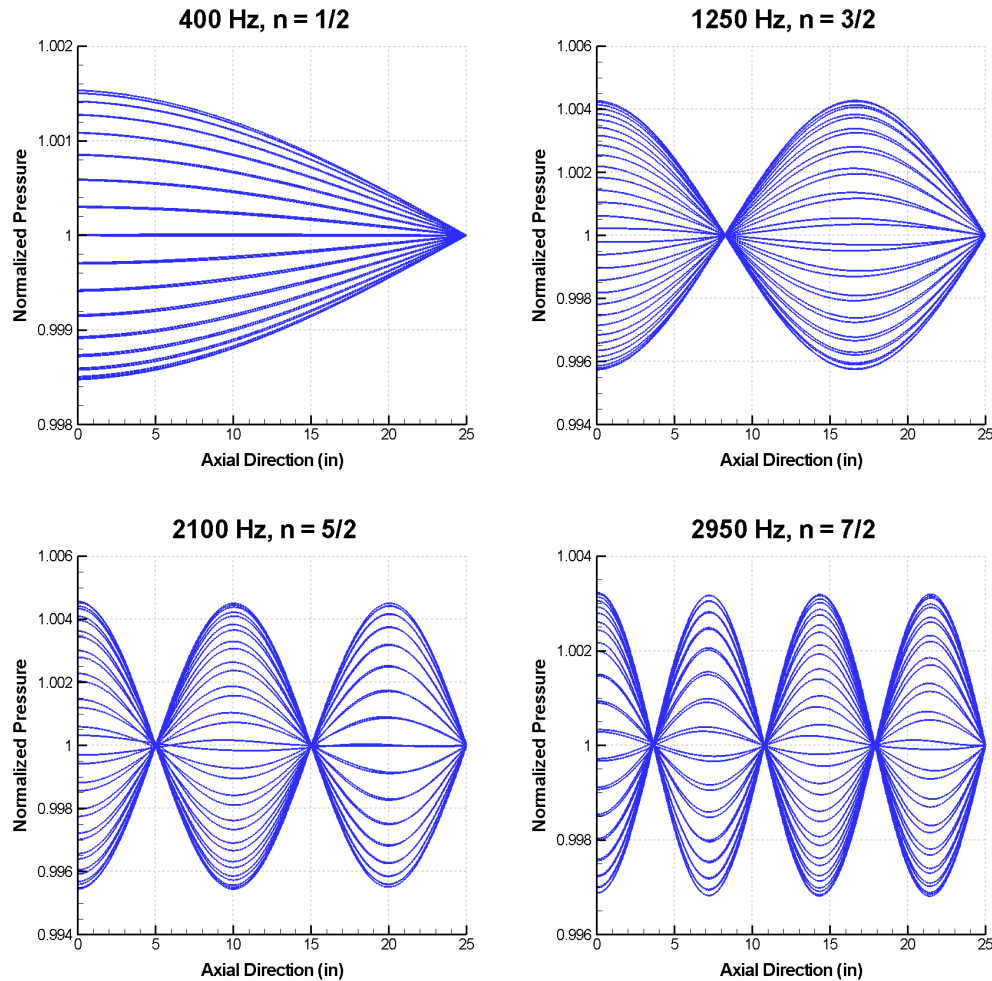


Figure 3.4: Mode shape plots for a closed/open constant area duct configuration with low Mach number ( $M = 0.01$ ) at 400 Hz, 1250 Hz, 2100 Hz, and 2950 Hz

The mode shapes in Figure 3.4 appear as expected for a closed/open system. Looking at the 400 Hz mode, a pressure anti-node is clearly seen on the left boundary, while on the right boundary there is a pressure node. An additional pressure node is added with each subsequent mode. Animation of the pressure oscillations for a particular mode show that these waves appear as standing waves, where the pressure anti-nodes (ie maximum or minimum) occur simultaneously across the length of the duct at the constant intermediate locations.



The phase relationship between the pressure and velocity can also be investigated by comparing the modes shapes of pressure and velocity. These are shown in Figure 3.5 for the 1250 Hz mode.

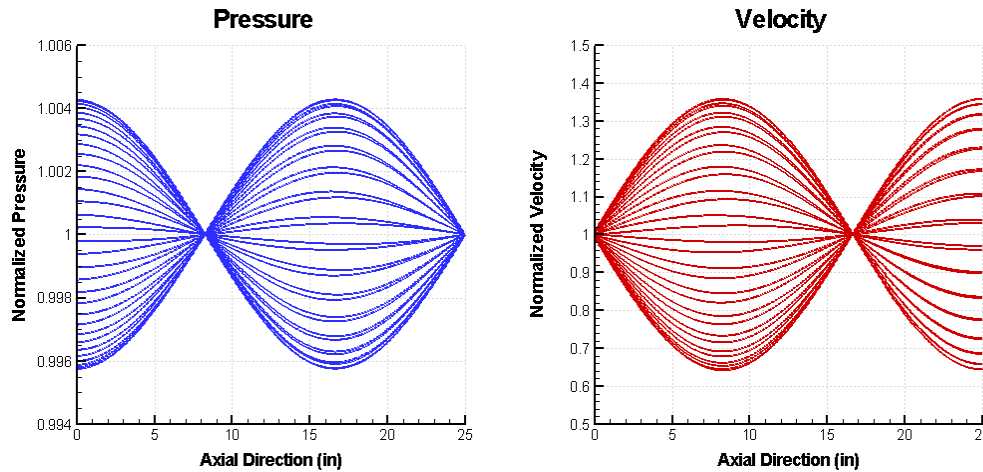


Figure 3.5: Pressure (blue) and velocity (red) mode shapes at 1250 Hz (plots are at different amplitude scales)

These plots show that where there is a pressure anti-node, a velocity node exists (far left boundary and at about 17 inches). At a velocity anti-node, a pressure node exists (at about 8 inches and the far right boundary). This suggests that pressure and velocity are 90 degrees (or 270 degrees) out of phase. This can be investigated further by comparing the actual pressure and velocity time traces at particular locations. The normalized pressure and velocity traces at the head end of the duct are shown in Figure 3.6.

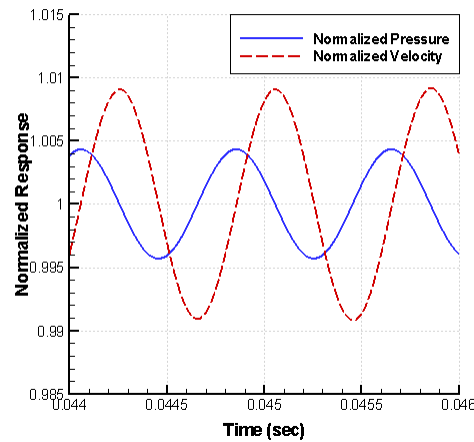


Figure 3.6: Pressure and velocity time traces at the injector head-end position

This shows that the velocity lags the pressure by 90 degrees. Wherever the normalized pressure is equal to one, the normalized velocity has a maximum or a minimum. Wherever the normalized velocity is equal to one, the normalized pressure has a maximum or minimum. This is consistent with the previous mode shape plots.

These results demonstrate that for low Mach number flow with a simple geometric configuration, the code yields identical modes as the classical acoustic analysis (within the frequency resolution). The mode shapes appear as expected, with pressure and velocity being 90 (or 270) degrees out of phase, depending on the spatial location in the duct.

### 3.1.2. Effects of Mean Flow on Acoustic Modes

The mass flow-rate in the duct is now increased so that the Mach number is relatively high ( $M = 0.38$ ), while the other conditions remain the same. This matches the experimental Mach number in the injector region. Broadband small amplitude forcing was performed and the FFT plots at positions one, two, and three are shown in Figure 3.8. These are the same positions used in Figure 3.2.

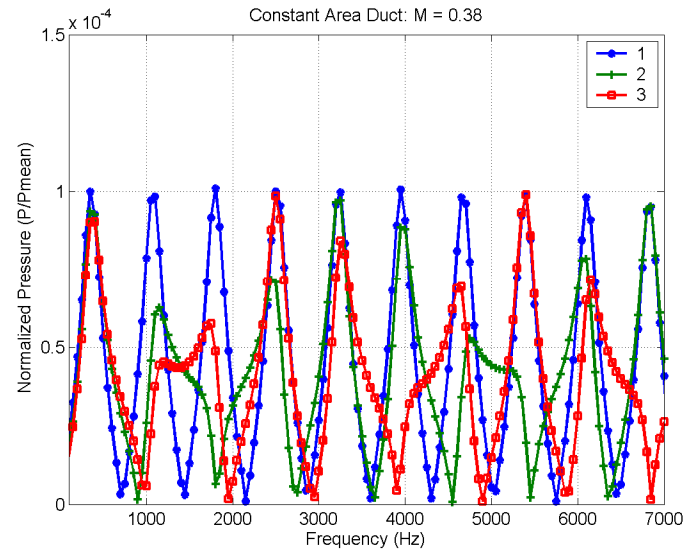


Figure 3.7: FFT plot of a small amplitude broadband forced, 25 inch straight duct with a Mach number of 0.38, taken at various positions in the duct

The peaks of Figure 3.7 are much wider and less well defined than in the low Mach number case. Also, the peaks occur at somewhat different frequencies for different axial positions (within 100 Hz of each other). The strongest response still occurs at position one (the head-end of the duct), however the other two positions do not even show peaks for some of the modes. This can be seen for position two at the 1800 Hz mode and for position three at the 3950 Hz mode. This mode variation at different axial positions is difficult to verify analytically, since classical acoustic analysis neglects mean flow.

Because the most well defined modes occur at the duct head-end, this response is compared with the low Mach number result at the same position. The low and high Mach number broadband results are plotted together in Figure 3.8. The FFT plot for the high Mach number case ( $M = 0.38$ ) is shown with a dashed blue line and the low Mach number case ( $M = 0.01$ ) is shown with a solid red line.

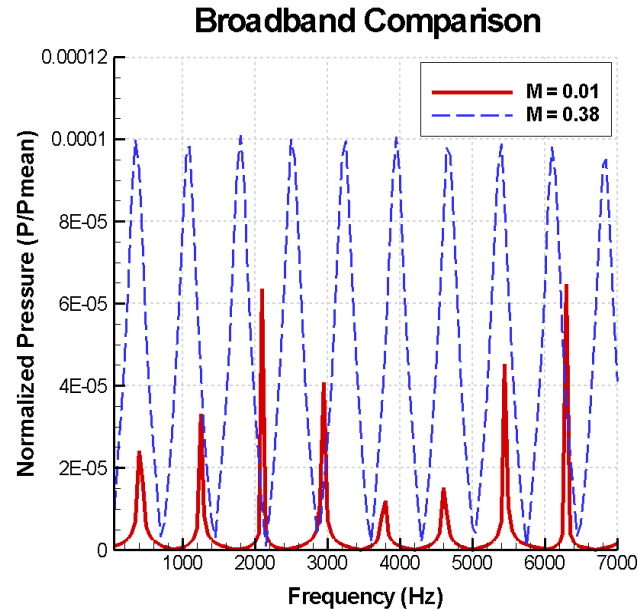


Figure 3.8: FFT plot of a small amplitude broadband forced, 25 inch constant area duct with Mach numbers of 0.38 (dashed blue) and 0.01 (solid red), taken at the head end of the duct

The first pressure peak for the higher Mach number case occurs at 350 Hz instead of 400 Hz. This suggests that increasing the Mach also number shifts the mode to a lower frequency. This is supported by other studies, where the mode frequencies were shown to decrease once the Mach number became significantly high.<sup>23</sup> The initially lower mode (350 Hz) causes the frequency interval between peaks to decrease from the low Mach number case. The interval between peaks changes from a range of 800-850 Hz in the low Mach number case to 700-750 Hz for the high Mach number case.

The analytical modes (with no mean flow) and computational modes ( $M = 0.01$  and  $M = 0.38$ ) are compared in Table 3-1. While the analytical and computational low Mach number modes match up well (within the 50 Hz frequency resolution), there is a significant difference between the low and higher Mach number modes. These differences suggest that mean flow effects have a significant impact on the acoustic modes of the system.

Table 3-1 Analytical and computational modes for the constant area configuration

n	Analytical (M = 0)	Computational	
		M = 0.01	M = 0.38
1/2	420	400	350
3/2	1260	1250	1100
5/2	2100	2100	1800
7/2	2940	2950	2500

The effects of higher Mach number on the mode shapes of the system were also investigated. The system was forced at the higher Mach number modes. The pressure at these modes was output at each spatial location for 32 time intervals within the oscillation cycle. The mode shapes of the first two modes are compared for the low Mach number case (on the left) and the higher Mach number case (on the right) in Figure 3.10 and Figure 3.10.

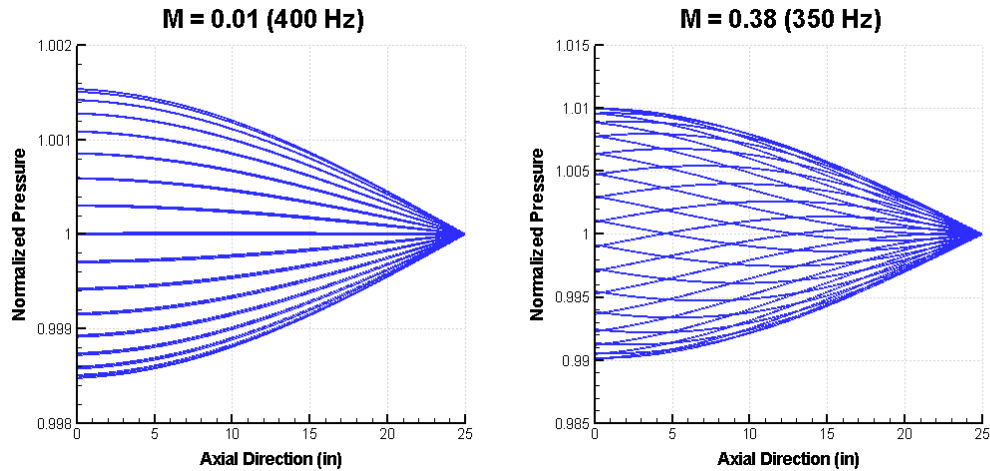


Figure 3.9 Mode shape comparisons for the first mode of a low Mach number flow (left) and a higher Mach number flow (right)

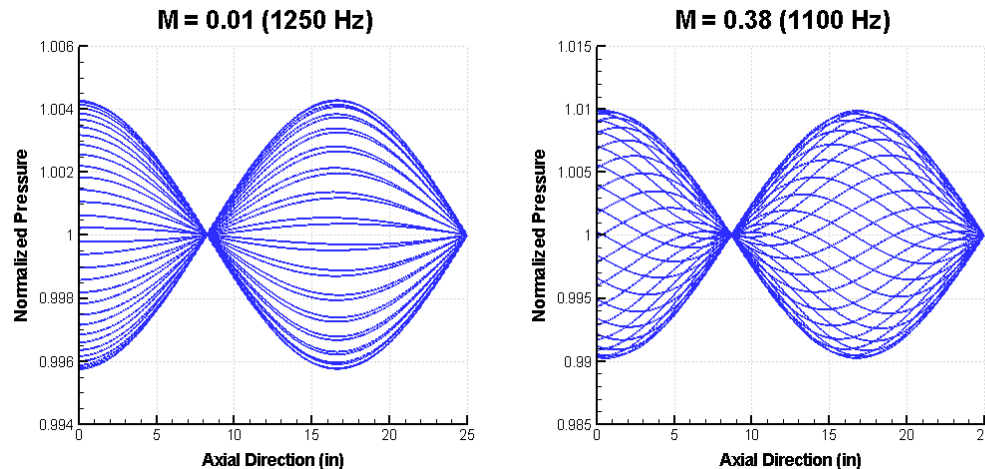


Figure 3.10: Mode shape comparisons for first and second mode of a low Mach number flow (left) and a higher Mach number flow (right)

The above plots show that increasing the Mach number changes the amplitude of the mode shape envelope, but has no effect on the envelope shape. However, the phase of the wave is very different between the low and high Mach number cases. Animation of the waves with respect to time shows that the high Mach number case combines a standing wave with wave propagation. The location of nodes and anti-nodes has not changed, but the wave appears to propagate across the duct. The pressure peaks no longer occur simultaneously along the length of the duct. This is due to the propagation of particle waves in the duct, which is discussed in more detail in CHAPTER 5. The particle wave was insignificant when the Mach number of the flow was low. When the Mach number is large, the particle wave propagation has an impact on the phase of the pressure wave, which then affects the mode shapes in the duct.

The phase relationship between the pressure and velocity is compared in Figure 3.11 for both low and high Mach number cases. Single frequency, small amplitude forcing at the second mode was employed. The time traces were taken at the head end of the duct.

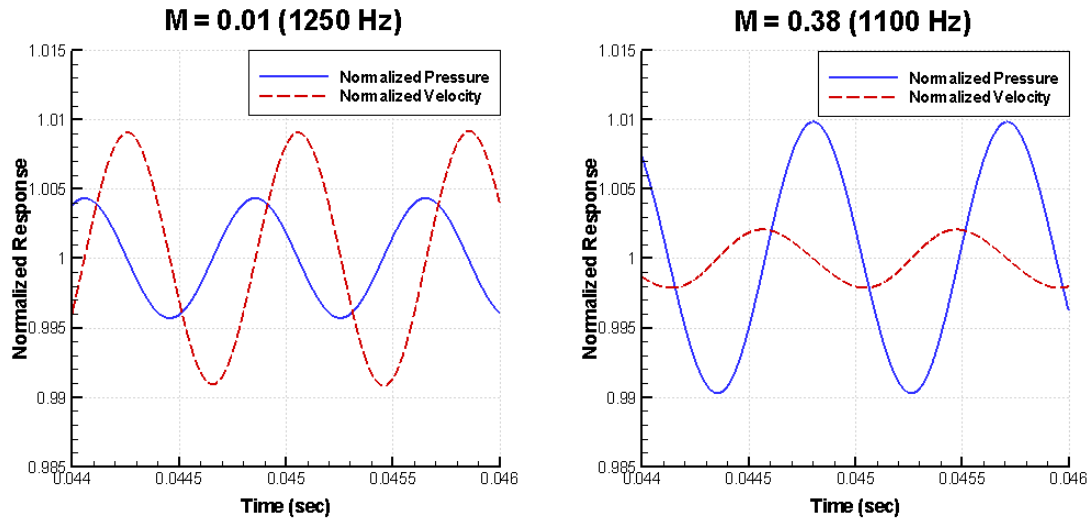


Figure 3.11: Pressure and velocity time traces for the second mode at the injector head-end for both the low and high Mach number cases

The above plots show that the velocity has changed from lagging the pressure by 90 degrees to lagging by 270 degrees (which is the same as stating that the velocity now leads the pressure by 90 degrees). The mean velocity in the duct is much higher for the high Mach number case, although the magnitude of mass flow forcing has remained the same. This causes the normalized velocity (oscillating velocity/mean velocity) to decrease in comparison with the normalized velocity of the low Mach number case. This accounts for the switch in the normalized velocity being greater for the low Mach number case and the normalized pressure being greater for the high Mach number case. Note that the relative amplitude between the pressure and velocity is a function of the location in the duct, the magnitude of mass-flow forcing, and the mean properties in the duct.

It is also of interest to investigate the spatial dependence of the pressure/velocity phase relationship. So far only the injector head-end has been analyzed, but this can be extended to any number of points in the duct. Five locations are chosen along the duct, corresponding to locations between nodes and anti-nodes for the second mode. The mode shape for the second mode is

shown in Figure 3.12 with the locations of output specified as positions one through five.

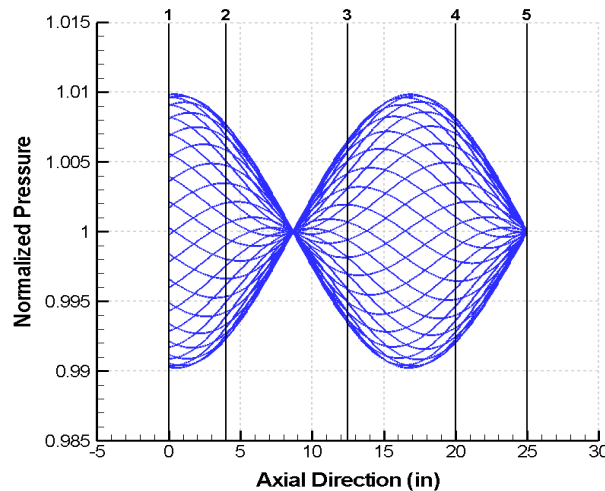


Figure 3.12: Output locations for pressure and velocity for the second mode (1100 Hz) for the high Mach number case

The pressure/velocity traces corresponding to positions one through four are shown in Figure 3.13. Small amplitude forcing at 1100 Hz and a Mach number of 0.38 have been employed. The phase relationship between the pressure and velocity changes between each position. At position one, the velocity leads by 90 degrees. At position two, the velocity lags by 90 degrees. At position three, the velocity again leads by 90 degrees. At position four, the velocity lags by 90 degrees. It appears that the phase changes by 180 degrees every time that a node or anti-node is crossed.



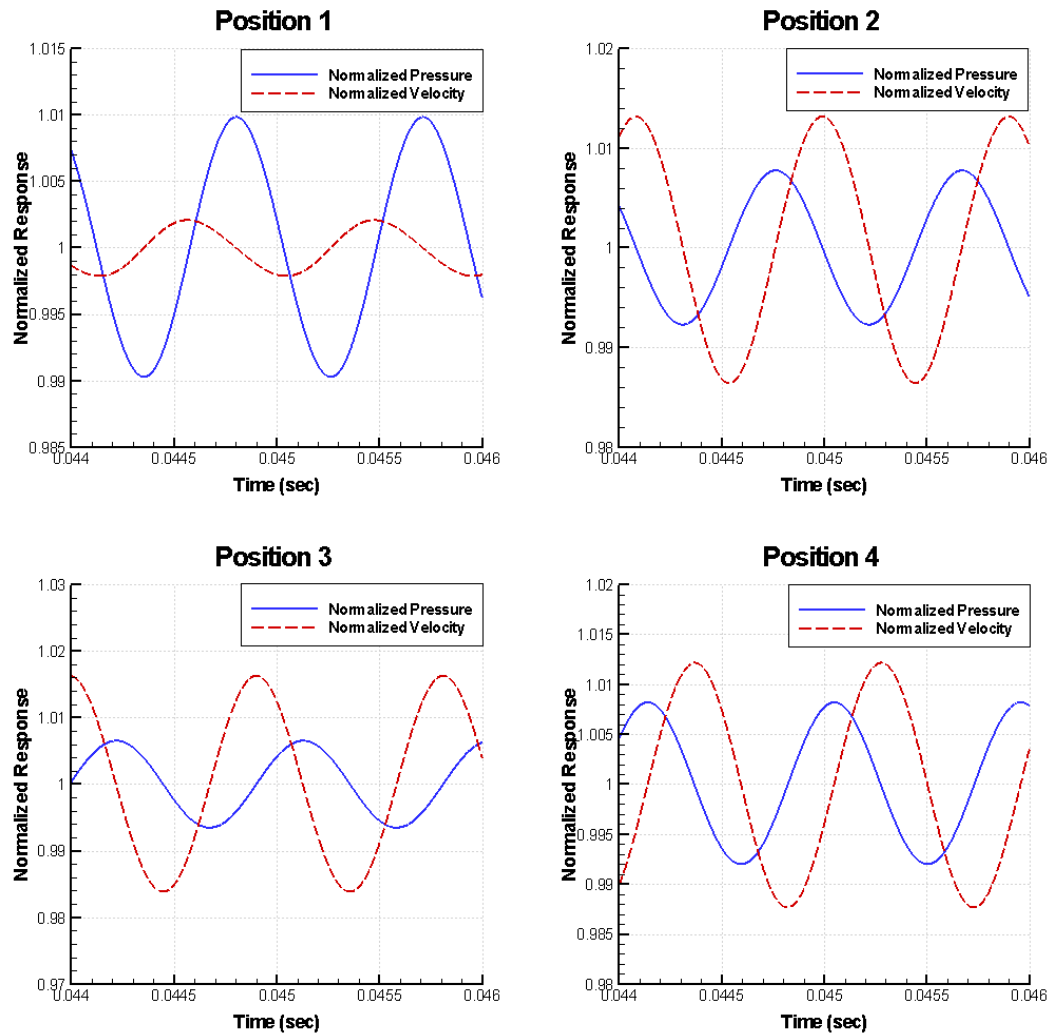


Figure 3.13: Pressure and velocity time traces at positions 1-4 (refer to figure 3.9) with small amplitude forcing at the second mode (1100 Hz)

Knowing the specific phase relationship between pressure and velocity is useful when developing response functions for particular combustion mechanisms. As explained in CHAPTER 1, understanding phase relationships is vital for determining whether the heat release is in phase with the pressure oscillations. Understanding the velocity phase is important in determining how certain mechanisms occur, such as vortex shedding.

### 3.2. Low Mach number, Simplified Computational Model

Cold flow, constant area duct trials were performed in the previous section in order to verify the code and to gain a general understanding of acoustic behavior, for both low and high Mach number flows. The analysis is now expanded to include injector and chamber regions and a combustion source. This configuration differs from the full computational model in that the Mach number has been decreased and the nozzle geometry has been replaced with a  $u' = 0$  boundary condition (see Section 5.2.1). This will be referred to as the 'simplified' computational model. The geometry for this model is shown in Figure 3.14.

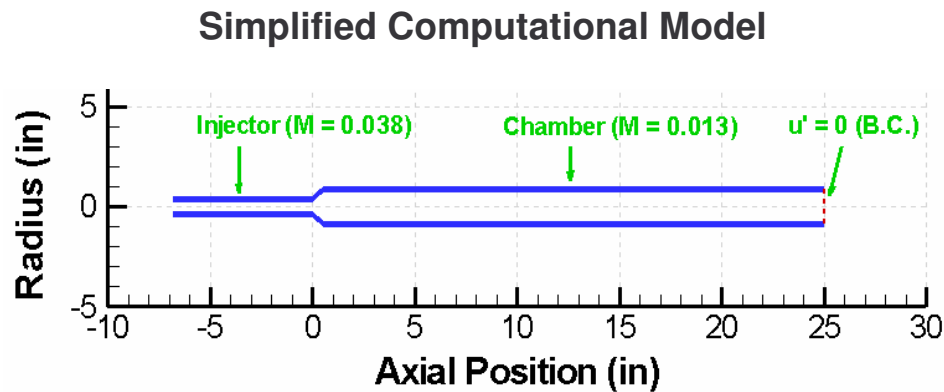


Figure 3.14: Simplified computational model with an outflow  $u' = 0$  boundary condition and decreased Mach number flow

These simplifications have been employed so that comparisons can be made with an analytical model (see Section 3.2.2). The analytical model uses similar geometry as the simplified computational model, including an injector region, a chamber region, and a downstream  $u' = 0$  boundary condition. Instead of a combustion source term, one set of constant conditions are applied in the injector region and another set in the chamber region. Mean flow is not accounted for and the upstream boundary simulates a hard wall. Full development of the analytical model can be found in Sisco<sup>14</sup>.

### 3.2.1. Results of the Simplified Computational Model

The mass flow-rate in both the injector and chamber regions has been decreased to  $1/10^{\text{th}}$  of the full computational model values in order to decrease the Mach number of the flow. This gives Mach numbers of 0.038 in the injector and about 0.013 in the chamber. When the Mach number is decreased to this low level, mean flow effects are assumed to have a negligible impact on the system acoustics. In order to change the mass flow-rate while maintaining the same geometry, the nozzle grid points have been replaced by a  $u' = 0$  boundary condition. This is shown to be accurate as long as the perturbations are small (see Section 5.2.1).

Broadband small amplitude forcing is applied to determine the frequency content of the system. A chamber length of 25 inches has been used to obtain the FFT plot in Figure 3.15.

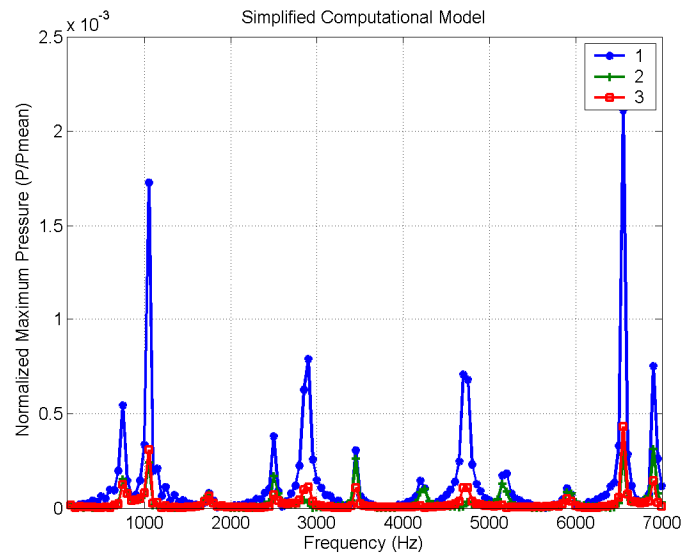


Figure 3.15: FFT plot of the simplified computational model forced with broadband small amplitude forcing. The chamber length is 25 inches.

The modes in Figure 3.15 appear to be fairly narrow and well defined. The first four modes, as indicated by all of the axial positions, are 750 Hz, 1050 Hz,

1750 Hz, and 2500 Hz. Almost all of the axial positions show the same mode frequencies. This suggests that mean flow effects are the main cause of the frequency variation with axial position that was observed in the previous section. Geometric effects may have an impact on this variation, but it appears to be slight.

The interpretation of the modes shapes of the system becomes more complicated when the geometry of the injector and chamber are included. Now the acoustic mode may be due to a mode in the chamber, a mode in the injector, or a mode which is a combination of modes in the injector and chamber. To assist in the interpretation of the modes shown in Figure 3.15, the mode shapes were plotted for the first four modes. Because of the geometry and boundary conditions, it is expected that the injector region will resonate similar to a closed/open system while the chamber will resonate similar to a closed/closed system. The chamber region acts more like a closed/closed system than an open/open system because of the steep area changes at the injector/chamber interface and the nozzle. While the injector and throat do provide open area, sloped wall boundaries encompass the majority of the chamber boundary area.

The mode shapes for the first four frequency peaks are shown in Figure 3.16, corresponding to frequencies of 750 Hz, 1050 Hz, 1750 Hz, and 2500 Hz. The left boundary (axial position = -6.82 inches) corresponds to the injector head-end or the inflow boundary. The right boundary (axial position = 25 inches) corresponds to the end of the chamber or the outflow boundary. The axial position of zero corresponds to the injector/chamber interface. Each mode shape is plotted at a different scale in order to see the details of the oscillations.

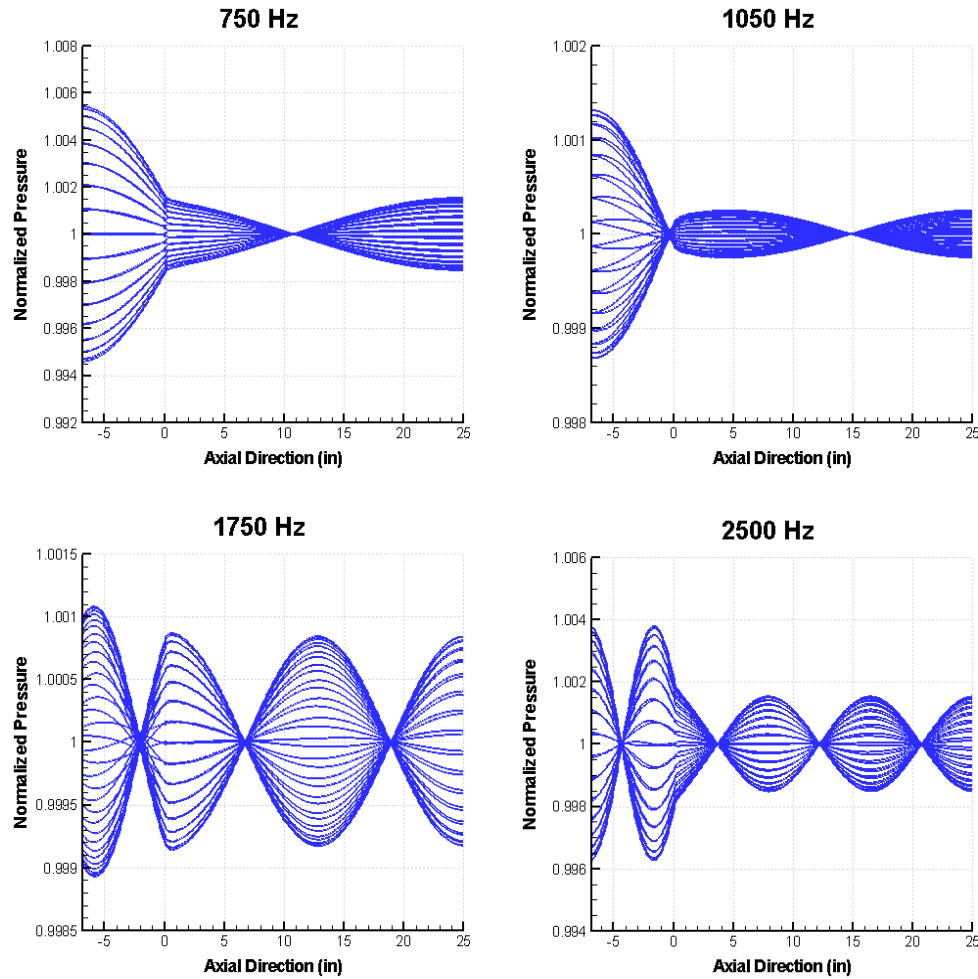


Figure 3.16: First four mode shapes of the simplified computational model for single frequency small amplitude forcing and a 25 inch chamber length

The 750 Hz mode shape appears to correspond to the first mode in the chamber. The 1050 Hz mode shape appears to represent the first half mode in the injector. The 1750 Hz mode shape corresponds to the second chamber mode. The 2500 Hz mode shape appears to be very close to both the third chamber mode and the 3/2 injector mode. The higher frequency modes also show behavior characteristic of injector half modes, chamber modes, or coupled modes.

The 1750 Hz mode shape in Figure 3.16 appears very much like a coupled closed/closed third chamber mode. It is interesting to note that this is

close to the frequency at which the experiment went unstable for the 25 inch chamber tests. As described in Section 1.3, the experiment was designed so that the injector and chamber modes would couple, thus promoting instability. Since the amplitudes of the injector and chamber modes are very close in magnitude at this frequency, there may be participation between the modes in exciting combustion instability. This is discussed further in Miller<sup>10</sup>.

The pressure and velocity mode shapes can also be compared, as was done in the constant area duct analysis. The pressure mode shape is shown on the left and the velocity mode shape on the right for the 1750 Hz mode.

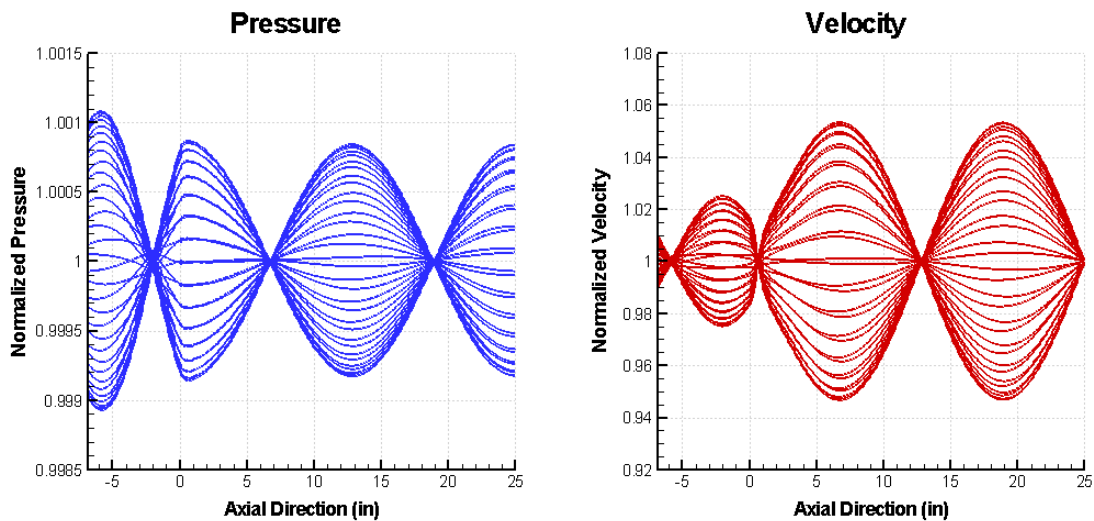


Figure 3.17: Pressure and velocity mode shape comparison for the 1750 Hz mode

These results appear similar to the straight duct case, in that the pressure and velocity mode shapes appear to be 90 (or 270) degrees out-of-phase. This is apparent because everywhere there is a pressure node, there is a velocity anti-node. Everywhere there is a velocity node, there is a pressure anti-node. The geometry difference between the straight duct configuration and the simplified computational model appears to have no influence on the phase relationship.

### 3.2.2. Comparison with an Analytical Model

The results from the previous section are now compared to an analytic solution containing similar conditions and geometry as the experiment.<sup>14</sup> The model uses average properties in the injector and chamber regions and causes the pressure oscillations to be equal at the injector/chamber interface by using mass and momentum balances. The model does not account for mean flow and uses  $u' = 0$  boundary conditions at the upstream and downstream ends. Although the analytical model has obtained modes for all of the experimental chamber lengths (see Sisco<sup>14</sup>), only the 25 inch case is used for comparisons. Table 3-2 shows the modes from the analytical model (labeled Analytical), the modes from the simplified computational model (labeled Computational) and the relative difference between the two frequencies.

Table 3-2: Comparison between the analytical and simplified computational models for a 25 inch chamber length

Mode	Analytical	Computational	% Difference
1st chamber	763	750	1.70%
	1055	1050	0.47%
2nd chamber	1718	1750	1.86%
	2521	2500	0.83%
3rd chamber	2946	2850	3.26%
	3447	3450	0.09%
4th chamber	4254	4250	0.09%
	4848	4750	2.02%
5th chamber	5190	5150	0.77%
	5980	5900	1.34%
6th chamber	6710	6550	2.38%
	6978	6900	1.12%

The mode designation in the left-hand column specifies what chamber mode is most closely approximated by the mode shape. The percent difference between the models is less than 4% in all cases, and less than 2% in most cases (all but two). Considering the approximations that were made in the analytical model in relation to the computational model (the mean flow is not zero and the combustion source creates changing properties in the chamber), the results appear to match very well.

Further understanding can be obtained by comparing the mode shapes directly. The mode shapes corresponding to the first two frequency peaks (750 Hz and 1050 Hz) are shown in Figure 3.18 and Figure 3.19 for both the analytical model (left) and the computational model (right). Note that different scales are used to generate the mode shapes.

The mode shapes show very good agreement between the analytical and simplified computational models for both the 750 Hz and the 1050 Hz modes. There appears to be a slight difference in the injector/chamber relative amplitudes for the 750 Hz mode shape. For the 1050 Hz mode shape, the phase in the injector region is slightly different, although the envelopes appear almost identical. Animation of the mode shapes shows that both approximate standing waves very closely.

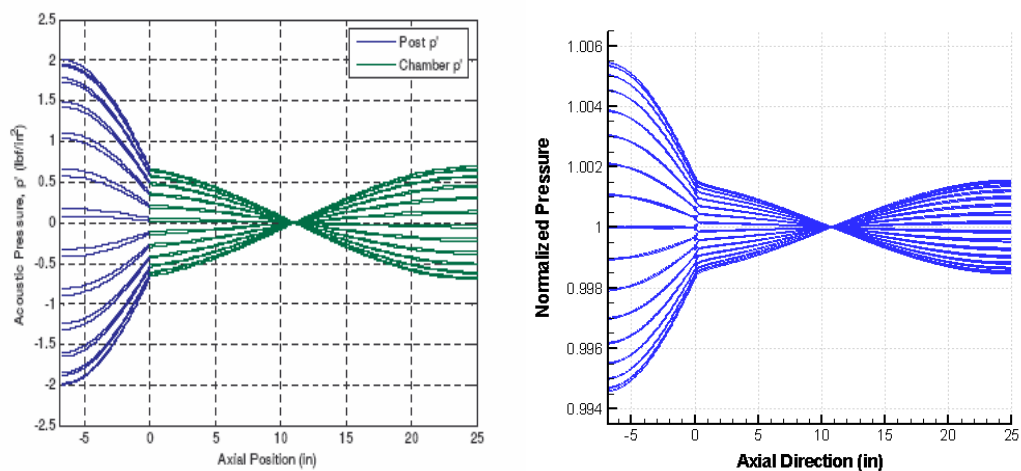


Figure 3.18: Pressure mode shapes using the analytical model (763 Hz, left) and the low Mach number, simplified computational model (750 Hz, right)



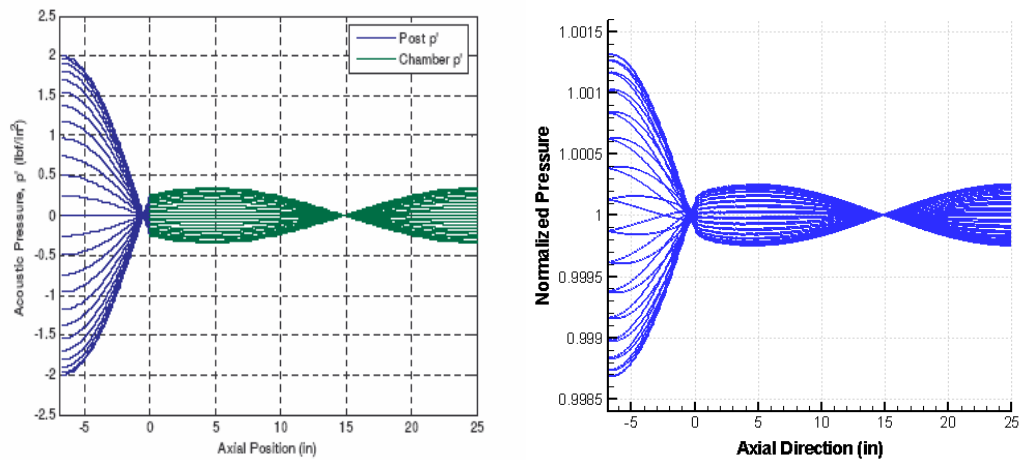


Figure 3.19: Pressure mode shapes using the analytical model (1055 Hz, left) and the low Mach number, simplified computational model (1050 Hz, right)

Because the 2<sup>nd</sup> chamber mode shape represents an important frequency (the frequency at which the experiment goes unstable), both pressure and velocity mode shapes are compared for this frequency. Figure 3.20 shows the analytical pressure mode shape on the left and the computational pressure mode shape on the right.

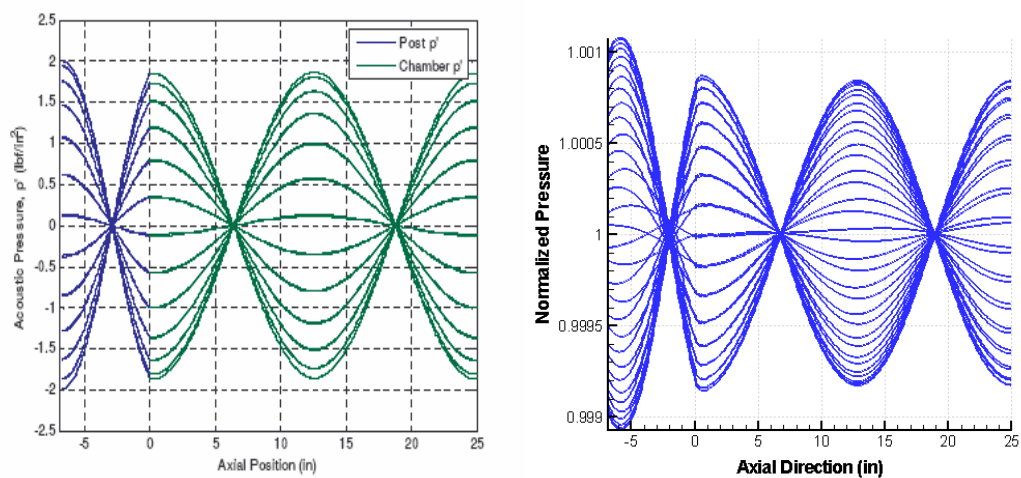


Figure 3.20: Pressure mode shape comparison between the analytical model (at 1718 Hz, left) and the low Mach number, simplified computational model (1750 Hz, right).

There is a slight difference between the analytical and computational results in the relative magnitudes between the chamber and injector. There is also a slight difference at the injector head end. For the analytical result there is an exact pressure anti-node at the injector head-end, while for the computational result the mode shape is just past an anti-node. Overall there appears to be good agreement at this chamber length. The analytical (left) and computational (right) velocity mode shapes are shown in Figure 3.21.

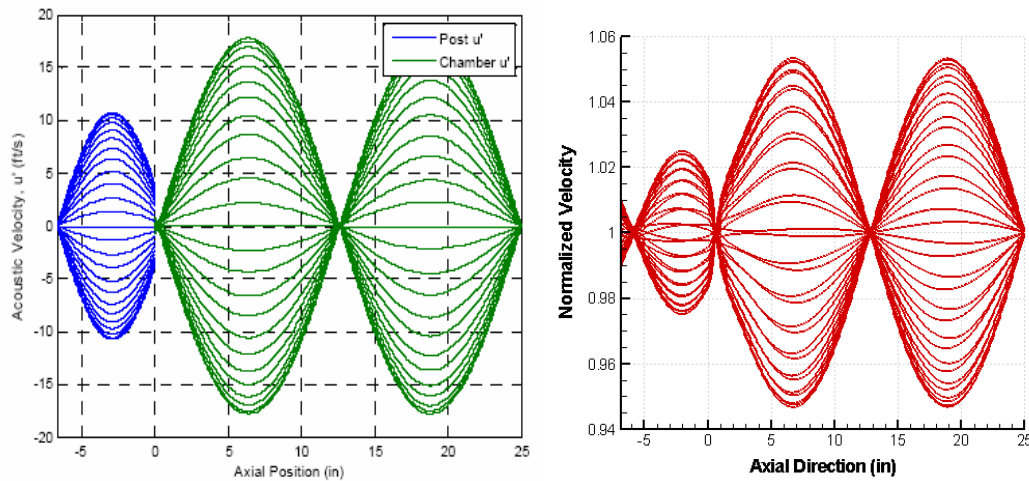


Figure 3.21: Velocity mode shape comparison between the analytical model (at 1718 Hz, left) and the low Mach number, simplified computational model (1750 Hz, right).

For the velocity mode shapes, the same trends appear as the pressure mode shapes. The relative injector/chamber amplitudes are slightly different between the two models. Also, the response at the injector head-end shows a slight variation. For the analytical mode shape there is a velocity node at the injector head-end. For the computational result the velocity mode shape is just past a node at the injector head-end.

Overall, the results from the analytical model and the simplified computational model match very well. A high Mach number analysis of the simplified computational model is not performed because it cannot be compared to the analytical model (since the analytical model does not account for mean

flow). Instead, results are obtained in the next section for the high Mach number, full geometrical computational model.

### 3.3. Full Computational Model Results

The full computational model, described in detail in CHAPTER 2, is now employed so that comparisons can be made with the experimental results in Section 3.4. This includes the full geometry (injector, chamber, and nozzle), a combustion source term, and a relatively high mach number in the injector region ( $M = 0.38$ ). The 25 inch chamber length case is chosen as the base case, which corresponds to test 25D1r (test 11) in the experiment.

The approach for validation is similar to the approach used in the previous sections for verification. Using broadband small amplitude mass flow forcing, an FFT plot is obtained which yields the acoustic modes of the system. Each of these modes is forced individually to obtain the mode shapes. Both the FFT plots and the mode shapes are compared to experimental data. This approach will be repeated in Section 3.3.4 for different chamber lengths, corresponding to the chamber lengths of the experimental tests.

#### 3.3.1. Results of the 25 inch Chamber Case

The broadband small amplitude forced FFT plot of the 25 inch chamber is shown in Figure 3.22 for positions one, two, three, and five (see Section 2.3). These correspond to the head-end of the injector, the injector/chamber interface, and two locations inside the chamber. The frequency resolution is 50 Hz.

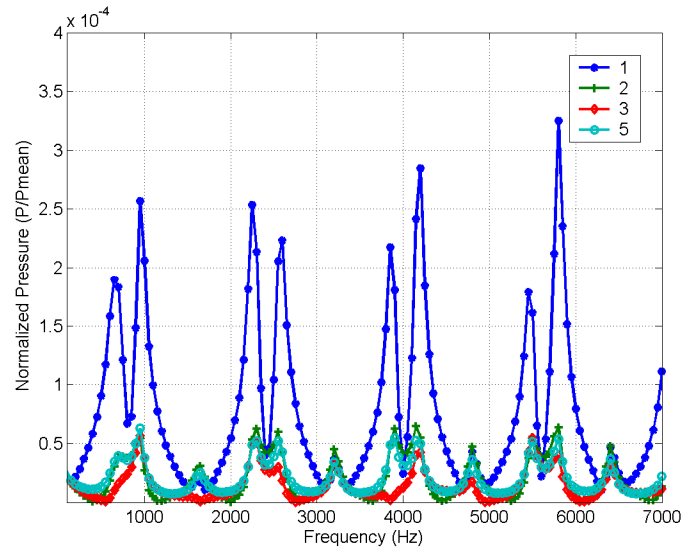


Figure 3.22: FFT plot of the 25 inch chamber case with small amplitude broadband forcing at positions 1, 2, 3, and 5

The pressure peaks are relatively wide and occur at somewhat different frequencies for each axial position, within 100 Hz of each other (see Appendix A for mode tables at all positions for all chamber lengths). This frequency variation is similar to the variation that was observed in Section 3.1.2. It appears that this variation in mode frequency is caused by mean flow effects. As the Mach number increases, the modes become wider and the pressure peaks occur within a range of frequencies for different axial positions. This range is within 100 Hz.

This frequency variation is investigated further by comparing the mode shape plots for the first mode, as indicated by position one (650 Hz) and position two (750 Hz). These plots are shown together with the same scale in Figure 3.23. Although the amplitudes at the injector head-end are somewhat different, the overall characteristics of the mode shapes appear similar. The mode in the injector is approaching the first  $\frac{1}{2}$  mode and the mode in the chamber is approaching the first mode in both plots. This suggests that there will not be dramatic differences within the range of mode frequencies excited by the different axial positions.

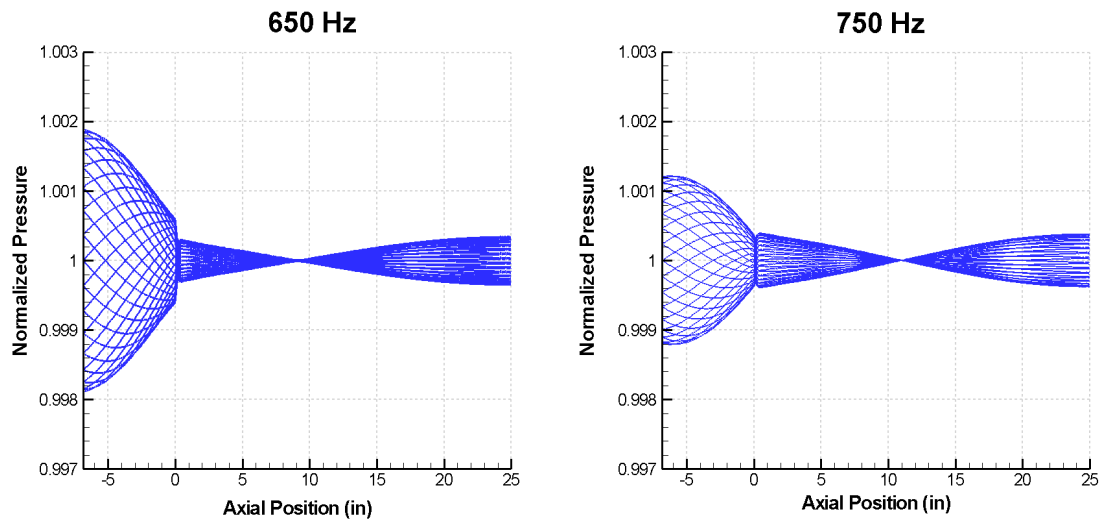


Figure 3.23: Mode shape comparison for the mode indicated by position 1 (650 Hz) and the mode indicated by position 2 (750 Hz)

For validation purposes (and for plotting of mode shapes), the exact modes are chosen as those which show the largest response in the FFT plot. For example, position one indicates a peak at 650 Hz while position two indicates a peak at 750 Hz. Since position one has the stronger response (higher amplitude), 650 Hz is chosen as the mode. This choice seems reasonable since in combustion instability, the heat release is most likely to couple with the frequency that shows the largest response. In Figure 3.22, either position one or position two always show the largest response. This is also the case in Section 3.3.4 when other chamber lengths are applied.

Although the frequencies at each position in Figure 3.22 are close to each other, the amplitudes at each position vary dramatically. The head-end of the injector (position 1, blue) shows a much higher amplitude response for certain modes. The injector/chamber interface (position 2, green) and the interior chamber positions (position 3, red and position 5, cyan) show roughly the same pressure amplitudes. This difference in amplitudes is due to the mode shapes at the various modes. For a particular mode, if the response is taken near a pressure anti-node the amplitude will be higher than if the response is taken near

a pressure node. In order to understand the spatial behavior of each mode, it is necessary to plot the mode shapes corresponding to the frequency peaks.

The first four peaks are located at frequencies of 650 Hz, 950 Hz, 1650 Hz, and 2250 Hz. These modes correspond to the injector half modes, the chamber modes, or some coupling of the two. The pressure mode shapes corresponding to these modes are plotted in Figure 3.24. Each has the same scale so that amplitudes can be compared. The axial position of zero is the interface between the injector and chamber.

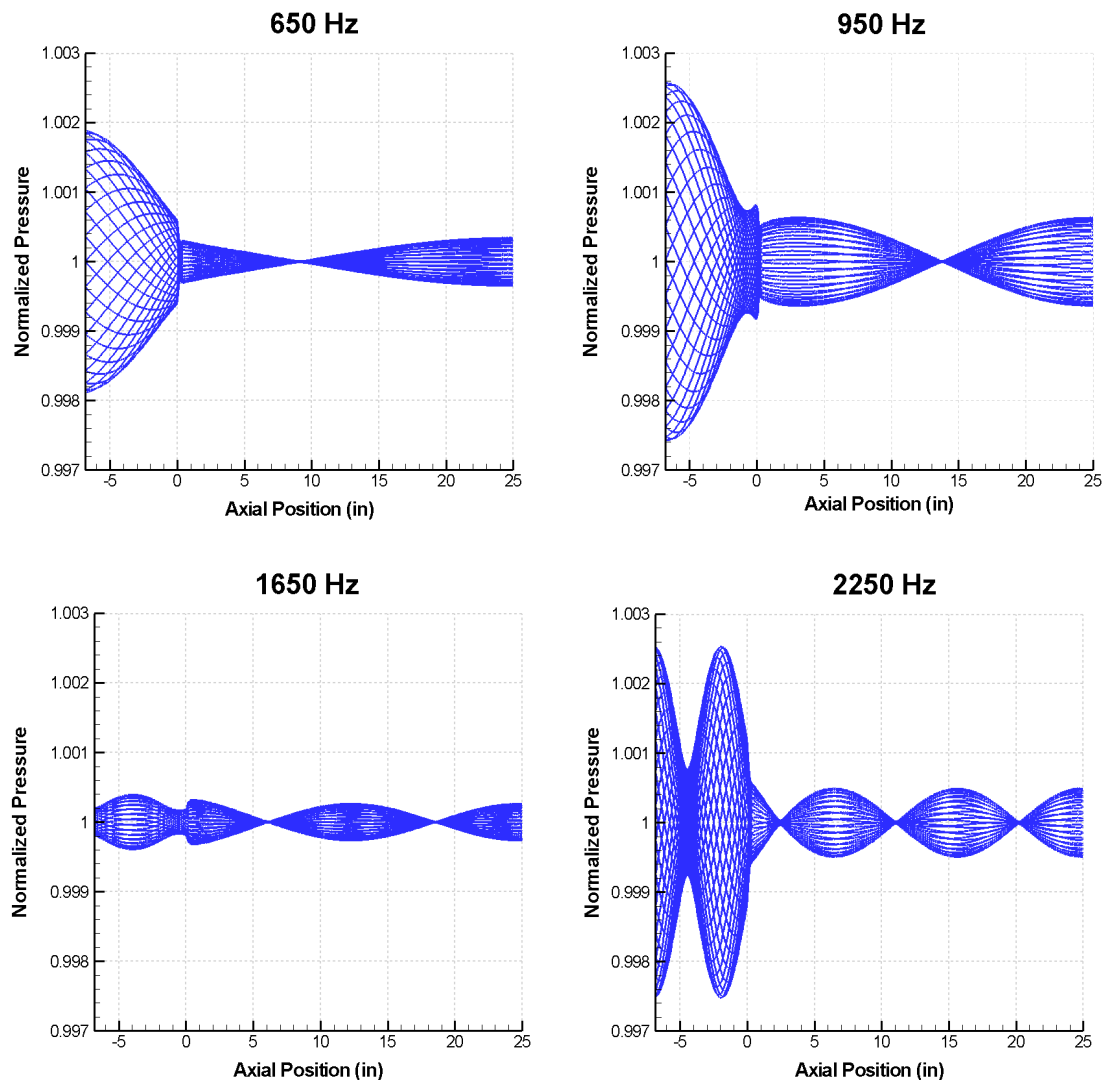


Figure 3.24: Mode shapes at 650 Hz, 950 Hz, 1650 Hz, and 2250 Hz for a 25 inch chamber

Note that the mode with the closest injector and chamber amplitudes is the 1650 Hz mode, which was the unstable mode in the experiments. The experiment was designed so that coupling would occur between the injector and chamber to promote instability. This coupling is believed to occur most easily when the injector and chamber amplitudes are close in magnitude. By comparing the relative amplitudes between the injector and chamber, the mode shapes may give an indication of which modes are most likely to go unstable.

These mode shapes appear similar to the mode shapes in Figure 3.16. The most notable difference between the low Mach number mode shapes and the full computational model mode shapes is the phase difference between the waves in the chamber and the waves in the injector region. From the constant area duct studies (see Figure 3.10), this can be attributed to the Mach number difference between the chamber and the injector. In the chamber, the Mach number is 0.13 while in the injector the Mach number is 0.38. The wave in the chamber appears like a standing wave while the wave in the injector appears like a combination of a standing wave and a traveling wave. This may cause the interface between the chamber and injector to be somewhat distorted, as can be seen in the 950 Hz mode shape. There also appears to be a widening of the nodes in the injector region. This is especially apparent in the 2250 Hz mode shape.

The velocity mode shapes can also be examined in comparison with the pressure mode shapes. The experimental 25 inch chamber tests went unstable near 1650 Hz, so this mode is chosen for more detailed analysis. The 1650 Hz mode shape is plotted in Figure 3.25, with the pressure mode shape in blue and the velocity mode shape in red.

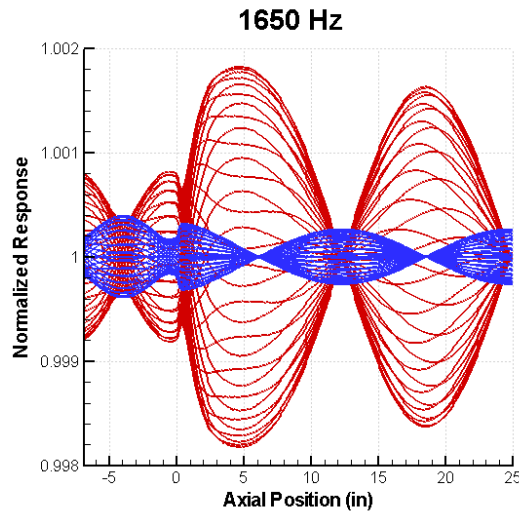


Figure 3.25: Pressure (blue) and velocity (red) mode shapes for a 25 inch chamber forced at 1650 Hz with small amplitude forcing

The velocity mode shape appears as expected, with approximate nodes where the pressure mode shape has anti-nodes, and anti-nodes where the pressure mode shape has nodes. Of interest is the relative size of the first velocity anti-node in the chamber compared to the second anti-node. This may be caused by the distortion that occurs in going from a relatively low Mach number in the chamber to a relatively high Mach number in the injector.

Comparison between the pressure mode shapes for the simplified and full computational models are shown in Figure 3.26 for the 2<sup>nd</sup> chamber mode. The mode shape for the simplified computational model (left) is the same as in Figure 3.16. The mode shape for the full computational model (right) has been scaled differently from Figure 3.24 so that more detail can be seen.



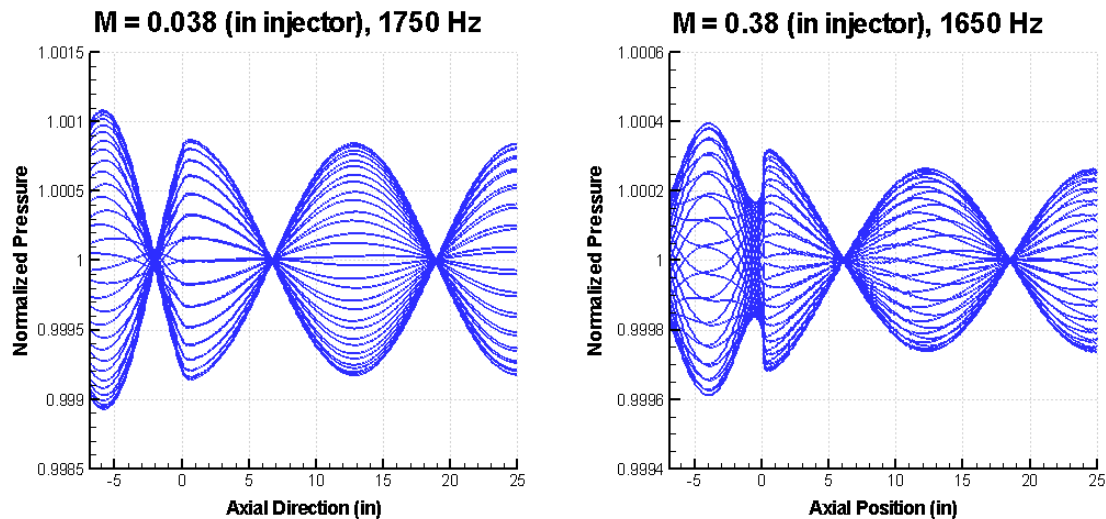


Figure 3.26: Mode shape comparison for the simplified computational model at 1750 Hz and the full computational model at 1650 Hz. The chamber length is 25 inches.

With a higher Mach number, the mode occurs at a lower frequency, changing from 1750 Hz in the simplified computational model to 1650 Hz in the full computational model. This is consistent with the findings in the constant area duct trials that as the Mach number increases, the mode frequencies decrease.

The relative amplitudes between the simplified computational model pressure peaks and the full computational model pressure peaks are very similar. However, the mode shape envelope in the injector is dramatically different. For the low Mach number case, the mode in the injector appears to almost approximate a closed/closed mode with a pressure node in the middle of the injector. For the full computational model mode shape, the mode in the injector appears to be approaching an open/open mode, with an anti-node in the middle of the injector.

For these conditions, the Mach number has not only changed the phase in the injector, but has also changed the fundamental shape of the mode. Part of the reason for this behavior is because the injector head-end boundary condition is not a wall boundary, but instead is an inflow boundary. Computations with the

injector head-end boundary condition changed to a wall boundary are dealt with in Section 5.3.1.

### 3.3.2. Variation of Frequency Resolution

The frequency resolution for the small amplitude broadband forcing has been specified as 50 Hz for all of the previous results. In other words, the broadband spectrum represented frequencies at 100 Hz, 150 Hz, 200 Hz, up to 7000 Hz. After this forcing was applied, frequency analysis was used to determine the acoustic modes excited by the system. For this thesis, either a fast Fourier transform (FFT) or power spectral density (PSD) analysis has been used. The frequency resolution controls how much data must be collected for an accurate analysis. The necessary number of data points is defined in Equation 3.2 as,

$$N_{\text{data\_pts}} = \frac{1}{\Delta f * \Delta t} \quad \text{Eq. 3.2}$$

where  $N_{\text{data\_pts}}$  equals the number of data points,  $\Delta f$  is the frequency resolution, and  $\Delta t$  is the computational time step.

For  $\Delta t = 0.45\text{e-}6$  seconds and  $\Delta f = 50$  Hz,  $N_{\text{data\_pts}} = 44445$  points (if rounded to the next highest integer). If the frequency resolution is doubled to 100 Hz, then 22223 points are necessary. If the frequency resolution is halved to 25 Hz, then 88889 points are necessary. Each of these resolutions was applied to the 25 inch chamber case and frequency analysis was performed to determine the modes. These results are summarized in Table 3-3.

Table 3-3: Acoustic modes for the 25 inch chamber case for frequency resolutions of 25, 50, and 100 Hz

Mode	Frequency Resolution		
	25 Hz	50 Hz	100 Hz
1st chamber	675	650	700
	950	950	1000
2nd chamber	1625	1650	1600
	2275	2250	2300
3rd chamber	2575	2600	2600
	3200	3200	3200
4th chamber	3875	3850	3900
	4175	4200	4200
5th chamber	4800	4800	4800
	5475	5450	5500
6th chamber	5800	5800	5800
	6400	6400	6400
7th chamber			
8th chamber			

All of the modes in Table 3-3 are within 50 Hz of one another, and in many cases the modes match exactly. When they don't match exactly, the 25 Hz modes are usually in-between the 50 and 100 Hz resolutions. As shown in Equation 3.2, more precise frequency resolutions require more data points, which is computationally more expensive. A frequency resolution should be chosen with consideration to both its accuracy and its cost.

For the experiments, there was some variability in the tests that were run. For example, under the same conditions, the unstable frequency for the 25 inch case ranged from 1709 Hz to 1660 Hz (see Table 1-1). Due to this variability, the 50 Hz frequency resolution was chosen for broadband forcing. It is only half as expensive as the 25 Hz resolution and appears to closely match the variability in the data. This frequency resolution is applied for the rest of the broadband forced cases. If a higher precision is desired for a particular case, this resolution can be easily changed and the case can be run again.

### 3.3.3. Decay Studies

Along with the other analysis which has already been done for the 25 inch chamber length, the decay of the small amplitude forced signal is also analyzed. This is done by forcing the mass flow at 1650 Hz and 0.001% of the mean mass flow-rate until a converged condition is reached where the oscillation maximum and minimum remain constant. The mass flow forcing is then set to zero and the pressure response is observed. The pressure history at position two is shown in Figure 3.27 for these conditions. The point at which the mass flow forcing was turned off is labeled.

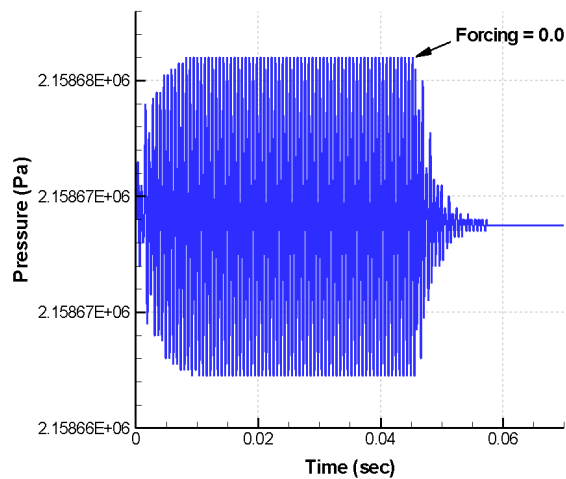


Figure 3.27: Growth and decay of pressure for forcing at 0.001% and 1650 Hz for a 25 inch chamber

In order to analyze only the pressure oscillation ( $p'$ ), the mean pressure was subtracted off. A close-up view of the decay region (0.045 sec – 0.061 sec) is shown in Figure 3.28.

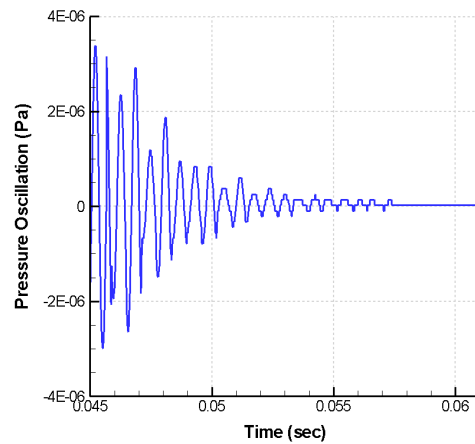


Figure 3.28: Decay of the pressure oscillation for forcing at 0.001% and 1650 Hz

A more quantitative analysis of the above decay can be done by curve fitting the maximum pressure at each oscillation. By doing this, an exponential decay curve was obtained and is shown below. The exponential equation that defines this curve is  $y = \exp(-328.8 \cdot x + 2.287)$ . The curve has an  $R^2$  value of 0.9418, showing that the exponential curve fit is fairly good.

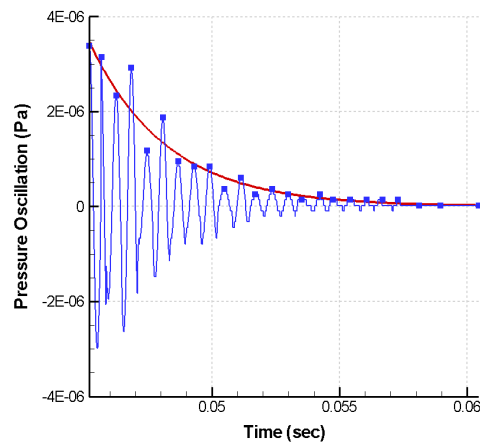


Figure 3.29: Exponential curve-fit for the conditions of Figure 3.28

It is expected that since exponential behavior was observed for this case, that similar behavior will occur once response functions are introduced into the code. Although experimental matching of growth and decay rates is difficult in analyzing combustion instability, it is important that the same qualitative behavior is observed. The growth and decay of pressure oscillations is discussed in more detail in CHAPTER 6 when response functions are examined.

### 3.3.4. Results of the 15, 20, and 35 inch Chamber Cases

The results for the other chamber length cases are now shown in the same manner as the 25 inch case results. For broadband small amplitude forcing, the FFT plot at positions one, two, and three will be shown for each chamber length case. The corresponding pressure mode shapes of the first four modes are then shown, where the scales are identical so that the relative amplitudes of the four modes can be seen directly. Finally, the pressure and velocity mode shapes are plotted together for the acoustic mode which most closely matches the unstable experimental mode. The FFT plot for the 15 inch chamber is shown in Figure 3.30.

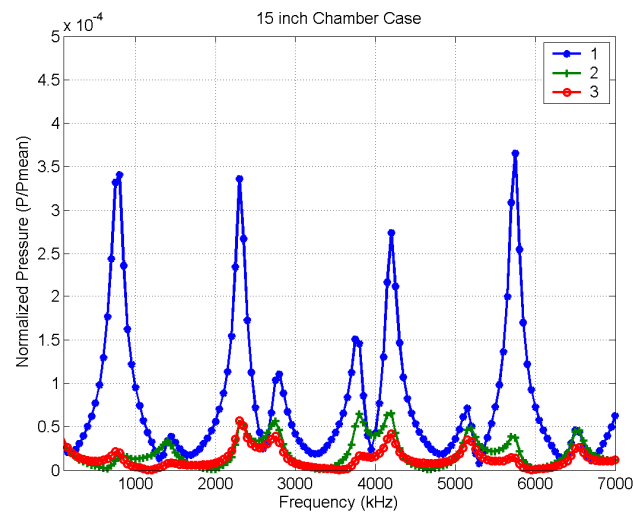


Figure 3.30: FFT plot of the 15 inch chamber case forced with small amplitude, broadband mass flow forcing

The first four modes occur at 800 Hz, 1450 Hz, 2300 Hz, and 2800 Hz. The pressure mode shapes for each of these modes are shown in Figure 3.31.

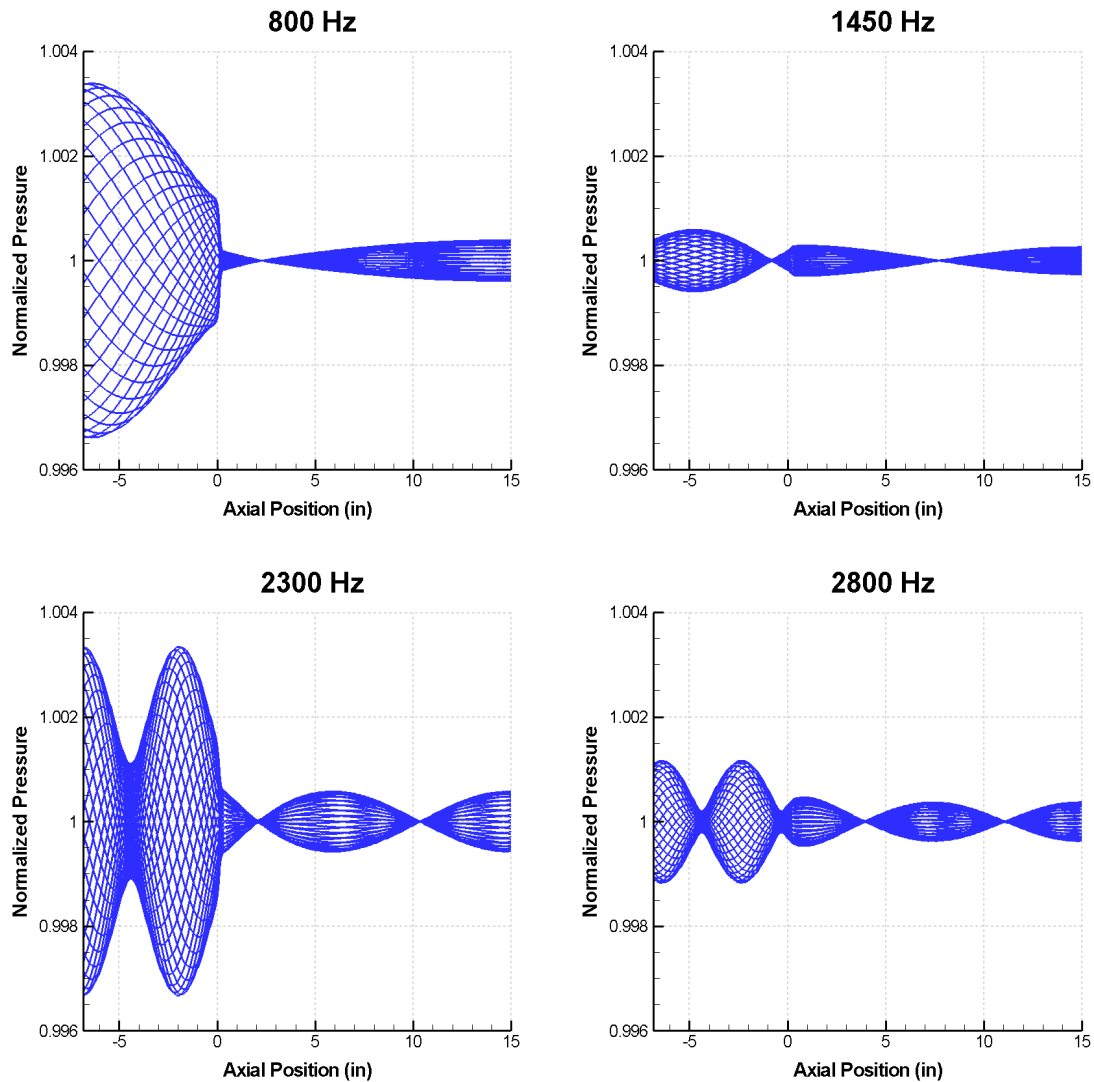


Figure 3.31: Mode shapes at 800 Hz, 1450 Hz, 2300 Hz, and 2800 Hz for a 15 inch chamber

The 800 Hz mode appears to correspond to the injector  $\frac{1}{2}$  mode. The 1450 Hz mode corresponds to the chamber 1<sup>st</sup> mode. The 2300 Hz mode corresponds to the injector  $\frac{3}{2}$  modes combined with the chamber 2<sup>nd</sup> mode. The 2800 Hz mode appears to be some kind of coupled mode. Note that the mode shape with the closest relative amplitudes between the injector and chamber is

the 1450 Hz mode, which corresponds to the unstable frequency in the experiment. The pressure and velocity mode shapes at the unstable frequency (1450 Hz) are shown in Figure 3.32 on the same plot.

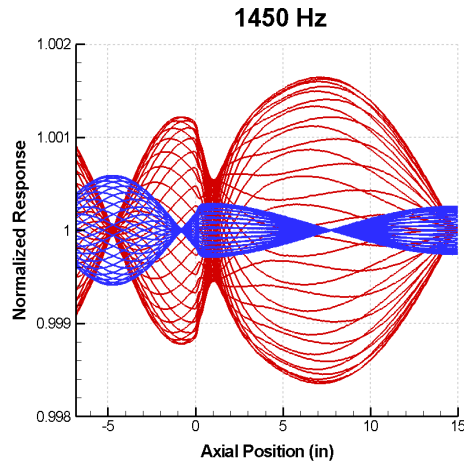


Figure 3.32: Pressure (blue) and velocity (red) mode shapes for a 15 inch chamber forced at 1450 Hz with small amplitude forcing

The FFT plot for the 20 inch chamber case is shown in Figure 3.33. The first four modes occur at 700 Hz, 1150 Hz, 1950 Hz, and 2450 Hz. The pressure mode shapes for each of these modes is shown in Figure 3.34.

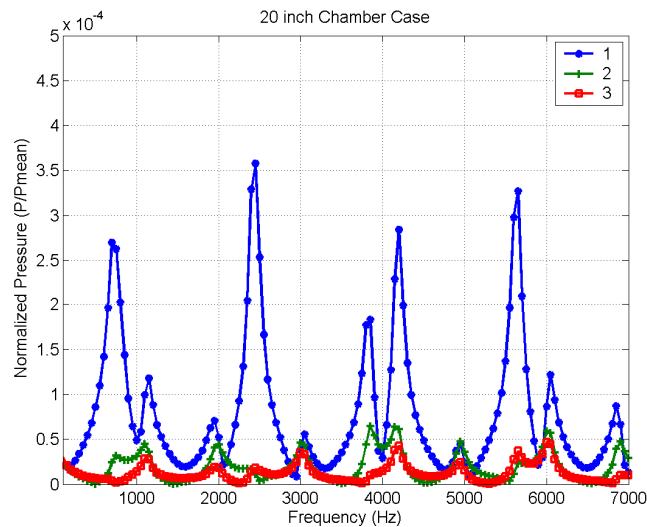


Figure 3.33: FFT plot of the 20 inch chamber case forced with small amplitude, broadband mass-flow forcing



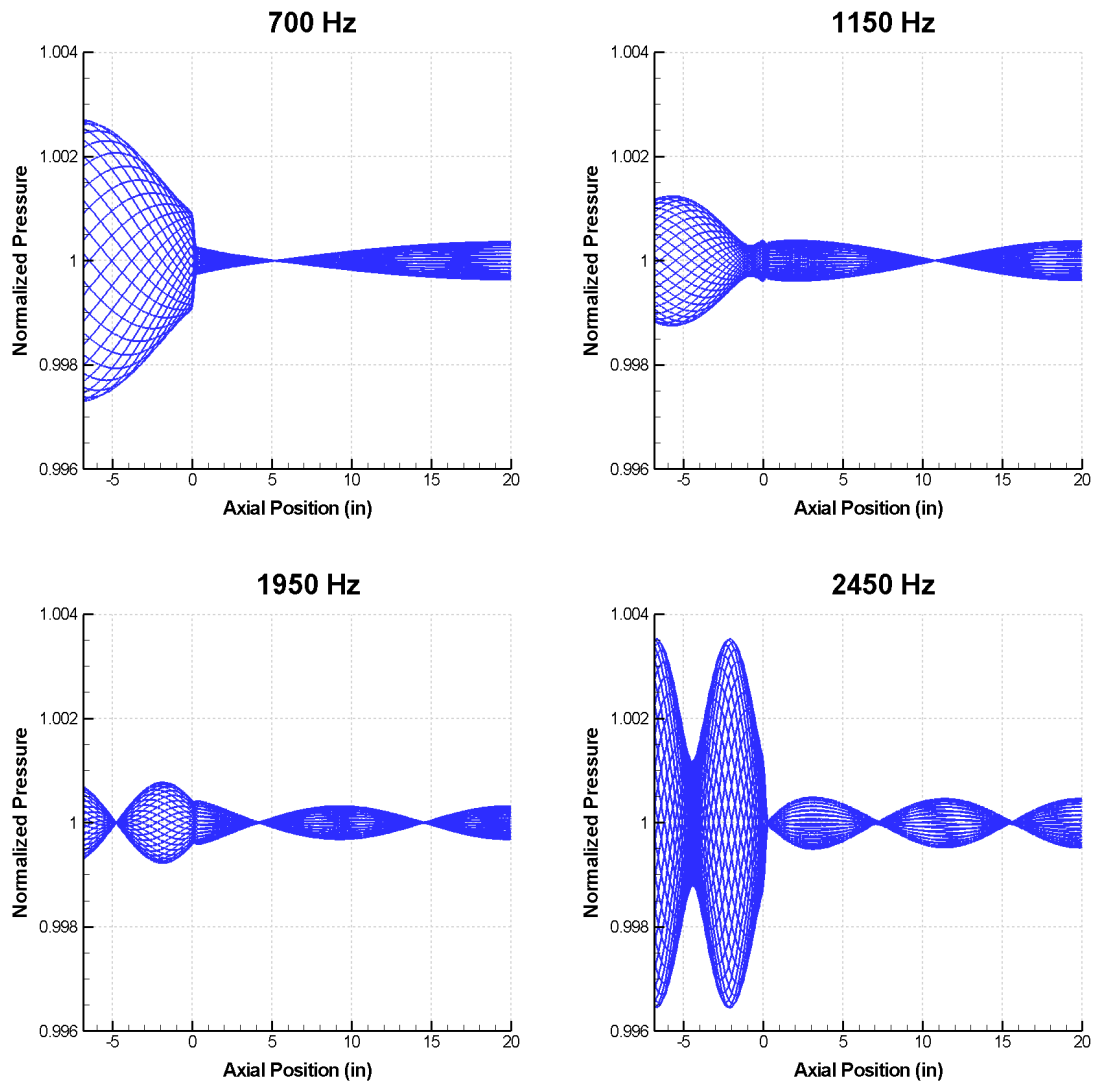


Figure 3.34: Mode shapes at 700 Hz, 1150 Hz, 1950 Hz, and 2450 Hz for a 20 inch chamber

The 700 Hz mode appears to correspond to the injector  $\frac{1}{2}$  mode. The 1150 Hz mode is close to the 1st chamber mode. The 1950 Hz mode corresponds to the chamber 2<sup>nd</sup> mode. The 2450 Hz mode corresponds to the injector  $\frac{3}{2}$  mode. Note that the mode shape with the closest relative amplitudes between the injector and chamber is the 1950 Hz mode, which does not correspond to the experimental unstable frequency. The pressure and velocity mode shapes at the unstable frequency (1150 Hz) are shown in Figure 3.35.

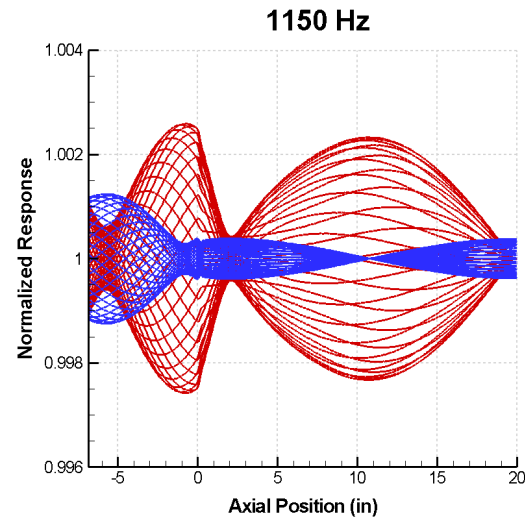


Figure 3.35: Pressure (blue) and velocity (red) mode shapes for a 20 inch chamber forced at 1150 Hz with small amplitude forcing

The FFT plot for the 35 inch chamber case is shown in Figure 3.36. The first four modes occur at 500 Hz, 800 Hz, 1250 Hz, and 1750 Hz. The pressure mode shapes for each of these modes is shown in Figure 3.37.

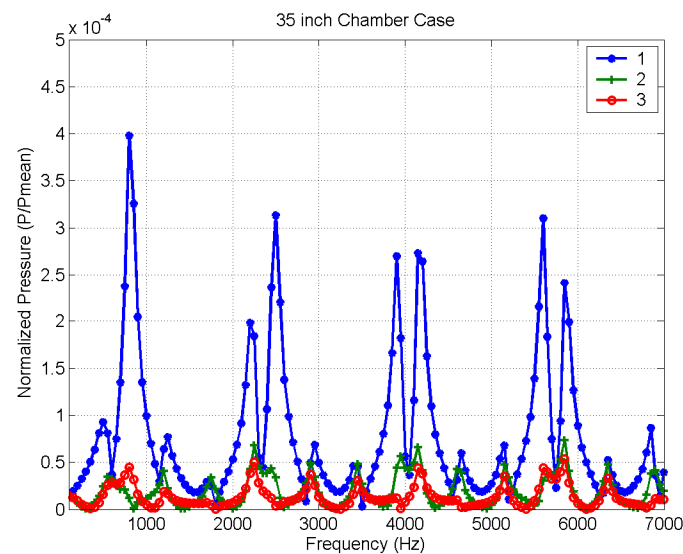


Figure 3.36: FFT plot of the 35 inch chamber case forced with small amplitude, broadband mass-flow forcing

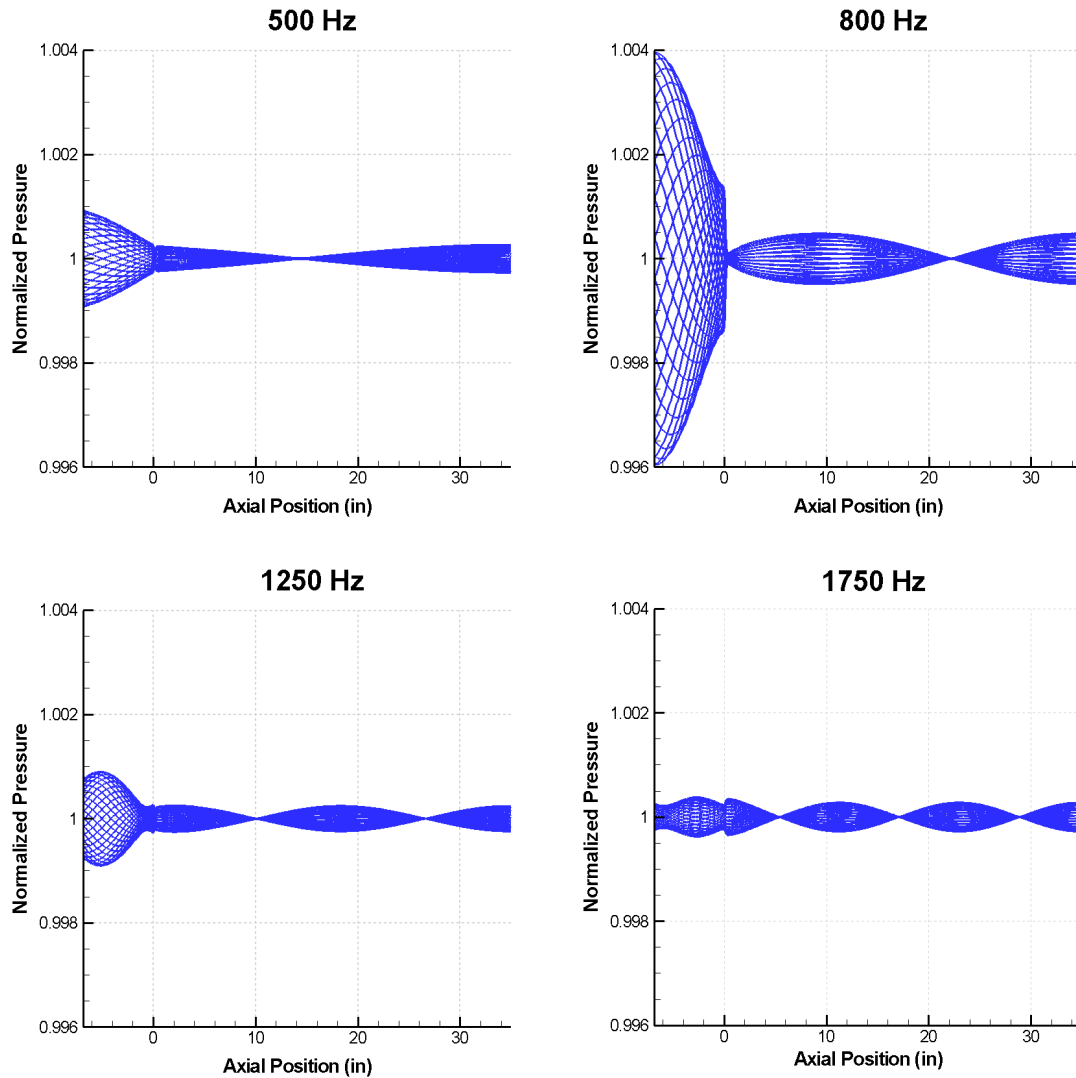


Figure 3.37: Mode shapes at 500 Hz, 800 Hz, 1250 Hz, and 1750 Hz for a 35 inch chamber

The 500 Hz mode corresponds to the chamber 1<sup>st</sup> mode. The 800 Hz mode appears close to injector  $\frac{1}{2}$  mode. The 1250 Hz mode corresponds to the chamber 2<sup>nd</sup> mode. The 1750 Hz mode corresponds to the chamber 3<sup>rd</sup> mode. The mode with the closest relative amplitudes between the injector and the chamber is the 1750 Hz mode, which was the first unstable mode encountered in the experiment. The pressure and velocity mode shapes at the unstable

frequencies (1250 Hz early in the test and 1750 Hz late in the test) are shown in Figure 3.38 on the same plot.

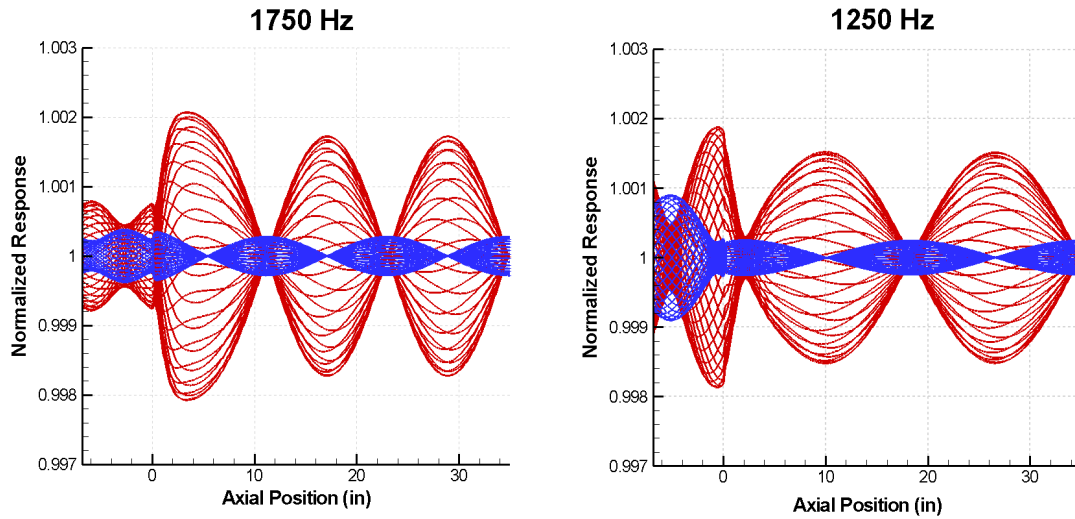


Figure 3.38: Pressure (blue) and velocity (red) mode shapes for a 35 inch chamber forced at 1750 Hz (early instability) and 1250 Hz (late instability) with small amplitude forcing

The results obtained for the 15, 20, and 35 inch cases are very similar to the results of the 25 inch chamber case. For each case it was necessary to take the FFT of the broadband forcing to identify the particular acoustic nodes. The mode shapes were plotted to investigate the nature of the mode (ie injector, chamber, or coupled). The injector modes were more difficult to interpret than the chamber modes, most likely due to the relatively high Mach number in the injector. For three of the four chamber length cases, the mode with the closest relative amplitudes between the injector and chamber corresponded to the experimental unstable mode. The only exception was the 20 inch case. In all of the chamber length cases, the unstable frequency corresponded closely to a chamber mode (1<sup>st</sup>, 2<sup>nd</sup>, or 3<sup>rd</sup>).

### 3.4. Acoustic Validation

The objective of running the full computational model is to obtain results which can be validated by the experimental data. This will determine how effective the computational model can be for future prediction. This section is confined to validating the linear aspects of the experimental data, namely the acoustic modes and the mode shapes. Small amplitude forcing is a necessary first step in validating the experimental results because it identifies the acoustic modes, one of which will be excited and grow to non-linear amplitudes if the conditions for instability are met. For this reason it is very important to model the linear acoustic modes accurately. High amplitude, non-linear forcing is addressed in CHAPTER 4.

#### 3.4.1. Validation of the 25 inch Chamber Case

The experimental results are now compared to the computational predictions for the 25 inch chamber length cases. The power spectral density plot for experimental test 25D1r (left) and the broadband FFT plot of the computations (right) are shown in Figure 3.39. The computational FFT has been forced with small amplitude broadband forcing but has been plotted on a log scale for comparison purposes. The only requirement for setting the level of forcing is that it be small enough to remain linear, which means that it should be at 0.1 % of the mean mass flow-rate or less (see Section 2.5). Because of this arbitrariness in setting the level of forcing, the PSD and FFT plots are compared with the intent of matching frequency, not amplitude. This is justified since the only difference between the two types of frequency analysis is the amplitude scaling.<sup>38</sup>

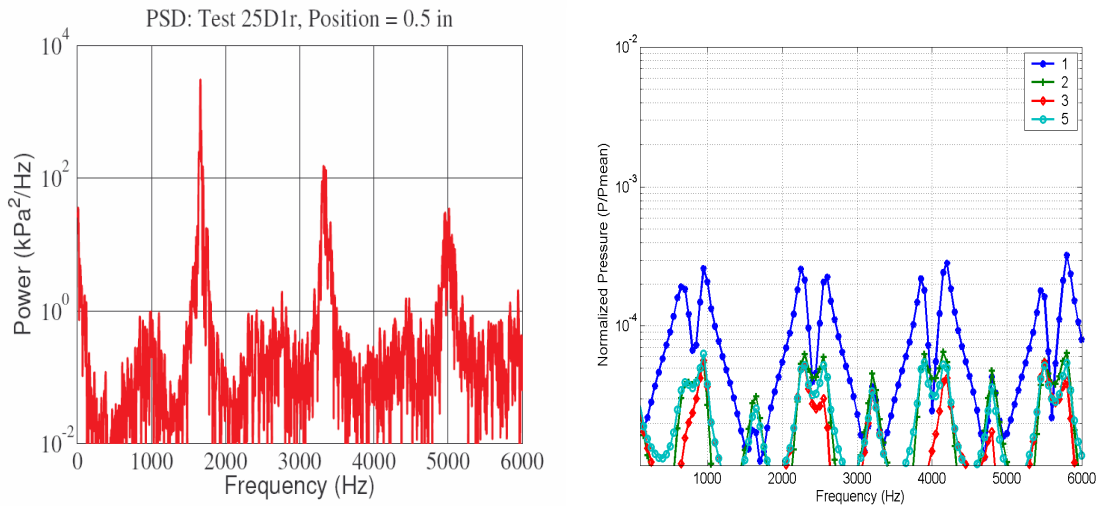


Figure 3.39: Comparison of the experimental PSD for test 25D1r (left) and the computational FFT (right) for a 25 inch chamber

The experimental PSD shows inherently non-linear behavior. The peak-to-peak pressure oscillations from the experimental tests reached greater than 40% of the mean pressure, which is strongly non-linear.<sup>4</sup> The pressure time traces also showed very steep fronted waves. The two large peaks at 3320 Hz and 4956 Hz are higher harmonic excitations of the 1660 Hz mode, which are results of the steep fronted waves.<sup>10</sup> Because the computational FFT was produced using small amplitude linear forcing, it cannot capture the non-linear nature of the experimental result. However, it can distinguish the fundamental modes of the system.

The experimental modes are estimated from the PSD for test 25D1r. Although the 1660 Hz mode and its harmonics are the only unstable modes, other modes can be estimated from the smaller peaks of the PSD. For a quantitative estimate, these were defined as those peaks that reached or exceeded a power level of 1 (10<sup>0</sup>) kPa<sup>2</sup>/Hz. Table 3-4 compares the modes from the zero mean flow analytical model, the full computational model, and the experiments for a 25 inch chamber.

Table 3-4 Mode comparison using the zero mean flow analytical model, the full computational model, and the experimental PSD plots

Mode	Analytical	Computational	Experimental
1st chamber	763	650	800-1100
	1055	950	
2nd chamber	1718	1650	1660
3rd chamber	2521	2250	2300-2500
	2946	2600	2600-2800
4th chamber	3447	3200	3350
5th chamber	4254	3850	4300-4600
	4848	4200	
6th chamber	5190	4800	4900-5100

The above table shows that there is a wide variation between the modes using the analytical, computational, and experimental methods. Because the analytical model does not take mean flow (and thus high Mach number) into account, its predicted mode frequencies are larger than the computational mode frequencies. The precision of the computational modes is limited by the specified frequency resolution. In both the analytical and computational models the temperature distribution is estimated using fairly simple models. Because the speed of sound is dependent on the temperature, this will also have an impact on the acoustic mode determination.

There is also a great deal of approximation in estimating the experimental modes from the PSD plot in Figure 3.39. The harmonics are not the same as actual linear acoustic modes, but they are the closest approximation that can be obtained from the non-linear experimental data. The difference between higher harmonics and chamber modes is that higher harmonics are simply integral

multiples of the initially unstable mode. Actual chamber modes are complex functions of the geometry and flow conditions.

The most important element for future combustion instability analysis is whether the unstable mode has been estimated accurately. This is clearly the case for the 25 inch chamber, since the computational result predicts 1650 Hz and the unstable experimental frequency is 1660 Hz.

The computational mode shapes can also be compared with the experimental data. This is done by using the  $p'_{rms}$  data from Miller<sup>10</sup> (p. 280 -281) for each of the transducer locations along the injector and 25 inch chamber (see Figure 1.10 for the transducer locations). The experimental data points and computational mode shape have been plotted together in Figure 3.40. As mentioned previously, the small amplitude forcing of the computation is arbitrary, as long as it is small enough to remain linear. In order to compare the two results, the 1650 Hz computational mode shape has been scaled so that it has the same oscillating pressure at the injector/chamber interface as the experimental  $p'_{rms}$  data at the 2.5 inch chamber transducer location. The comparison is meant to validate the relative amplitudes of the experimental data with the nodes and anti-nodes of the computational mode shape.

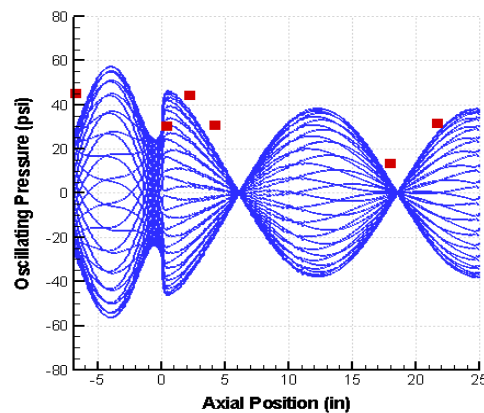


Figure 3.40:  $P'_{rms}$  experimental data points at transducer locations of test 25D1r at 1660 Hz are shown in red. The computational mode shape with small amplitude forcing at 1650 Hz for a 25 inch chamber is shown in blue.



The experimental data points appear to be shifted slightly to the right relative to the computational mode shape at the injector/chamber interface. Other than that the relative position of the experimental data appears to match fairly well with the computational mode shape. The experimental data matches the same increasing and decreasing trends as the mode shape, suggesting that nodes and anti-nodes are being modeled accurately.

### 3.4.2. Validation of all Chamber Length Cases

The linear computational analysis has predicted the experimentally observed unstable mode very closely for the 25 inch chamber, predicting 1650 Hz for an unstable mode of 1660 Hz. The computational mode shape at 1650 Hz qualitatively matches the experimental pressure data at the various transducer locations along the injector and chamber. This validation is now extended by comparing the computational results with all of the unstable tests, comprising chamber lengths of 15, 20, 25, and 35 inches. The same analysis was run for each length. The experimental chamber modes were estimated in the same way as in Table 3-4, and are plotted with the computational modes in Figure 3.41. The solid points are the computational chamber modes and the hollow points are from the experimental data.

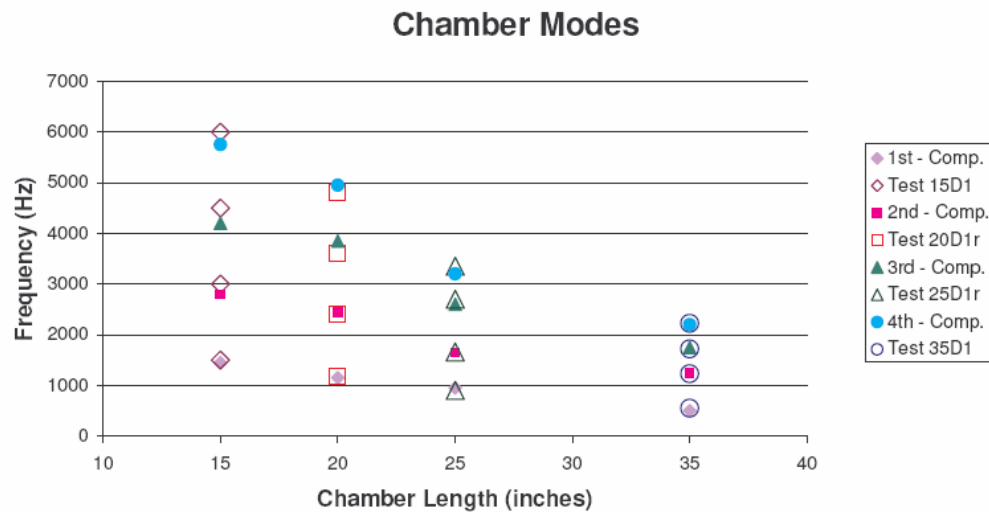


Figure 3.41: Comparison of experimental and computational chamber modes for chamber lengths of 15, 20, 25, and 35 inches corresponding to tests 15D1, 20D1r, 25D1r, and 35D1

The chamber modes appear to match fairly well, considering the approximations in determining the chamber modes from the experimental PSD plots. The agreement appears to improve as the length of the chamber increases. This can be explained by recognizing that the 15 and 20 inch test cases went unstable at the first chamber mode (see Table 3-5) and so the subsequent points are actually higher harmonics of the first mode, not actual chamber modes. The 25 and 35 inch cases went unstable at the 2<sup>nd</sup> or 3<sup>rd</sup> chamber modes, so the points are more likely to be indicative of true modes.

The decrease in mode frequency as the chamber length increases is explained from classical acoustic analysis. Referring to Equation 3.1 ( $F_n = nc/2L_c$ ), as the length of the chamber increases, the mode frequencies decrease. Because the chamber is longer, the wavelength of the mode is larger and the frequency is lower.

The most important modes (and the only ones that can be clearly identified from the experimental PSD plots) are the unstable modes. These are compared to the analytical and computational results in Table 3-5 for four of the

experimental tests. The 35 inch chamber case switched from being unstable at the third chamber mode (1721 Hz) early in the experimental run to being unstable at the second chamber mode (1233 Hz) later in the run. Both are listed in the table below. The same tests have been used as those in Figure 3.41.

Table 3-5: Comparison of unstable modes as shown by the experiments and as predicted by the analytical and computation models

Exp. Test	Unstable Mode	Analytical	Computational	Experimental
15D1	1st Chamber	1467	1450	1502
20D1r	1st Chamber	1177	1150	1184
25D1r	2nd Chamber	1718	1650	1660
35D1 (early)	3rd Chamber	1834	1750	1721
35D1 (late)	2nd Chamber	1263	1250	1233

There is very good agreement between the analytical, computational, and experimental unstable modes. Except for the 15 inch chamber test, the computational modes are well within the 50 Hz frequency interval that was specified for the broadband forcing. To further confirm that these are the correct modes, the experimental  $p'_{rms}$  data points for the unstable frequencies are plotted with the corresponding computational mode shapes using the same procedure as Figure 3.40. These comparison plots are shown in Figure 3.42. The experimental  $p'_{rms}$  data was obtained from Miller<sup>10</sup>.

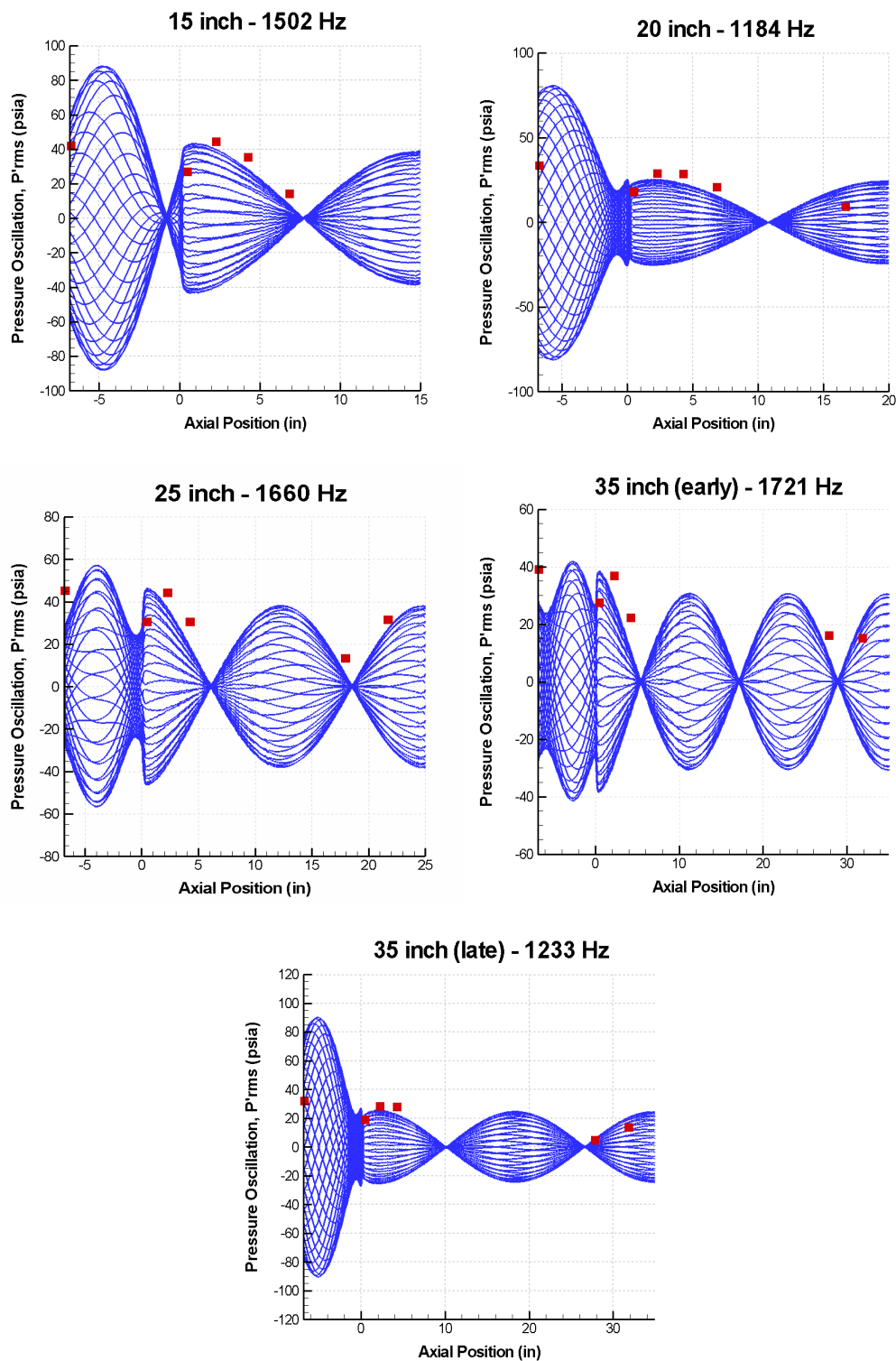


Figure 3.42: Computational (blue) and experimental (red) pressure mode shape comparisons for the unstable modes corresponding to chamber lengths of 15, 20, 25, 35 inches. The 35 inch plots include early and late unstable frequencies.

Except for a slight shift to the right, the computational and experimental comparisons show good agreement near the injector/chamber interface. The agreement towards the back of the chamber matches qualitatively, but appears to be slightly off in magnitude. In all of the above plots, the injector-head end experimental point is quite different from the computational shape at that location. This may be partly due to the incorrect inflow boundary condition at the injector head-end, since the upstream experimental boundary condition is a hard wall. Modifying the upstream boundary condition in the computational model is addressed in Section 5.3.

The injector region is possibly quite important because of its influence on instability. It is believed that when the injector and chamber magnitudes are similar in size, the modes couple and instability is more likely to occur at this frequency. However, there is a relatively high Mach number in the injector, which causes analytical and computational solutions to be very different in this region. Since there is little experimental data to compare with in the injector, validating the correct mode shape in the injector region is difficult. More experimental data points are necessary in the injector to determine how the actual shapes compare. With the given data it is difficult to determine whether the magnitude, the shape, or both are off in the injector region.

## CHAPTER 4. LARGE AMPLITUDE, NON-LINEAR FORCING

In the previous chapter, the linear acoustic modes were identified and validated for all chamber lengths. Using the full computational model (including the pertinent mean flow conditions), the unstable modes for each experimental test were predicted within about  $\pm 50$  Hz of the true frequencies. The unstable modes are the focus of the large amplitude studies, since these dominate the frequency response of the experimental PSD plots. The experimental plots in Figure 1.13 show that that the largest response is at the unstable frequency, followed by smaller responses at higher harmonics (integral multiples) of the unstable frequency. The other chamber modes show much smaller (almost negligible) responses.

Section 4.1.1 examines the non-linear response to single-mode, finite-amplitude forcing, showing the transition from linear to non-linear behavior. In Section 4.2, the non-linear results are compared with and validated against the experimental data. The computational frequency response is shown using power spectral density (PSD) plots so that direct comparisons can be made with the experimental data. In the previous chapter with small amplitude forcing, the focus was on matching the acoustic frequencies and the corresponding mode shapes. When large amplitude forcing is used, the amplitude of the frequency response can also be matched.

### 4.1. Results of Large Amplitude Forcing

Instead of broadband forcing, only the single unstable frequency is forced using large amplitude oscillations. For small amplitude oscillations, forcing at a

single frequency only gives the acoustic mode for that frequency. All mode shapes shown in the previous chapter were obtained by small amplitude forcing at a single frequency. As the amplitude increases, non-linear characteristics begin to appear and the acoustic modal energy spills over into higher integral multiples of the frequency, producing steep fronted waves and higher harmonics. Being able to characterize the non-linear behavior of the pressure oscillations accurately is imperative in modeling combustion instability correctly, since it is an inherently non-linear phenomenon.

#### 4.1.1. 25 inch Chamber Case

The PSD plot in Figure 4.1 corresponds to the 25 inch chamber case forced at 1650 Hz with a mass-flow oscillation of 0.001 % of the mean mass-flow rate. The response at positions one, two, and five are shown (see Figure 2.3 for the designation of output locations). This small amplitude forcing results in a linear response, since the dominant peak at 1650 Hz is about seven orders of magnitude higher than the next largest peak.

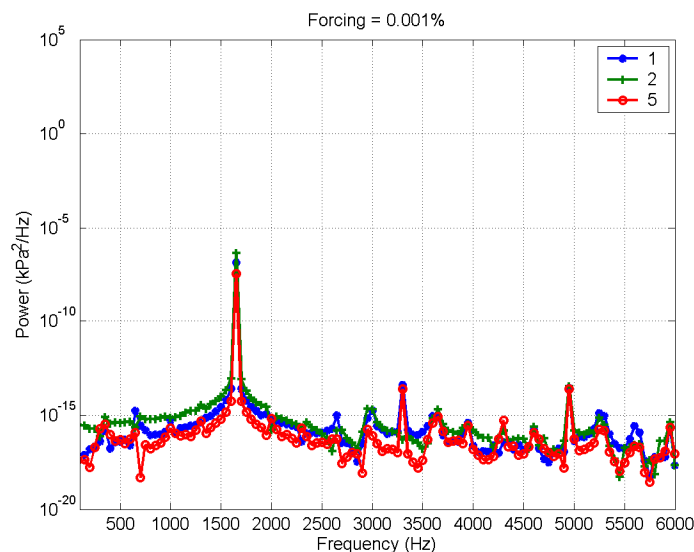


Figure 4.1: PSD plot of the 25 inch chamber forced at 1650 Hz and 0.001% of the mass-flow rate

As the forcing is increased, higher harmonics appear in the forced frequency response, becoming significant at a mass flow-rate forcing of about 1%. Results for the 25 inch chamber forced at 1650 Hz with a 1% forcing of the mass-flow are shown in Figure 4.2. Higher harmonics can clearly be seen at 3300 Hz and 4950 Hz. Although the amplitudes of the harmonics have increased, the amplitude of the forced frequency at 1650 Hz is still approximately four orders of magnitude larger than the first harmonic at 3300 Hz. Note that the same scaling is retained in Figure 4.2 (and in Figure 4.3 and Figure 4.4 shown below) as in the “linear” response in Figure 4.1 to show the increase in overall magnitude of the response.

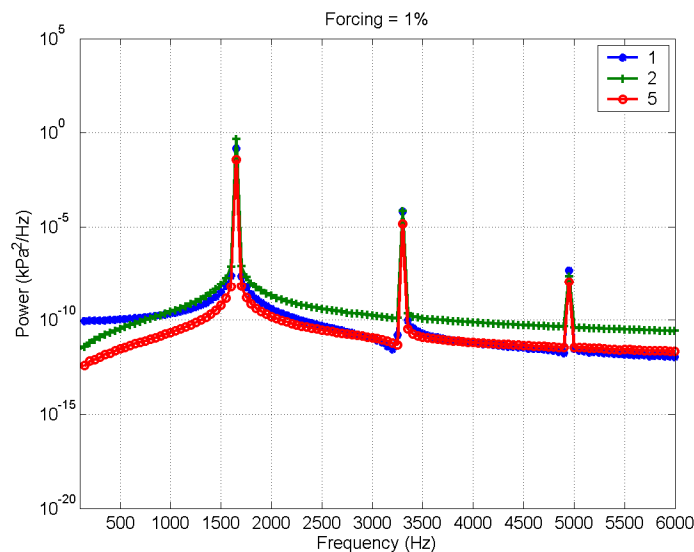


Figure 4.2: PSD plot of the 25 inch chamber forced at 1650 Hz and 1% of the mass-flow rate

At a perturbation of 10% of the mass-flow rate (Figure 4.3), the first harmonic has grown until it is within approximately two orders of magnitude of the forced frequency. Although all three peaks have increased in magnitude relative to Figure 4.2, the larger forcing has caused a greater relative change in the harmonics than in the forced peak. The forced peak has grown by



approximately two orders of magnitude, the first harmonic by four, and the second harmonic by five. This indicates strong non-linear behavior in the frequency response.

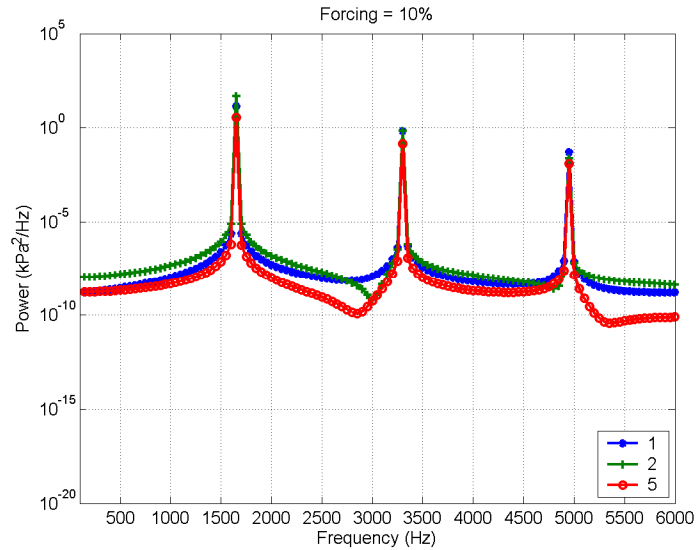


Figure 4.3: PSD plot of the 25 inch chamber forced at 1650 Hz and 10% of the mass-flow rate

When the forcing is set at 50% (Figure 4.4), the computational response approaches the magnitude of the experimental response. Further, the first harmonic has grown until its amplitude is within an order of magnitude of the forced frequency. The amplitude of the second harmonic is within an order of magnitude of the first harmonic.

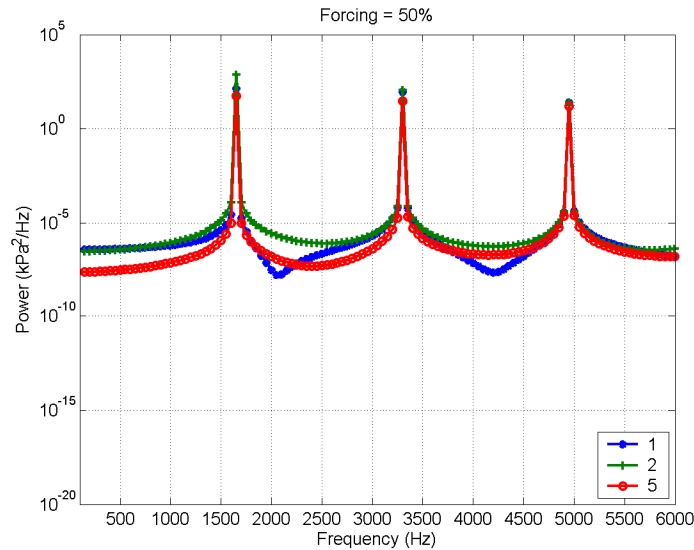


Figure 4.4: PSD plot of the 25 inch chamber forced at 1650 Hz and 50% of the mass-flow rate

For all of the PSD plots that have been shown in this section, only single frequency forcing has been used. No other modes have been forced, yet higher harmonics have still appeared and grown as the forcing increased. This shows that the higher harmonics are caused by high amplitude, non-linear forcing and not by the excitation of other acoustic modes. This further demonstrates how non-linear higher harmonics are different from linear acoustic modes.

It should be noted that there is a maximum amplitude at which the computations can be forced. The maximum amount of forcing that the computational model will currently allow is around 80 - 90% of the mean mass flow-rate. Forcing at a magnitude higher than this causes the code to diverge. In other words, the growth of the oscillation increases so dramatically (or the oscillation is so large) that the code terminates and a limit cycle, or a 'converged' condition, cannot be established. This is possibly due to one of the flow conditions becoming non-physical during the oscillation cycle, such as the temperature becoming negative. It may be possible to increase this forcing limit by decreasing the time step,  $\Delta t$ . The results show that even with the current

maximum forcing limit, a large range of non-linearity is possible with the computational model.

The effects of the higher harmonics that appear in the frequency response can be investigated further by examining the actual pressure histories that the PSD plots were obtained from. The pressure history plot for large amplitude (50%) forcing at 1650 Hz is shown in Figure 4.5.

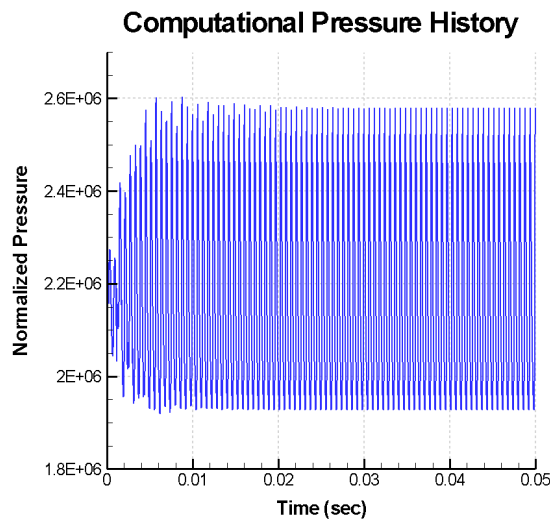


Figure 4.5: Pressure history for a 25 inch chamber forced at 1650 Hz and 50% of the mean mass flow-rate

As described in Section 2.5, the mass flow-rate is oscillated by applying a perturbation as a sine wave function. Convergence of the oscillation causes an initial growth region, followed by a converged region where the maximum and minimum oscillations are constant. For small amplitude forcing, the resulting wave appears as a simple sine wave all throughout the combustor. When single frequency, large amplitude forcing is applied, the character of the wave changes. The pressure histories at the injector/chamber interface (position 2) are compared for small amplitude forcing (left) and large amplitude forcing (right) in Figure 4.6. In both plots the solutions have reached a converged state.

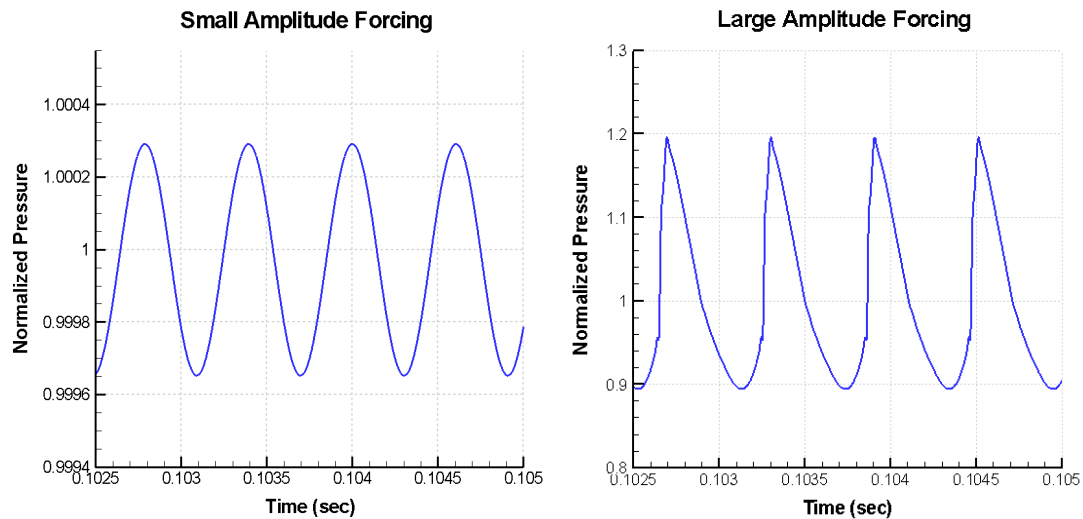


Figure 4.6: Comparison of pressure history traces for small (left) and large (right) amplitude forcing at 1650 Hz for a 25 inch chamber

When large amplitude forcing is applied, the pressure wave becomes steep fronted and appears more like a shock wave. This is due to the higher harmonics included in the wave. The response to the small amplitude forced wave includes only the 1650 Hz frequency at which it was forced. The response of the large amplitude forced wave includes the 1650 Hz frequency as well as all of the significant harmonic frequencies. A wave that included an infinite number of higher harmonics would appear as a vertical line (pressure discontinuity) in the pressure trace.

Of note is also the asymmetry of the large amplitude forced wave. The small amplitude forced wave is symmetrical about its mean pressure, in that the oscillation greater than the mean is the same size as the oscillation below the mean. However, the large amplitude forced wave shows an oscillation above the mean which is almost twice as big as the oscillation below the mean. This same occurrence can be seen in experimental non-linear waves, which will be shown in Section 4.2.1.

The effects of large amplitude forcing can also be observed in the mode shapes. In the mode shape plots of Figure 4.7, progressively larger mass-flow

forcing is applied to a 1650 Hz mode shape. The '0.1% Forcing' plot repeats the mode shape for small amplitude forcing. The other three plots show the mode shapes for large amplitude forcing (10%, 20%, and 50%).

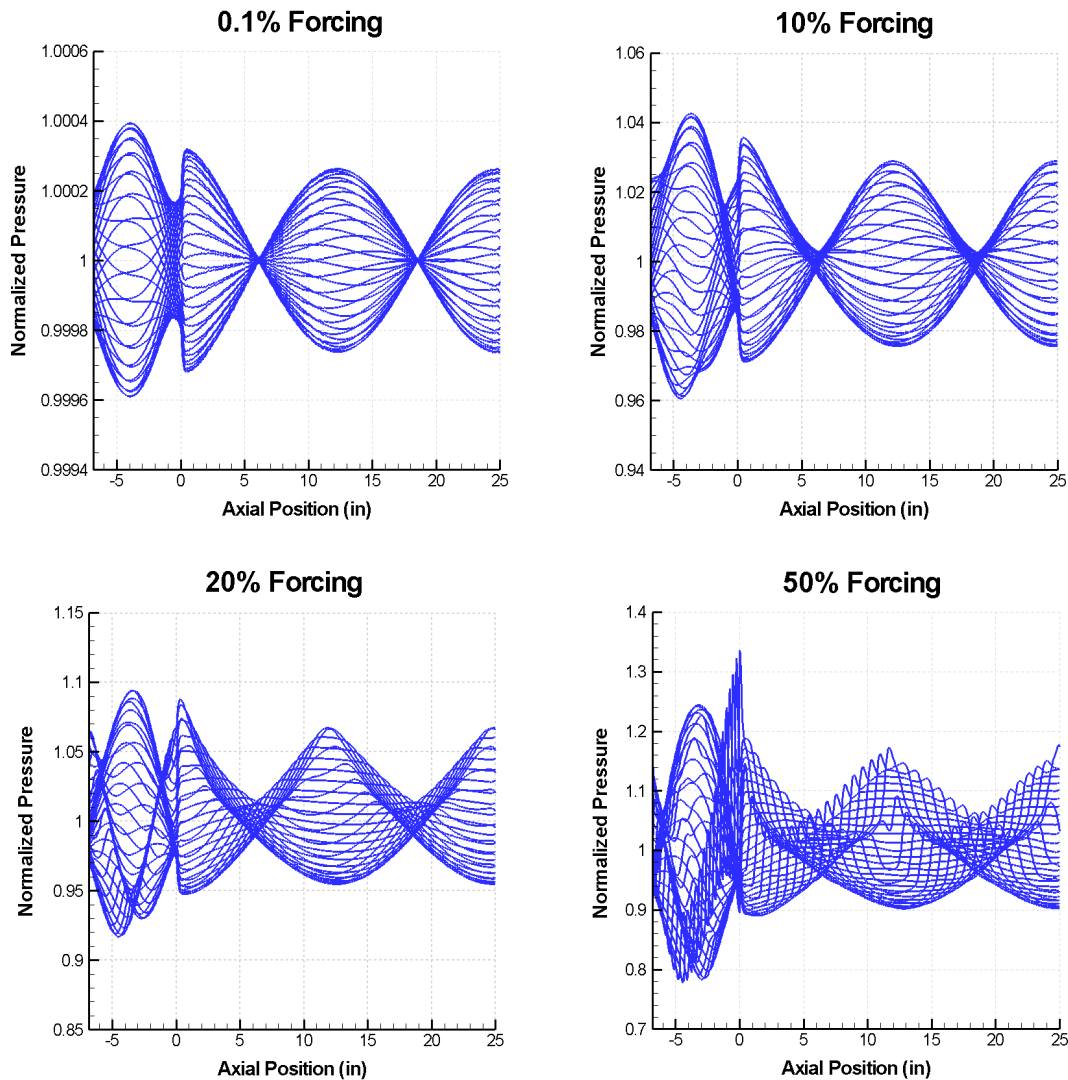


Figure 4.7: Mode shapes forced at 1650 Hz and 0.1%, 10%, 20%, and 50%.

The mode shapes become increasingly more complicated as the forcing is increased. As the higher harmonics grow in magnitude, the pressure nodes in the response broaden to regimes of finite (as apposed to zero) response. The mode shapes corresponding to these higher harmonics do not all have nodes at the

same location as the 1650 Hz mode. The presence of these additional modes causes blurring of the nodes, as indicated by Figure 4.7. The increased wave steepening shown in Figure 4.6 also contributes to the appearance (and propagation) of steep waves in the chamber and injector.

#### 4.1.2. Oscillation in the Throat Region

In Section 2.3.2, the justification for adding a diverging nozzle to the computational domain was discussed. This diverging section was necessary to ensure that the flow remained supersonic at the outflow boundary, regardless of the magnitude of the mass flow forcing. The supersonic flow would then maintain an appropriate exit boundary condition throughout the computational run.

The oscillation in the throat is now looked at in more detail to verify that the expected behavior does indeed occur. By oscillating at high amplitude, the Mach number in the throat should oscillate about the sonic point ( $M = 1.0$ ), going back and forth between subsonic and supersonic flow at the throat. To adequately capture the behavior at the throat, it was necessary to increase the number of grid points above the 501 points that was used in Section 2.3.3. This is necessary due to the propensity of one-dimensional computations to place the sonic point between grid points. In other words, even though the throat grid point represents the smallest area grid point, the code does not force the Mach number to be equal to one at this location. Instead, the sonic point occurs between this throat grid point and one of its two surrounding points. This is shown in Figure 4.8 with a Mach number plot at the throat grid point for a 501 point grid and a mass flow forcing of 0.1%. It is observed that the Mach number oscillates about a value of 1.08657 instead of 1.0.

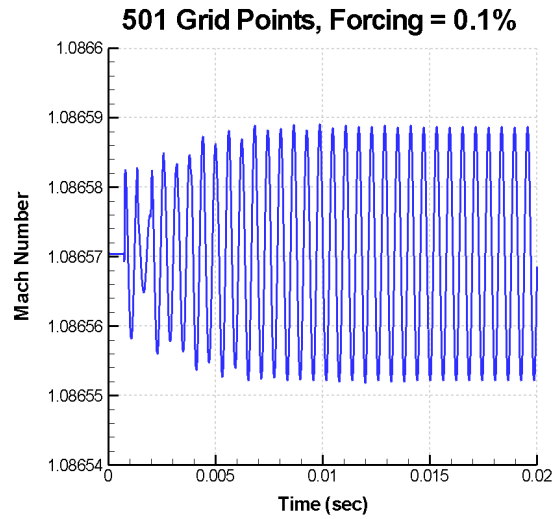


Figure 4.8: Mach number plotted at the throat grid point for a 501 point grid with a mass flow forcing of 0.1%

Because a higher resolution was necessary to find a grid point at where the Mach number oscillated about 1.0, the number of grid points was increased by a factor of 10 to 5001 points. The Mach number plot at the throat grid point is shown in Figure 4.9 for a 5001 point grid with a mass flow forcing of 0.1%.

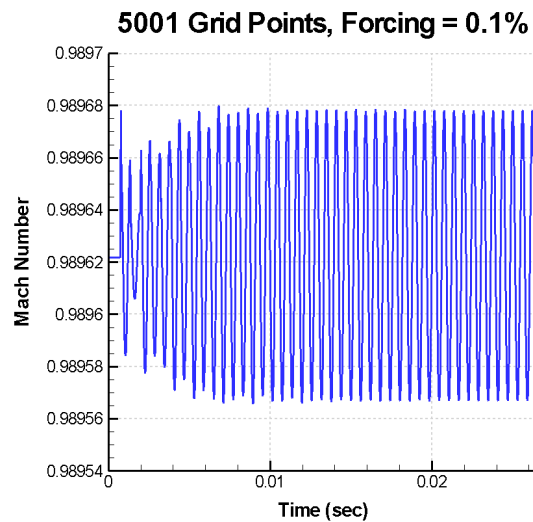


Figure 4.9: Mach number plotted at the throat grid point for a 5001 point grid with a mass flow forcing of 0.1%

Although the mean Mach number is much closer to 1.0 (0.9896 compared to 1.0866), the Mach number still does not oscillate about the sonic point. In order to force the response to oscillate about one, the mass flow forcing is increased to large amplitude forcing of 50%. This introduces non-linear behavior, but should still show the desired oscillation about the sonic point. The Mach number plot in Figure 4.10 shows that this does indeed occur (left). The plot on the right is a close-up view of some of the last cycles.

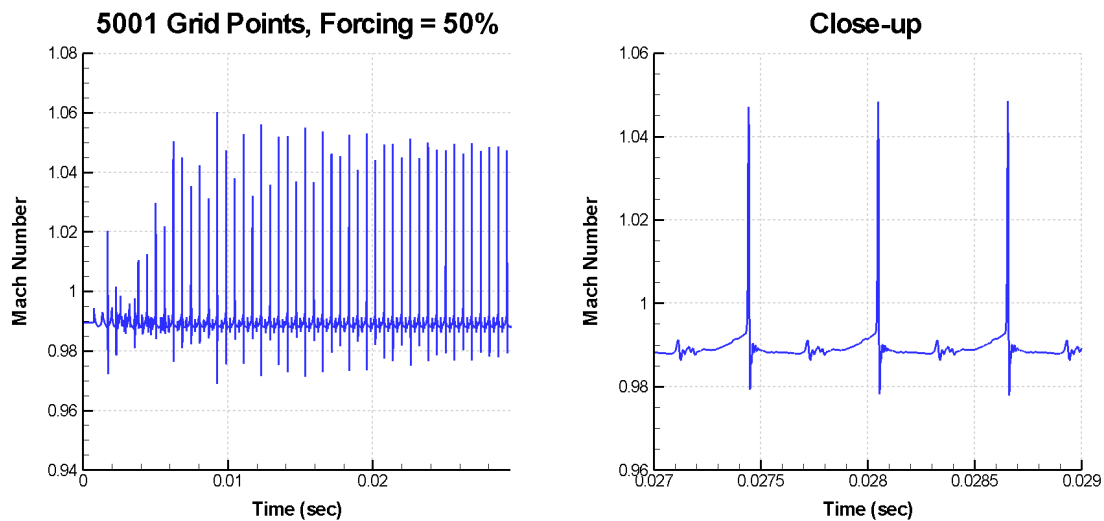


Figure 4.10: Mach number plotted at the throat grid point for a 5001 point grid with a mass flow forcing of 50%

The above plot shows the Mach number oscillating about the sonic point. This shows the need for the diverging section of the nozzle so that the flow remains supersonic at the exit. This also shows that the Mach number is not being forced to be equal to 1.0 due to any kind of boundary condition or source term. The flow Mach number at the throat periodically crosses through Mach one because of the throat geometry, the governing equations, and the unsteady pressure fluctuations.



#### 4.1.3. 15, 20, and 35 Inch Chamber Cases

The PSD plots at positions one, two, and five are shown in Figure 4.11 for chamber lengths of 15, 20, and 35 inches. Each is forced at its unstable frequency and at 50% of the mean mass flow-rate. For the 35 inch case, both the early instability (1750 Hz) and the late instability (1250 Hz) are shown.

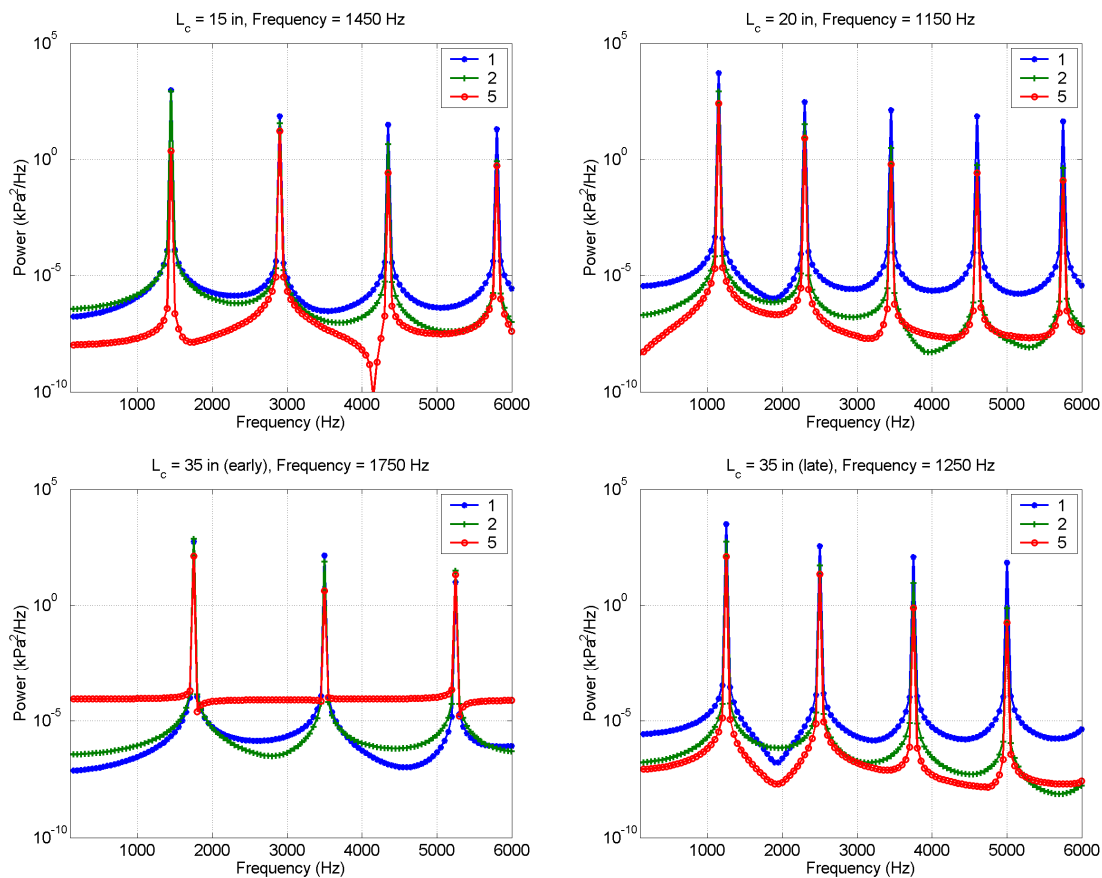


Figure 4.11: The PSD plots at positions one, two, and five are shown below for chamber lengths of 15, 20, and 35 inches. Each is forced at its unstable frequency and at 50% of the mean mass flow-rate.

The PSD plots above appear similar to the results for the 25 inch chamber case. All show the highest peak at the forced frequency and lower amplitude peaks at the higher harmonics. It is interesting to note the response of the 15

inch chamber at position five (about 7.5 inches inside the chamber). The first and third peaks at position five have relatively small amplitudes compared to the second and fourth peaks. Therefore, it is conjectured that position five is close to a node for frequencies of 1450 Hz (1<sup>st</sup> peak) and 2900 Hz (3<sup>rd</sup> peak).

The mode shapes for each chamber length are also be plotted at the same frequencies and level of forcing as above. These are shown in Figure 4.12 for 15, 20, and 35 (both early and late) inch chamber lengths for 50% mass flow forcing at the unstable frequencies.

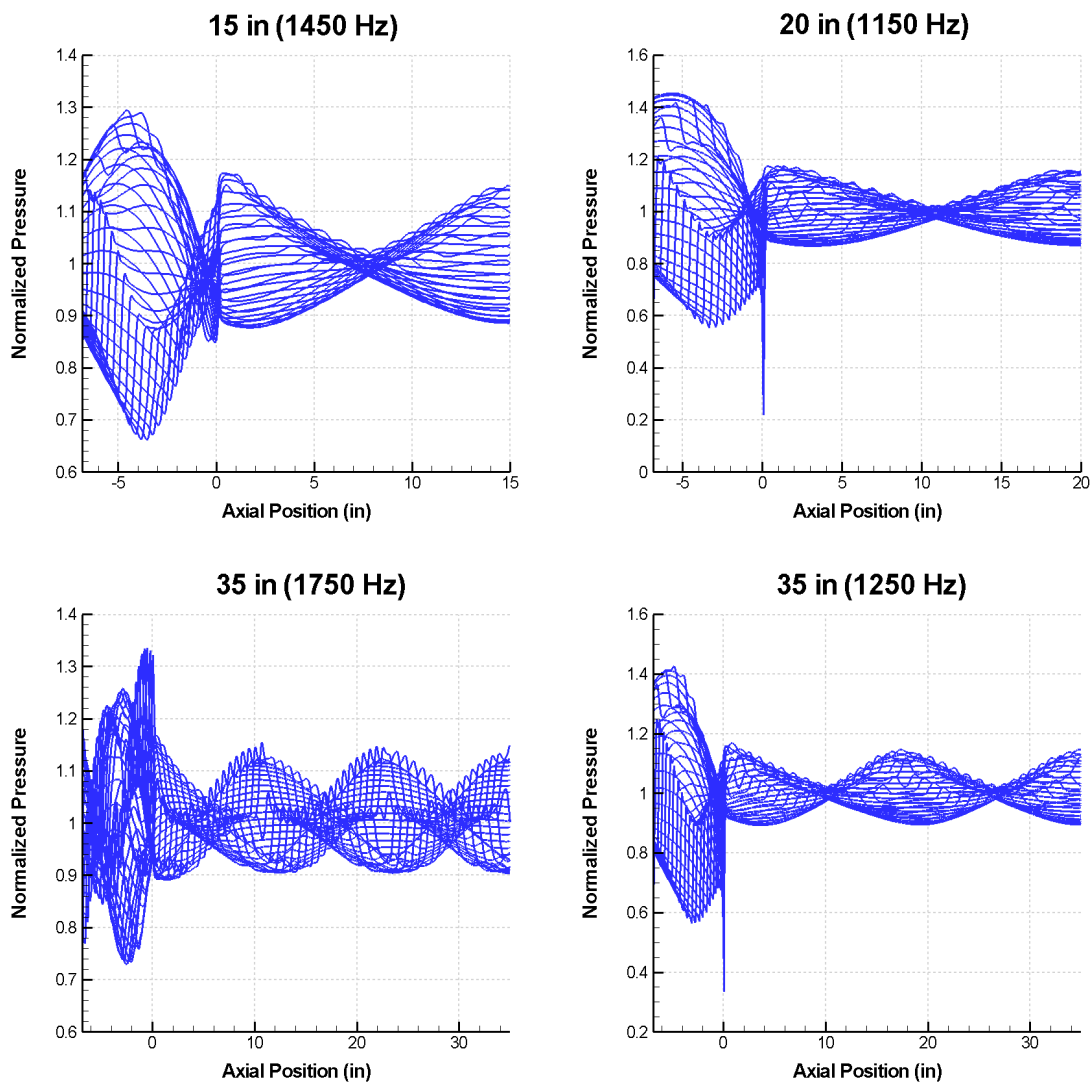


Figure 4.12: Mode shape results for 50% forcing of each chamber length (15, 20, and 35 inch) at the respective unstable frequency

As with the 25 inch large amplitude mode shape, the mode shapes for the other chamber lengths are also difficult to interpret because of their complexity. The shape in the chamber region still has the same basic shape as the small amplitude forced mode shapes, although the nodes have been blurred due to the higher harmonics. The shape in the oxidizer region has changed dramatically from the shape of the small amplitude forced results. Discontinuities can clearly be seen at the injector/chamber interface for the 20 and 35 (late) inch chamber length cases. This may be due to a grid resolution that is not large enough to adequately model the high amplitude acoustic behavior at the injector/chamber interface. It is also possible that shock formation is occurring within the injector and chamber. Note that for the 15 inch mode shape, a node exists at about 7.5 inches inside the chamber, which is roughly the same location as output position five. This shows that the PSD output and the mode shape output correspond well.

#### 4.2. Validation of Non-linear Results

Now that the effects of large amplitude forcing have been documented, the computational results can be compared with the experimental data. The objective of this section is to confirm that the non-linear behavior of the experimental data can be matched by applying an appropriate level of mass flow forcing at the unstable frequency. The computational code can predict the linear acoustic modes (as was shown in CHAPTER 3), but does not yet have the capability of predicting which mode will go unstable. This is because the effects of unsteady combustion have not yet been accounted for in the computational model. The modeling of an unsteady heat release source will be considered in more detail in CHAPTER 6. At this point, all growth and non-linear limit cycle development are due to the oscillation of the inlet mass flow-rate.

#### 4.2.1. Validation of the 25 inch Chamber Case

The experimental and computational PSD plots are compared in Figure 4.13 for the 25 inch case. The computation has been forced at 1650 Hz with a mass flow perturbation of 70% of the mean mass flow-rate.

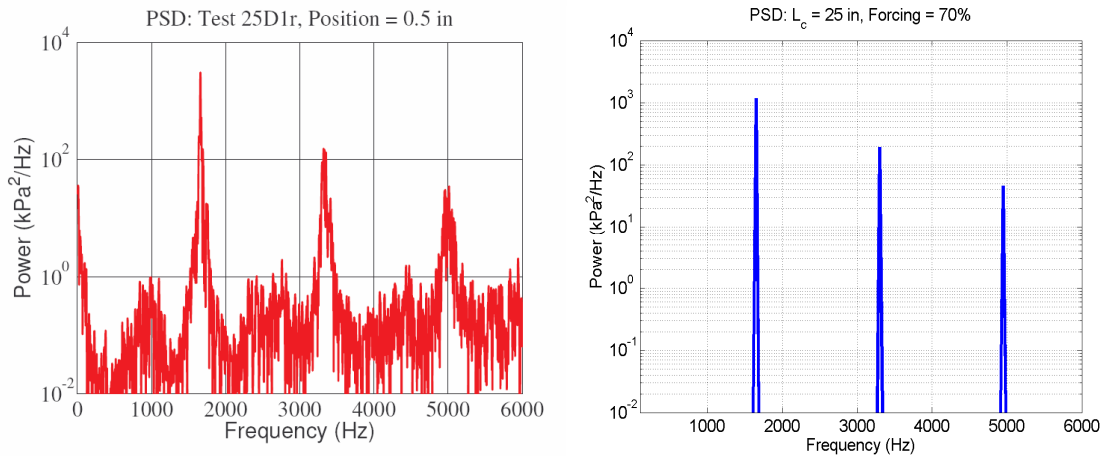


Figure 4.13: Comparison of experimental (left) and computational (right) PSD plots for the 25 inch chamber case with 70% forcing applied to the computational mass flow at position two

The experimental and computational results compare qualitatively very well for the forced frequency peak and its higher harmonics. Because the computation is forced at 1650 Hz, no off-resonance modes are excited in the computational PSD plot. Other modes are being excited in the experimental PSD plot, although at amplitudes much lower than the unstable mode and its harmonics. These same trends are seen in Figure 4.14, as the pressure history traces for the experimental and computational results are compared.

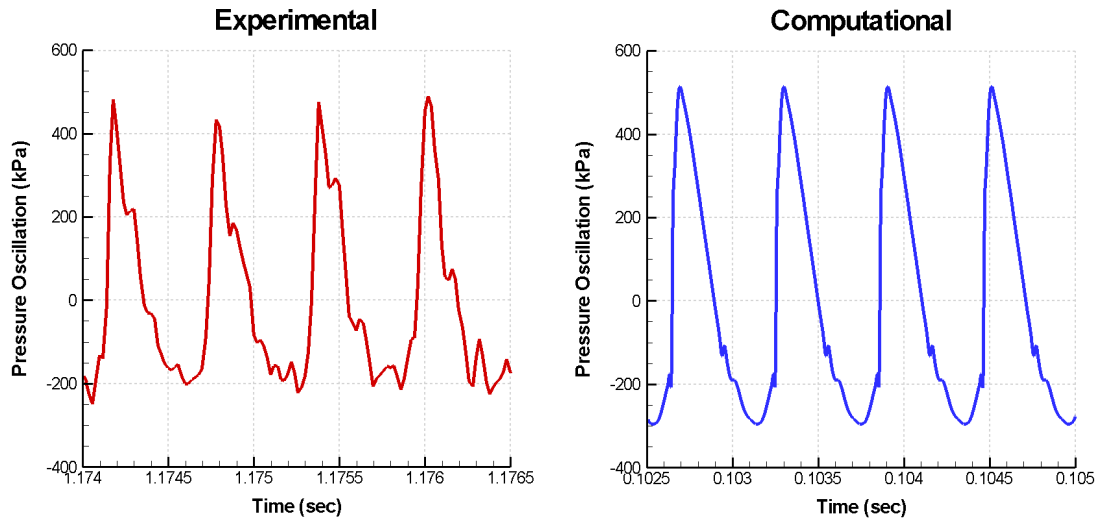


Figure 4.14: Comparison between experimental (left) and computational (right) pressure history traces for a 25 inch chamber. The computations have been forced at 1650 Hz and 70% of the mean mass-flow rate.

The same steep-fronted behavior is observed in both the experimental and computational results, which occur because of the higher harmonics. The experimental data is also influenced by the excitation of smaller amplitude modes which are not observed in the computational data. This is most apparent in the second, smaller spike that can be seen in each fluctuation of the experimental data. These smaller modes do not occur in the computational results because the code is only being forcing at 1650 Hz. Note that both the experimental and computational pressure traces in Figure 4.14 show approximately the same level of asymmetry in the oscillations, with the maximum peak being about twice as big as the minimum peak.

The non-linear computational mode shapes can also be compared with the experimental mode shapes, as was done in CHAPTER 3. The same type of scaling was performed for these comparisons as was done in Figure 3.40.

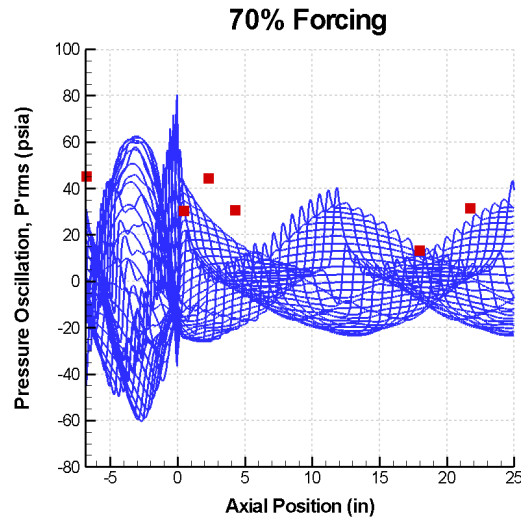


Figure 4.15: Comparison between experimental data and the computational mode shape for 70% forcing

The comparison does not appear to match quite as well as the comparison in Figure 3.40. This is most apparent at the injector/chamber interface where there appears to be a shock in the computational mode shape but not in the experimental data. However, the trends for nodes and anti-nodes still match for both the experimental and computational results. Of note is the second to last experimental data point, which is located very near to a node, but still has a non-negligible amplitude. This may be due to the blurring of the nodes that occurs when higher harmonics are present.

#### 4.2.2. Validation of All Chamber Length Cases

The experimental and computational PSD plots are now compared for all of the chamber length cases. The 15, 20, and 25 inch cases are compared in Figure 4.16. The experimental and computational results for the 35 inch chamber case are compared in Figure 4.17 for both the early (1721 Hz) and late (1233 Hz) instabilities.

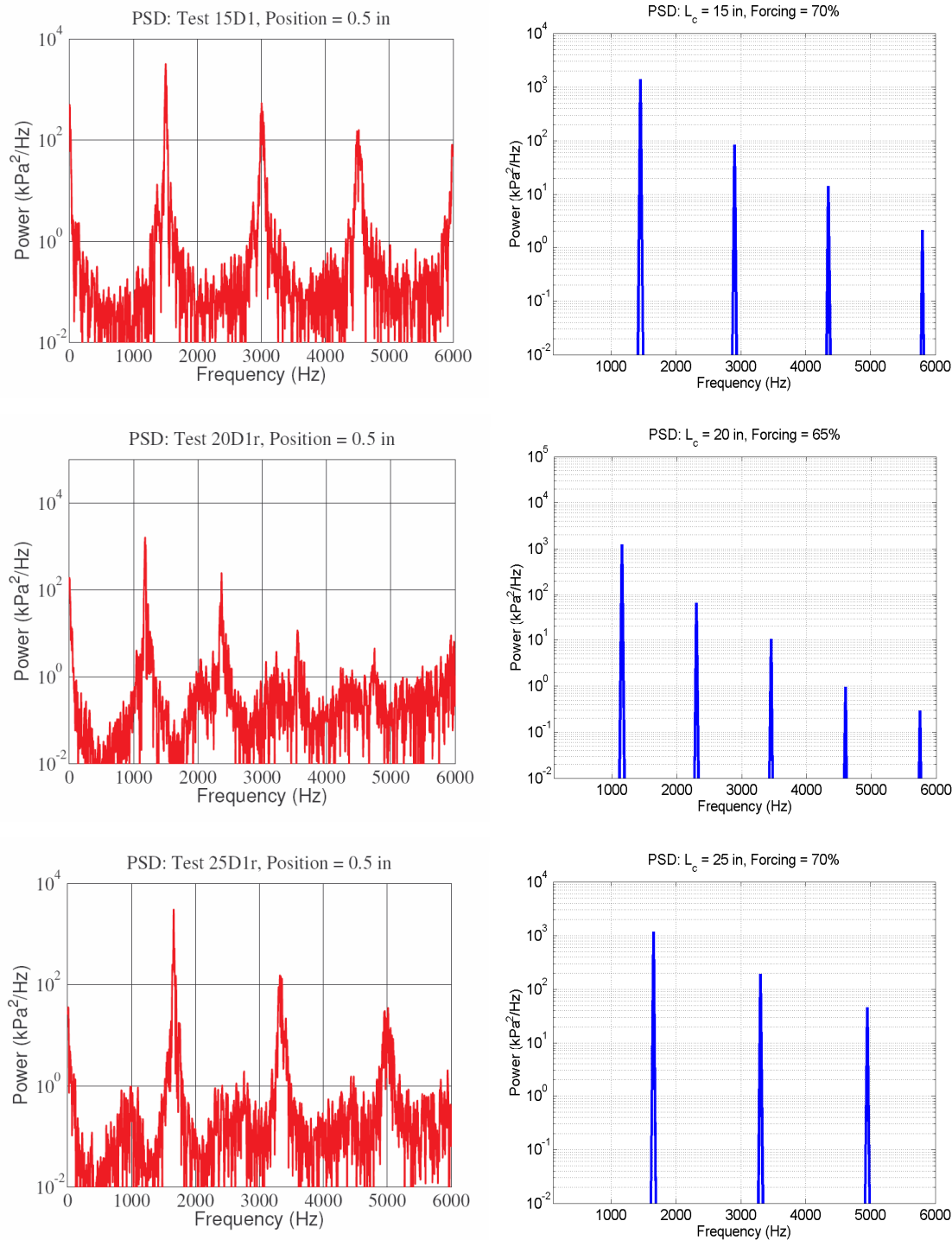


Figure 4.16: PSD experimental (left) and computational (right) plots for chamber lengths of 15 inches (1502 Hz), 20 inches (1184 Hz), and 25 inches (1660 Hz)

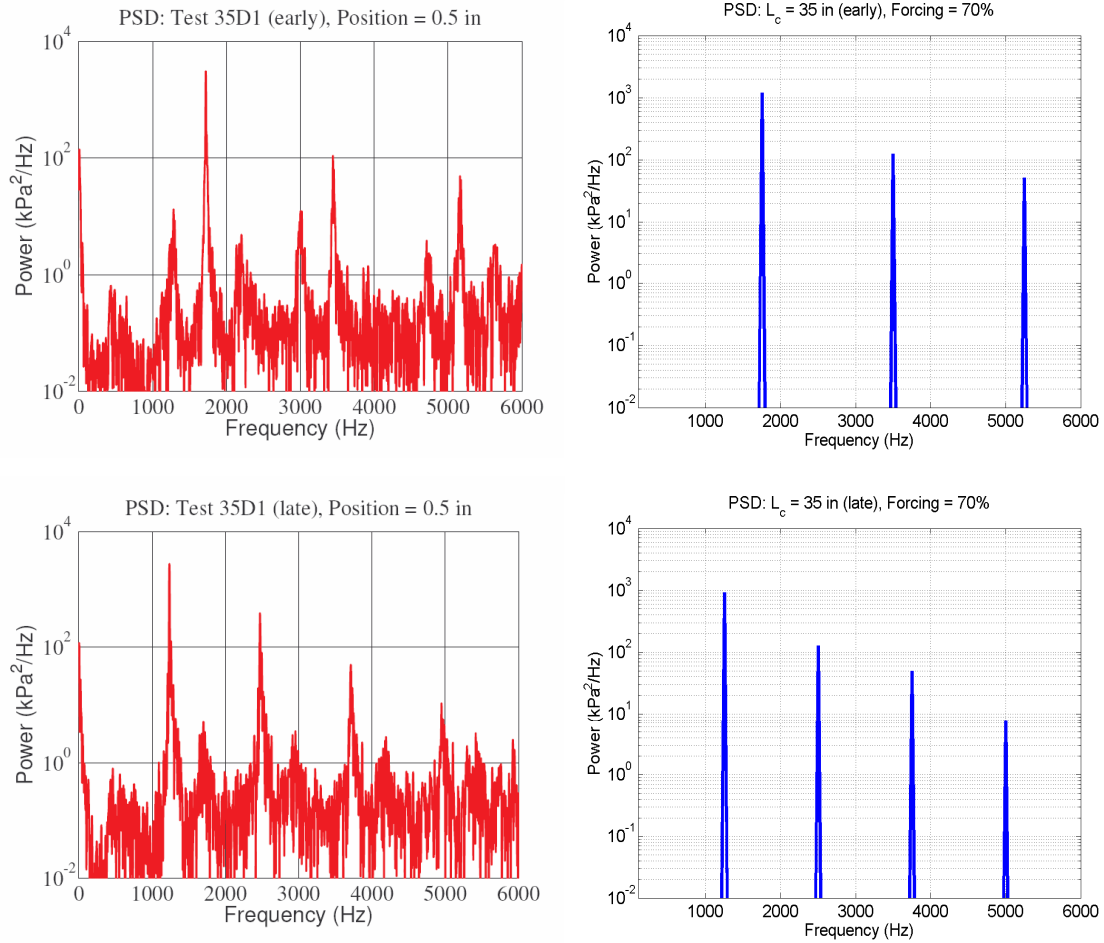


Figure 4.17: PSD experimental (left) and computational (right) plots for the 35 inch chamber length for the early (1721 Hz) and late (1233 Hz) instabilities

The results appear similar to the 25 inch chamber case, as a high initial peak and subsequent higher harmonics appear in both the computational and experimental results. For most of the results, the computational response is slightly lower in magnitude than the experimental response. This is due to the limitations in how large of forcing can be used in the computational code. If the forcing is too large, the code will diverge. The initial peak of the computational results is still always within a half order of magnitude of the experimental results. Overall, the qualitative non-linear behavior is matched very well, and the magnitude of the response is matched fairly well.



## CHAPTER 5. BOUNDARY CONDITION STUDIES

In the previous two chapters the linear acoustics and non-linear behavior of the computational model have been validated using the experimental data. Before moving on to the formulation of heat release response function models (CHAPTER 6), the boundary conditions of the original computational model are evaluated for accuracy and appropriateness. For example, the experimental configuration has a hard wall boundary at the injector head-end, but the computational model has an inflow boundary condition at this location. The current chapter serves as an extension of CHAPTER 2 by modifying the upstream and downstream boundary conditions of the original computational model.

A general discussion of traditional boundary conditions for computational fluid dynamics (CFD) can be found in Section 5.1. Section 5.2 examines using different approximate downstream boundary conditions in place of the nozzle. This can be used for making future comparisons between lower-order analytical models and the computational model. In Section 5.3, the upstream inflow boundary condition of the computational model is modified to more closely match the experimental configuration. This is done by changing the inflow boundary to a wall boundary, which necessitates also adding an oxidizer source into the injector region. The formulation of this source and the subsequent steady and unsteady results are presented.

### 5.1. Traditional Boundary Conditions

For a one-dimensional code, boundary conditions must be specified on the upstream and downstream boundaries. The number of boundary conditions on each boundary depends on the particular physics of the flow. This number can be determined by using the method of characteristics, which uses the eigenvalues of the  $A$  matrix (the convection matrix). These eigenvalues correspond to the acoustic waves ( $u+c$ ,  $u-c$ ) and the downstream running particle wave ( $u$ ), where  $u$  is the flow velocity and  $c$  is the speed of sound.<sup>26</sup> The number of necessary boundary conditions corresponds to the number of waves coming from outside the domain. These serve as inputs to the flow. For example, at the upstream boundary of a subsonic flow, the  $u+c$  and  $u$  waves are entering the domain at the boundary and must be specified as boundary conditions. The waves coming from inside of the domain cannot be specified as boundary conditions since they are specified by the conditions of the flow.

The Mach number of the flow at the boundary affects the number of necessary boundary conditions. For a subsonic flow, the speed of sound ( $c$ ) is greater than the flow velocity ( $u$ ) and so the  $u+c$  and  $u$  waves travel downstream while the  $u-c$  wave travels upstream. For a supersonic flow, the flow velocity is greater than the acoustic speed, so all three waves move downstream.<sup>26</sup>

#### 5.1.1. Inflow Boundary Conditions

At the inflow boundary of a subsonic flow, two boundary conditions are required since there are two downstream moving waves. There are two physically realistic ways in which these can be specified. The first corresponds to having a large plenum upstream of the boundary, where the flow velocity is low. The conditions upstream of the boundary are representative of stagnation conditions. The stagnation temperature and stagnation pressure are specified as the two boundary conditions.

The second situation corresponds to having a choked orifice upstream of the boundary. In this case, the mass flow-rate and stagnation temperature are fixed, and thus are specified as the inflow boundary conditions. This is the upstream boundary condition which has been used in the computational model up to this point. Since the inlet flow has a subsonic Mach number, acoustic waves propagate both downstream ( $u+c$ ) and upstream out of the domain ( $u-c$ ). The particle wave ( $u$ ) also propagates downstream.

For supersonic inflow, three upstream boundary conditions are necessary since all three waves are traveling downstream. In this case, any three independent properties can be specified at the boundary. These usually correspond to stagnation pressure, stagnation temperature, and either velocity or mass flow-rate.

#### 5.1.2. Outflow Boundary Conditions

At the outflow boundary for subsonic flow, only one boundary condition is needed since there is only one upstream moving wave. This physically corresponds to specifying the back pressure as a boundary condition, since the back pressure controls the conditions at the exit for subsonic flow.

For supersonic outflow, no boundary conditions are needed (or can even be specified) because all three waves are moving downstream. In other words, no information is coming in from outside of the domain, so the conditions at the outflow boundary are completely determined by the upstream flow.

### 5.2. Approximate Downstream Boundary Conditions

In order to simplify the computational domain and decrease the computing expense, special boundary conditions can be applied which approximate the boundary conditions mentioned in the Section 5.1. The savings in computational

cost can be large, especially for multi-dimensional simulations. For example, a nozzle is geometrically complex and may require a significant number of grid points to characterize it accurately. If a nozzle can be replaced by a single boundary, the number of necessary grid points may be decreased significantly. The accuracy of these approximations must be verified to determine whether the corresponding loss of accuracy is worth the computational savings.

If lower order models are being used in conjunction with computation, these accuracy studies can also be used to validate the lower order model. If a lower-order model can only handle simple geometry, approximate boundary conditions must be applied to the model. Computational accuracy studies can then be used to determine how much confidence can be placed in the lower-order model. The opposite can also be done, as an exact analytical solution with simple boundary conditions can be used to verify a complex computational code.

Two approximate downstream boundary conditions have been applied, corresponding to a completely reflexive boundary ( $u' = 0$ ) and an admittance condition which is a function of the flow conditions.

#### 5.2.1. Choked Downstream Boundary ( $u' = 0$ )

The choked downstream boundary condition approximates quasi-steady isentropic nozzle flow in a short nozzle. For a fixed geometry and quasi-steady flow, the Mach number through a short nozzle is fixed in time at each spatial location. This means that the Mach number at the nozzle entrance is constant. If it is also assumed that the temporal variation in the speed of sound is negligible, the velocity must be fixed at this location. The  $u' = 0$  condition forces the fluctuating velocity ( $u'$ ) to be equal to zero. This is equivalent to specifying some constant velocity at the boundary.

To determine the mean velocity at the nozzle entrance, the code was first run with the full nozzle geometry under steady-state conditions. The nozzle portion was then removed and replaced with the  $u' = 0$  boundary condition,

setting  $u$  equal to the mean velocity at the nozzle entrance. From Table 2-3, the mean value of the velocity entering the nozzle is 143.7 m/s. Broadband small amplitude forcing was applied for both the nozzle and  $u' = 0$  boundary conditions for a chamber length of 25 inches. FFT analysis was performed at position 2 (the injector/chamber interface) for both sets of data. This is shown in Figure 5.1.

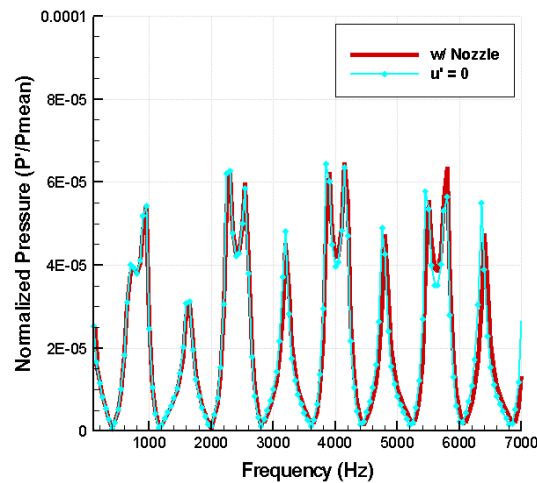


Figure 5.1: FFT comparisons between the nozzle and  $u' = 0$  boundary conditions at position 2 for small amplitude broadband forcing in a 25 inch chamber

The agreement between the two conditions is very good at lower frequencies, where the quasi-steady nozzle flow assumption is most valid. On average, the  $u' = 0$  condition tends to overestimate the pressure amplitude. There is more divergence at higher frequencies (both in frequency shift and pressure amplitude), although the difference remains relatively small. This suggests that for small amplitude forcing, the assumptions are quite accurate. With small amplitude forcing, the variation of the speed of sound is small and the flow is close to being quasi-steady. As the magnitude of forcing increases, the quasi-steady approximation becomes increasingly less valid.

The small amplitude mode shapes for both boundary conditions are compared in Figure 5.2 for a 25 inch chamber at a forcing frequency of 1650 Hz. As can be seen, the agreement between the two mode shapes appears to be

very good, especially in the chamber region. Small differences can be seen in the injector region, which most likely caused by a slight change in the steady-state injector Mach number due to the application of the  $u' = 0$  boundary condition.

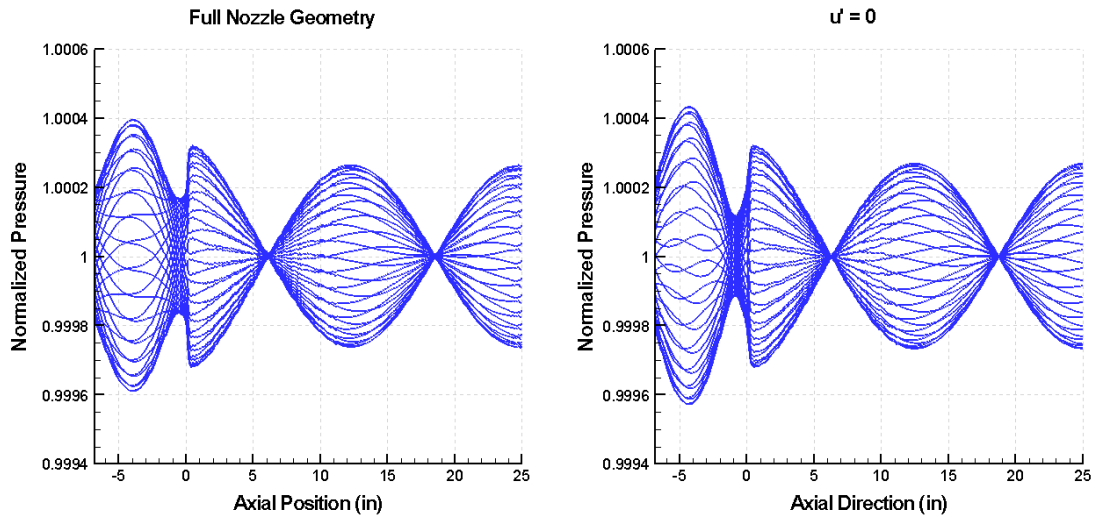


Figure 5.2: Mode shape comparison between  $u' = 0$  boundary condition and the full nozzle configuration for a small amplitude forcing.

For comparison of the two boundary conditions with high amplitude (non-linear) forcing, an FFT is performed on pressure histories forced at 1650 Hz at position 2 with a 25 inch chamber. This is shown in Figure 5.3, where the mass flow-rate has been forced at 50% of its mean value.

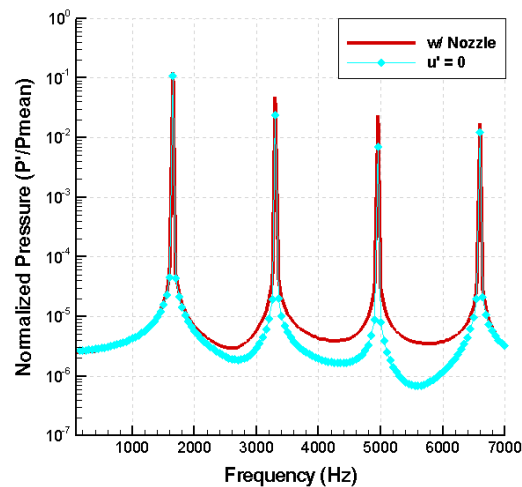


Figure 5.3: FFT comparison between the nozzle and  $u' = 0$  boundary conditions at position 2 for high amplitude forcing at 1650 Hz with a 25 inch chamber length

Figure 5.3 shows that there is still good agreement for the first resonant frequency. However, at higher frequencies the solutions diverge, with the  $u' = 0$  boundary condition showing consistently lower amplitude solutions. This divergence most likely occurs because at high amplitude forcing, the flow is no longer quasi-steady and there is significant temporal variation in the speed of sound. This was shown in Section 4.1.2 when large amplitude forcing was applied, causing large fluctuations in the throat Mach number. Therefore, the assumptions made in applying this boundary condition do not hold for high amplitude forcing.

### 5.2.2. Downstream Nozzle Admittance Boundary Condition

The downstream boundary can also be characterized with a nozzle admittance function. Because the nozzle interacts in the damping or growth of perturbations, the application of a nozzle admittance is more appropriate in working with combustion instability than a  $u' = 0$  boundary condition. The

admittance condition can be derived by performing a perturbation analysis on the continuity equation, assuming isentropic flow in a short nozzle.<sup>16</sup> The nozzle admittance takes the form:

$$\frac{u'}{p'} = A_{\text{noz}} \frac{c}{\gamma p} = M \left( \frac{\gamma - 1}{2\gamma} \right) \frac{c}{\gamma p} = \alpha \quad \text{Eq. 5.1}$$

where  $u'$  is the velocity perturbation,  $p'$  is the pressure perturbation,  $p$  is the mean pressure,  $c$  is the mean speed of sound,  $M$  is the mean Mach number, and  $\gamma$  is the specific heat ratio, all at the nozzle entrance. The admittance has units of velocity/pressure, which is equivalent to the reciprocal of the mass flux.

Using the conditions specified in Section 2.4,  $\alpha$  is approximately equal to  $4.5 \text{ e-6 m}^2\text{s/kg}$ . An FFT was then performed using the nozzle admittance boundary condition with small amplitude forcing under the same conditions as Figure 6.2. This is compared with the nozzle and  $u' = 0$  solutions in Figure 5.4.

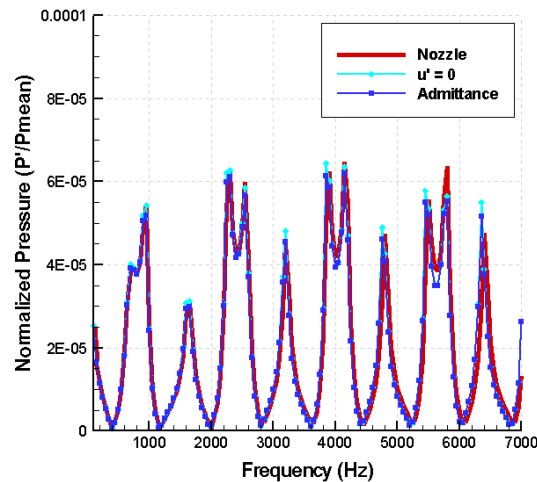


Figure 5.4: Comparison between full nozzle,  $u' = 0$  boundary condition, and nozzle admittance boundary condition for an FFT performed with linear broadband forcing at position 2 for a 25 inch chamber.



The nozzle admittance boundary condition solution closely matches the solutions of both the nozzle configuration and the  $u' = 0$  boundary condition for small amplitude forcing. Using the values in Section 2.4, the reciprocal of the steady-state mass flux is calculated as  $0.00308 \text{ m}^2\text{s/kg}$ . This can be used to normalize the admittance amplitude, which results in  $\alpha/m''_{ss} = 0.00146$ . Since the normalized nozzle admittance is relatively small, the  $u' = 0$  approximation applied in the previous section is fairly accurate. On average, the admittance condition gives a slightly lower normalized pressure amplitude than either the nozzle or the  $u' = 0$  condition.

Mode shapes were also obtained for the admittance boundary condition. The 1650 Hz mode shape is compared below with the  $u' = 0$  boundary condition mode shape. The two mode shapes are almost identical, which further shows that the  $u' = 0$  boundary condition is a good approximation for small amplitude forcing.

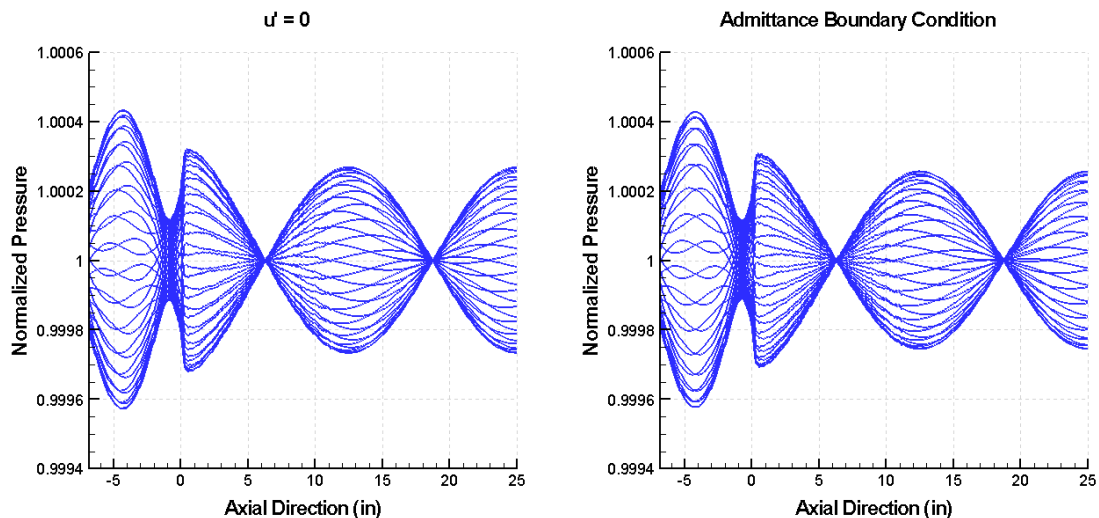


Figure 5.5 Mode shape comparison between  $u' = 0$  boundary condition and the admittance boundary condition for small amplitude forcing.

High amplitude, single frequency forcing was also done with the nozzle admittance condition applied. An FFT comparison between the full nozzle

configuration,  $u' = 0$  boundary condition, and nozzle admittance condition at position 2 is shown in Figure 5.6.

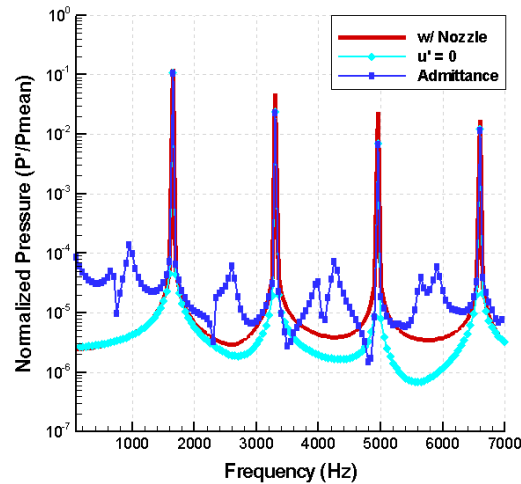


Figure 5.6: Comparison of nozzle configuration,  $u' = 0$  boundary condition, and nozzle admittance condition for an FFT performed at position 2 with high amplitude forcing at 1650 Hz and a 25 inch chamber length

In Figure 5.6, the admittance condition matches very closely with the  $u' = 0$  boundary condition at the resonance frequencies. However, at the off-resonance frequencies, the admittance condition appears to excite various modes in the chamber that are not excited by either the nozzle configuration or the  $u' = 0$  boundary condition. Because there is such a large difference between the nozzle configuration solution and the approximate boundary condition solutions, it appears that approximate boundary conditions introduce large errors when high amplitude forcing is applied. As discussed in CHAPTER 4, large amplitude forcing introduces steep-fronted waves and higher harmonics at shorter wavelengths, which cause the quasi-steady assumption to lose validity. Therefore, these approximate boundary conditions should not be relied upon to give accurate solutions when the flow oscillations are sufficiently high to exhibit non-linear behavior.

### 5.3. Upstream Boundary Condition and Source Term

The original formulation of the computational model applied an inflow boundary condition at the upstream boundary. An inflow boundary corresponds to an open boundary where the waves are free to propagate out of the domain. However, this is fundamentally different than the upstream condition in the experiment. In the experimental setup, the upstream boundary was a wall and the oxidizer was introduced at the mid-point of the injector. A wall boundary corresponds to a closed boundary, where the waves cannot propagate outside of the domain but are reflected. This was done so that the longitudinal pressure perturbations would reflect as much as possible from the upstream end, thereby decreasing the damping in the system and encouraging instability in the injector and chamber. To predict combustion instability accurately, it is important to match the experimental upstream boundary.

#### 5.3.1. Upstream Wall Boundary Condition

At a hard wall boundary, the flow velocity normal to the wall is zero. This boundary condition (and its implementation) is analogous to the  $u' = 0$  boundary condition discussed in Section 5.2.1, except that the velocity is held constant at zero instead of some flow-dependent velocity.

Because the computational model is one-dimensional, boundaries are only applied at the upstream and downstream ends of the domain. Since the upstream boundary is now a hard wall, the flow can no longer originate from this boundary. The only option for introducing flow into the domain (without going to multiple dimensions) is to add a source term at some point in the domain. The method chosen for doing this is outlined in Section 5.3.2.

### 5.3.2. Oxidizer Mass Flow Source Formulation

The oxidizer source term is added at the same location in the computational domain as in the experimental setup (3.4 inches from the injector head end). To preclude the oxidizer source from appearing as a discontinuity, a smoothly varying Gaussian normal distribution is employed.<sup>42</sup> The normal distribution is a probability density function and was chosen because of its simplicity. The general form is,

$$N_d(x; \mu, \sigma) = \frac{1}{\sigma\sqrt{2\pi}} \exp\left(-\frac{(x - \mu)^2}{2\sigma^2}\right) \quad \text{Eq. 5.2}$$

where  $\mu$  is the mean,  $\sigma$  is the standard deviation, and  $x$  is the axial coordinate.

The  $\mu$  and  $\sigma$  parameters in Equation 5.2 can be chosen to best match the experiment. The mean was chosen as 3.40 inches and the standard deviation was chosen as 0.964 inches so that about 99.9% of the area under the distribution is within the injector region. With this source term employed, the oxidizer flow-rate in the injector increases with the axial coordinate, with the oxidizer addition reaching completion before the injector/chamber interface. A schematic of this setup, with the wall boundary and oxidizer source labeled, is shown in Figure 5.7.

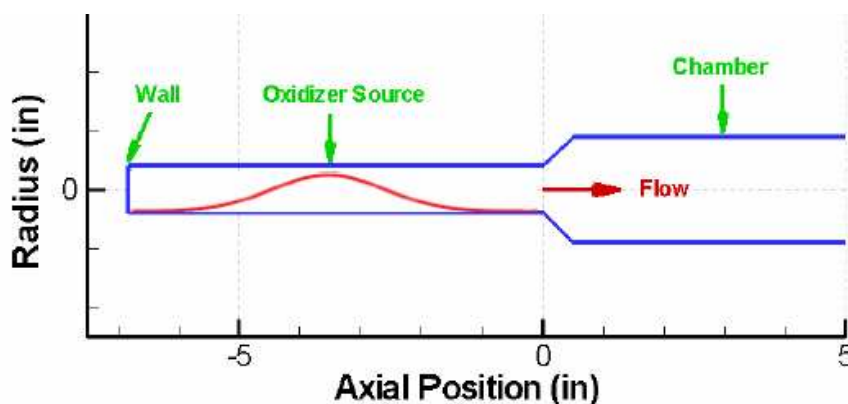


Figure 5.7: Schematic of the computational domain, showing the upstream wall boundary, the oxidizer source, and part of the chamber (the nozzle is not shown). The oxidizer source distribution is shown inside the injector for  $\sigma = 0.964$  inches.

The equations of motion employed in the code were defined in Section 2.1. The oxidizer mass flow source is added to the right-hand-side of the governing equations as a vector, just like the steady combustion source (see Section 2.2. Defining the oxidizer source in the same way as the steady combustions source,

$$H = \begin{pmatrix} \bar{\dot{\omega}}_{ox} N_d \\ \bar{\dot{\omega}}_{ox} N_d \bar{u} \\ \bar{\dot{\omega}}_{ox} N_d \bar{h}_0 \\ \bar{\dot{\omega}}_{ox} N_d Y_{ox} \end{pmatrix} = \begin{pmatrix} \bar{\dot{\omega}}_{ox} N_d \\ \bar{\dot{\omega}}_{ox} N_d \bar{u} \\ \bar{\dot{\omega}}_{ox} N_d \left( c_p \bar{T} + h_f^0 + \frac{\bar{u}^2}{2} \right) \\ \bar{\dot{\omega}}_{ox} N_d Y_{ox} \end{pmatrix} \quad \text{Eq. 5.3}$$

where  $h_f^0$  is the heat of formation,  $Y_{ox}$  is the oxidizer mass fraction, and  $\dot{\omega}_{ox}$  is the rate at which oxidizer is introduced into the flow in terms of a mass flux ( $\text{kg/m}^2\text{s}$ ).<sup>43</sup> An over-bar designates a mean quantity.

Since only oxidizer is present in the injector region,  $Y_{ox}$  equals one. The  $\dot{\omega}_{ox}$  term is obtained by integrating over the volume of the injector and equating this to the mean mass flow-rate. This derivation is shown in Equation 5.4.

$$\begin{aligned} \bar{\rho} \bar{u} \bar{A} &= \int \bar{\dot{\omega}}_{ox} (N_d) dV \\ \bar{\rho} \bar{u} \bar{A} &= \bar{\dot{\omega}}_{ox} \int (N_d) \bar{A} dx \\ \bar{\rho} \bar{u} \bar{A} &= \bar{\dot{\omega}}_{ox} \bar{A} \int (N_d) dx \\ \bar{\rho} \bar{u} &= \bar{\dot{\omega}}_{ox} \int (N_d) dx \\ \bar{\rho} \bar{u} &= \bar{\dot{\omega}}_{ox} \end{aligned} \quad \text{Eq. 5.4}$$

where  $N_d$  represents the normal distribution from Equation 5.2.

The  $\dot{\omega}_{ox}$  term is constant, and so can be taken out of the integral, as shown in the second line of Equation 5.4. The area of the injector region is also constant, and cancels with the mass flow-rate area when taken outside of the integral (4<sup>th</sup> line). The last step is possible because the integral of a probability

density function (the area under the curve) is equal to one. The final result of Equation 5.4 is that the  $\dot{\omega}_{ox}$  term is simply equal to the injector mean density times the injector mean velocity. For the conditions given in Table 2-1 and Table 2-3 (and using the ideal gas equation of state to find the injector mean density), the  $\dot{\omega}_{ox}$  term is equal to  $1415 \text{ kg/m}^2\text{s}$ .

In the experimental configuration, the oxidizer was injected radially into the injector. This caused the oxidizer to have no initial axial momentum. This can be modeled in the source term by making the second term ( $\dot{\omega}_{ox}u$ ) exactly equal to zero. All of the momentum in the injector comes from the mass flow-rate and the pressure.

### 5.3.3. Upstream Boundary Solution Comparisons

The steady-state solutions for the wall boundary condition (with the oxidizer source included) are compared to the inflow boundary condition solutions in Figure 5.9 - Figure 5.11. The axial geometry and output locations have been repeated in Figure 5.8 for orientation in interpreting the steady-state solutions.

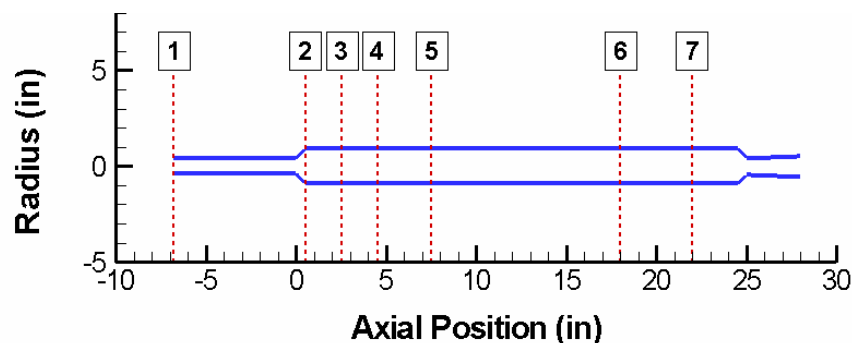


Figure 5.8: Axial geometry and output locations of the computational domain

In Figure 5.9 - Figure 5.11, the left figure shows the entire computational domain while the right figure shows a close-up view of the solution in the injector.

The left figures show that the steady-state solutions are interchangeable in the chamber and nozzle regions from the inflow boundary results. Different values for the standard deviation of the oxidizer source are also included to show the range of possible solutions with the wall boundary/oxidizer source configuration.

Figure 5.9 shows the steady-state velocity solutions. In the injector region (axial coordinate less than zero), the inflow boundary solution shows a constant velocity of 255 m/s. For the wall boundary solutions, the velocity starts at zero and increases until it has reached 255 m/s. The slope at which the velocity increase occurs is dependent on the standard deviation of the oxidizer source. For a standard deviation of 0.394 inches, the increase happens very rapidly in the center of the injector (green). For a standard deviation of 0.964 inches, the increase occurs over a longer axial distance (red).

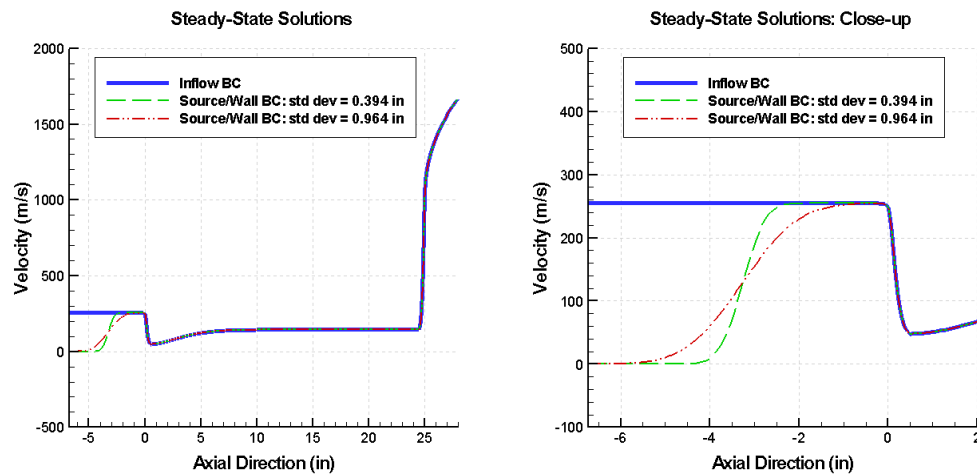


Figure 5.9: Steady-state velocity solutions (full domain and close-up) for an inflow boundary condition and for the oxidizer source/wall boundary configuration

Comparisons of the steady-state pressure solutions are shown in Figure 5.10 for the same oxidizer source and boundary condition parameters as the previous velocity solutions.

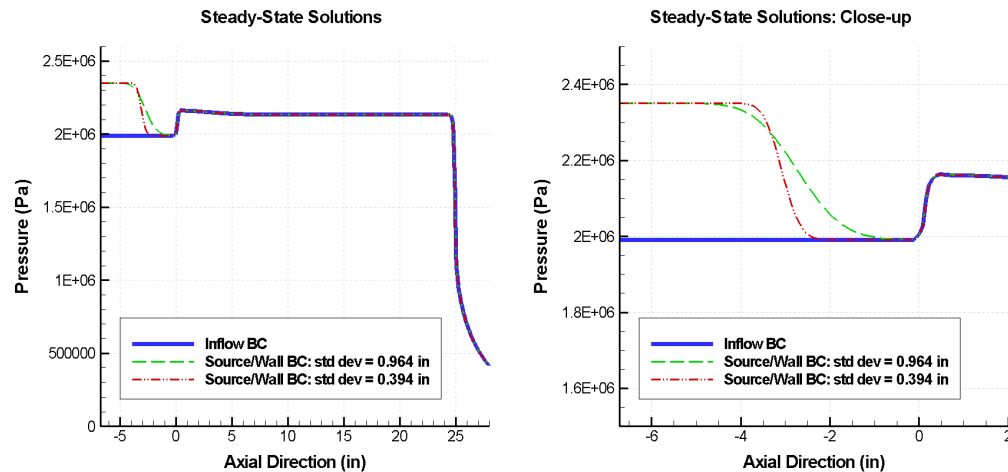


Figure 5.10: Steady-state pressure solutions (full domain and close-up) for an inflow boundary condition and for the oxidizer source/wall boundary configuration

The pressure in the chamber and nozzle are identical for the inflow and wall boundary configurations. For the wall boundary solution, the pressure in the injector can be seen to drop from a stagnation condition at the wall boundary to its static pressure before entering the chamber. The slope at which the pressure decrease occurs is again dependent on the standard deviation of the oxidizer source.

The steady-state temperature solutions are compared in Figure 5.11 for an inflow boundary and a wall boundary with a source standard deviation of 0.964 inches. As with the previous steady-state solutions, the chamber and nozzle solutions are exactly the same for the steady-state temperature. Although not shown, this same result has been verified for all of the flow parameters, such as mass-flow rate, density, etc. In the injector region, the temperature falls from 970 K to 952 K. This corresponds to the transition from stagnation temperature to static temperature as the velocity of the flow increases through the injector.



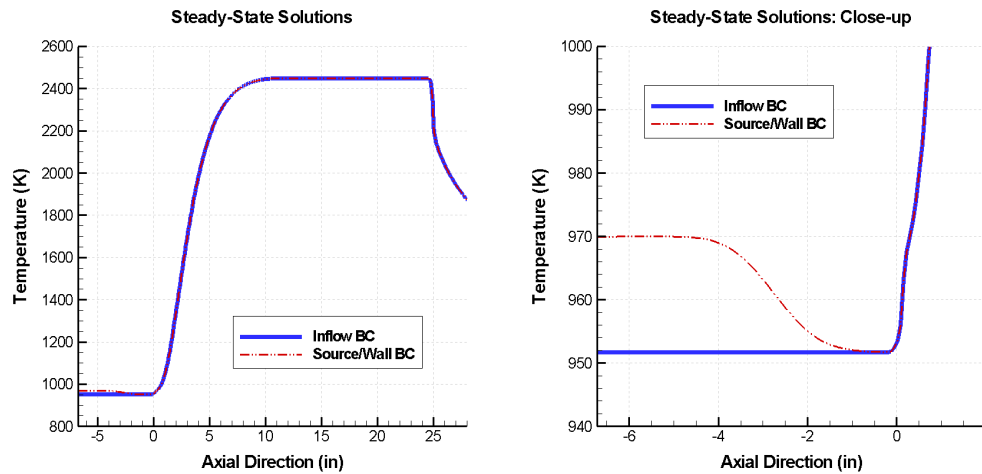


Figure 5.11: Steady-state temperature solutions (full domain and close-up) for an inflow boundary condition and for the oxidizer source/wall boundary configuration

Unsteady solutions were also obtained for the wall boundary/oxidizer source configuration. These include FFT plots of broadband, small amplitude forcing and small amplitude mode shapes. The broadband FFT plot for a 25 inch chamber is shown in Figure 5.12 for positions one, two, and five (see Figure 5.8). FFT plots for all of the chamber lengths (along with tables comparing the mode frequencies at all output locations) can be found in Appendix B.

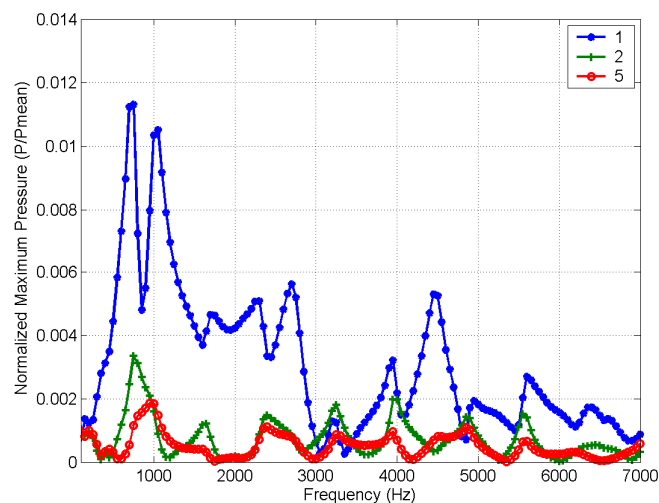


Figure 5.12: FFT plot of the 25 inch chamber case with broadband small amplitude forcing and the wall boundary/oxidizer source applied

The above plot indicates similar modes as those obtained in Section 3.3, although some of the modes have been shifted in frequency from the inflow boundary condition result. The amplitude of the response at position one also seems to be lower at higher frequencies, which was not observed in the inflow boundary results.

Two representative mode shape comparisons (at 750 Hz and 1650 Hz) are shown in Figure 5.13 and Figure 5.14. The other mode shapes follow similar trends.

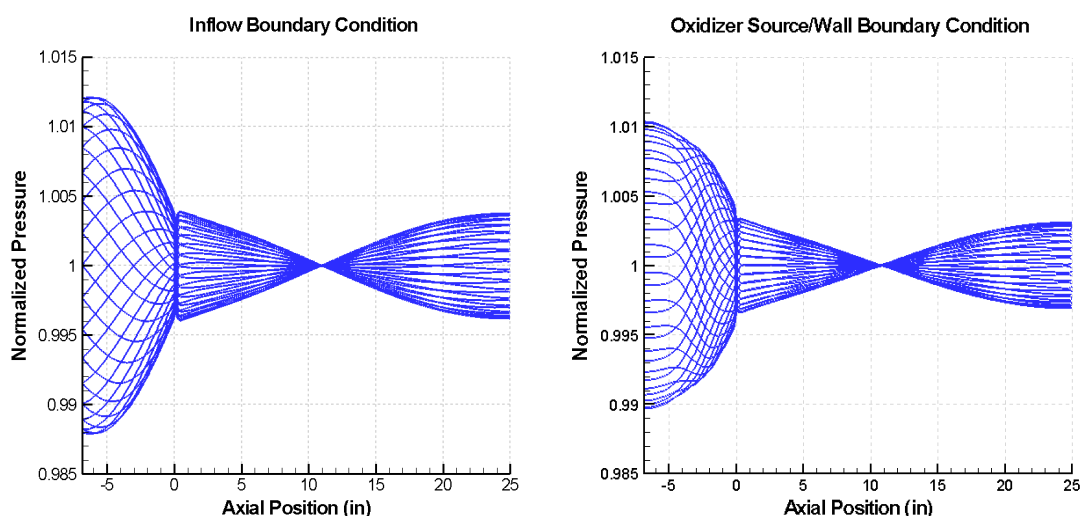


Figure 5.13: Pressure mode shape comparison between the inflow boundary condition and the wall BC/source for small amplitude forcing at 750 Hz

In Figure 5.13, the wall boundary mode shape (right) appears very similar to the inflow boundary mode shape (left), especially in the chamber region. The phase differences in the injector region can be explained by the change in the injector Mach number. For the inflow boundary condition, the steady-state solution is at a constant mach number of 0.38. Because the chamber is only at a Mach number of 0.13, there is a phase shift between the chamber mode shape and the injector mode shape, as discussed in Section 3.3.1. For the wall boundary/source solution, there is also a Mach number change in the injector

itself as the Mach number increases from zero to 0.38. This transition is shown by a phase shift in the injector region of the wall boundary/source mode shape.

The wall boundary also forces the mode shape to have an exact pressure anti-node at the injector head-end. However, since the inflow mode shape is already very close to a pressure anti-node at the injector head-end, there is only a slight change in the mode shape envelope between the two boundary conditions.

For small amplitude forcing at 1650 Hz, a large difference in the mode shapes can be seen between the two boundary conditions, as shown in Figure 5.14.

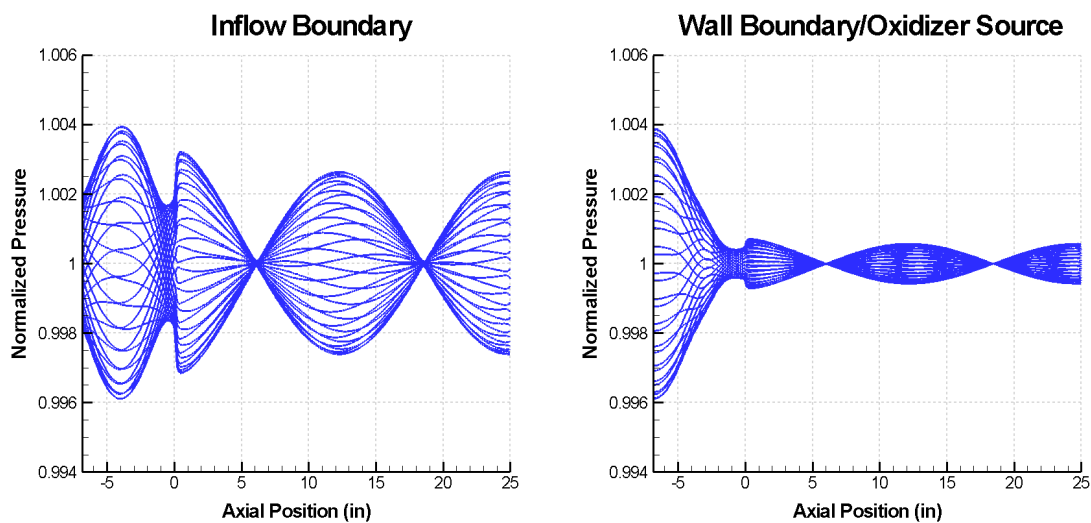


Figure 5.14: Pressure mode shape comparison between the inflow boundary condition and the wall BC/source for small amplitude forcing at 1650 Hz

The relative amplitudes between the injector and chamber have changed dramatically from the inflow boundary result to the wall boundary result. For the inflow boundary mode shape, the injector and chamber amplitudes are roughly the same. For the wall boundary mode shape, the injector amplitude is much larger than the chamber amplitude. The phase and shapes of the modes in the injector region are also very different between the two mode shapes. The change in phase in the injector is due to the Mach number transition from zero to 0.38,

just like the 750 Hz mode shape. The change in the mode shape envelope can be explained by the wall boundary condition. For the inflow boundary condition, the mode shape appears to be close to a pressure node at the injector head-end. The wall boundary forces the mode shape to have a pressure anti-node at the injector head-end, which causes the mode shape to change dramatically. The mode in the injector appears more like a half-mode for the wall boundary solution.

For those inflow mode shapes that are already close to having a pressure anti-node at the injector head-end, most of the change in the wall boundary solution will be in the phase difference (due to the transition in the injector from a low Mach number to a high Mach number). This should not impact the mode shape envelope significantly. If the inflow mode shape does not already approximate an anti-node at the injector head-end, the wall boundary will force a pressure anti-node there. This will cause changes in both the phase and the mode shape envelope.

The wall boundary/oxidizer source condition was also forced with high amplitude forcing at 50% and 1650 Hz. The PSD results are shown in Figure 5.15.

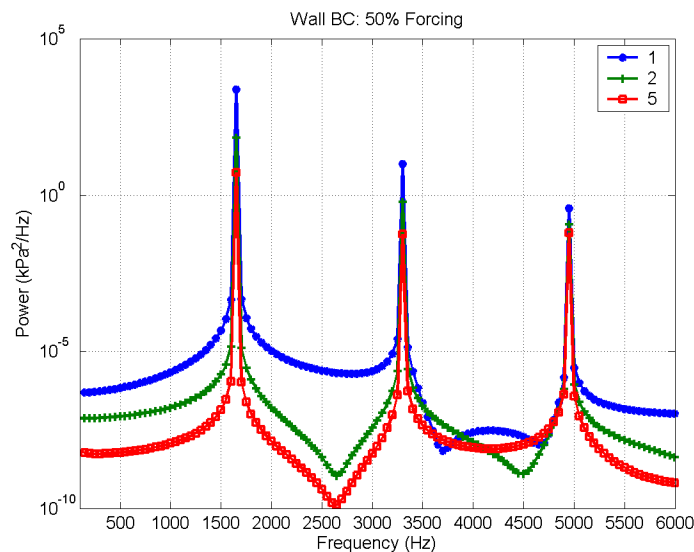


Figure 5.15: PSD plot of high amplitude (50%) forcing at 1650 Hz with a 25 inch chamber length

Figure 5.15 appears similar to the results of Section 4.1, with a high peak at the forced frequency and decreasing harmonics appearing at higher frequencies. The results also have relatively narrow peaks and do not excite any other off-resonance modes. The amplitudes are slightly different from the inflow boundary in that now the highest response occurs at the injector head-end instead of the injector/chamber interface. As shown by the mode shapes in Figure 5.14, this result occurs because a pressure anti-node is being forced at the injector head-end due to the wall boundary. Overall, the change to a wall boundary condition (and the addition of an oxidizer source) does not appear to significantly alter the non-linear behavior of the response.

The change from an inflow boundary to a wall boundary with an oxidizer source has had an impact on the steady-state solutions, the small amplitude modes, and the non-linear response. The steady-state wall boundary solutions appear reasonable and seem to qualitatively match the experimental configuration better than the inflow boundary. The small amplitude wall boundary results indicate that while the frequencies have changed only slightly from the inflow boundary modes, the mode shapes may be dramatically different for certain modes. The wall boundary (and oxidizer source) may cause changes in both the injector phase and the mode shape envelope. This includes changes in the relative injector/chamber amplitudes and in the actual injector envelope shape. This was especially apparent for the 1650 Hz wall boundary mode shape, where a relatively large pressure anti-node formed at the injector head-end. The large amplitude wall boundary results show the same qualitative behavior as the inflow boundary results, although the amplitudes at certain positions have changed. In accordance with the mode shape results, the 1650 Hz result showed larger amplitudes at the injector head-end position in relation to the other chamber positions.

## CHAPTER 6. INSTABILITY STUDIES USING RESPONSE FUNCTIONS

The previous chapters have concentrated on matching the linear and non-linear acoustic response of the experimental results by oscillating the inlet mass-flow rate at small and large amplitudes. The combustion has been approximated using a steady-state heat release model, which does not capture its dynamic nature. Because combustion instability is produced by a coupling between the oscillating pressure and heat release, it is necessary to model the dynamic heat release in order to simulate instability.

The computational model that is currently being used is only formulated for one-dimensional analysis, so complex two or three-dimensional flow dynamics cannot be captured. Response functions (see Section 1.1.4) must be formulated which relate the heat release to one of the flow conditions. Section 6.1 will show a simple response function for dynamic heat release and Section 6.2 will examine how to implement this into the computational model. Section 6.3 will examine the results using different boundary conditions and Section 6.4 will compare these results to the experiment data.

### 6.1. Simplified Response Function

As discussed in Section 1.1.1, Rayleigh's criterion states that when positive (negative) heat release is in phase with positive (negative) pressure oscillations, the pressure oscillations will be amplified. The pressure oscillations will decrease if the heat release is negative (positive) when the pressure oscillation is positive (negative). Then, the phase relationship between the

pressure and heat release plays a very important role in determining whether instability will even occur.

The amount of pressure amplification is also very important because this will determine whether the pressure oscillation decays or grows. Even if the pressure and heat release are perfectly in-phase, the pressure oscillation will decay if the pressure amplification is smaller than the amount of damping in the system. Damping may occur due to the escape of dynamic pressure energy out of the nozzle or inlet. If the pressure amplification is greater than the amount of damping, the part of the dynamic pressure that has not escaped will feed back into the pressure oscillation, causing growth of the pressure oscillation. This growth will continue until non-linear limit cycle behavior occurs.

Because phase and amplitude are controlling factors of combustion instability, the heat release response functions are often defined using these parameters. Two forms of response functions are shown below, one which relates the heat release with pressure, the other which relates heat release with velocity.

$$q'''(x, t) = \alpha p'(x, t - \tau) \quad \text{Eq. 6.1}$$

$$q'''(x, t) = \alpha u'(x, t - \tau) \quad \text{Eq. 6.2}$$

The  $\tau$  parameter controls the phase relationship, while the  $\alpha$  parameter controls the amplitude of the response. If  $\tau$  creates a condition where the response is sufficiently in-phase with the heat release and  $\alpha$  is large enough to overcome damping in the system, the heat release will grow and combustion instability will result.

Although pressure and heat release coupling is necessary for instability, the heat release itself may be controlled by any of the complex flow dynamics occurring in the system. For example, the dynamic heat release may be greatly affected by vortex shedding.<sup>32-35</sup> This occurs when a vortex is shed near the injector/chamber interface and then moves downstream until it comes in contact

with a wall or another vortex. When interaction occurs between a wall or another vortex, rapid turbulent mixing takes place which causes combustion and heat release. The heat release (or a part of it), is controlled by the phase at which the vortexes sheds. Equation 6.2 refers to this type of situation, where the velocity perturbation is controlling the heat release response. Some of the flow mechanisms that influence heat release were discussed briefly in Section 1.1.4.

## 6.2. Formulation of a Simple Heat Release Source

The response functions discussed in the previous section can be simplified further if it is assumed that the heat release and pressure are exactly in phase. For this to be true, the  $\tau$  parameter from Equations 6.1 and 6.2 must be equal to zero. In accordance with Rayleigh's criterion, this defines the phase condition when combustion instability is most likely to occur. Under this condition, the occurrence of combustion instability becomes solely a function of the amplitude of the response function. For simplicity, it is assumed that the heat release is a function of the pressure oscillation. Then Equation 6.1 simplifies to the following,

$$q'''(x, t) = \alpha p'(x, t) \quad \text{Eq. 6.3}$$

This can be implemented in the computational model by including Equation 6.3 in the energy equation of the source term that was defined in CHAPTER 2. For coding purposes, the oscillating pressure ( $p'$ ) can be defined as the difference between the instantaneous pressure and the mean pressure. Since the steady-state solution was obtained prior to running the unsteady code, the mean pressure is already known and can be entered as an input. Then Equation 6.3 becomes,

$$q'''(x, t) = \alpha(x, \beta, \mu, \sigma) * (p(x, t) - p_{\text{mean}}(x)) \quad \text{Eq. 6.4}$$



The  $\alpha$  parameter in Equation 6.4 is defined as constant in time but varying in space. The spatial variation allows the  $\alpha$  parameter to be introduced gradually so that a discontinuity does not occur in the code. Similar to the formulation of the oxidizer source in Section 5.3.2, a normal distribution (with a mean parameter,  $\mu$  and a standard deviation,  $\sigma$ ) is used to define  $\alpha$ . The  $\beta$  parameter is the actual constant input for  $\alpha$ . The spatial integration of  $\alpha$  over the entire domain will then be equal to  $\beta$ . The  $\alpha$  term is defined as,

$$\alpha(x, \beta, \mu, \sigma) = \frac{\beta}{\sigma\sqrt{2\pi}} \exp\left(-\frac{(x - \mu)^2}{2\sigma^2}\right) \quad \text{Eq. 6.5}$$

The mean and standard deviation were set in accordance with the physical conditions of the system. Assuming that most of the combustion occurs near the injector/chamber interface,  $\mu$  was set at the axial position corresponding to the interface. Also, it was assumed that the distribution of this heat release was relatively narrow, so that the standard deviation is small. A schematic of the heat release envelope is shown in Figure 6.1. Note that the heat release envelope includes both positive and negative normal distributions, representing the oscillations of the unsteady heat release.

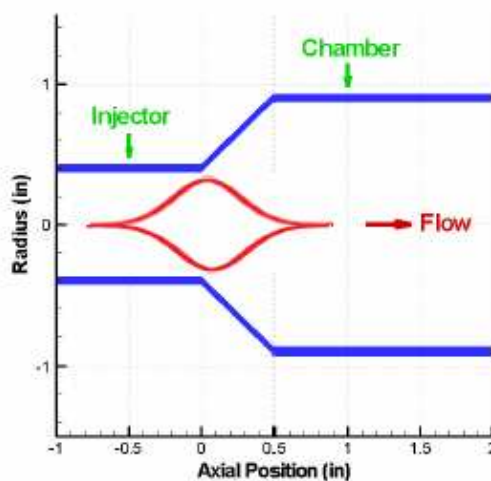


Figure 6.1: Schematic showing the heat release envelope at the injector/chamber interface. Note that the envelope shows both positive and negative heat release.

For most of the chamber length cases, the mode shapes at the unstable frequencies show a pressure anti-node close to the injector/chamber interface (see Figure 3.42). By defining a narrow heat release source near the interface, instability in the system should be promoted since the pressure oscillation is near its highest value.

In order to use Equation 6.4, some kind of initial perturbation in the pressure is necessary so that the heat release term is not identically zero (which would occur if the instantaneous pressure was exactly equal to the mean pressure). This perturbation is accomplished by oscillating the mass-flow with small amplitude forcing, as was done in CHAPTER 3. This causes the initial perturbation to be linear. The results in the following sections were obtained by first running the small amplitude perturbation to a converged condition (no growth or decay) while  $\alpha$  was input as zero. The mass-flow perturbation is then changed to zero and  $\beta$  is simultaneously set to some non-zero value. The response can then grow or decay, depending on the relative size of the amplitude of  $\beta$  and the amount of damping in the system.

### 6.3. Application of the Response Function

The response function formulation from the previous section is now employed for two different boundary conditions. In Section 6.3.1 the response function is applied with an inflow boundary condition, which was used to obtain the results of CHAPTER 3 and CHAPTER 4. In Section 6.3.2 the response function is applied with an injector head-end wall boundary, which was developed in CHAPTER 5. The wall boundary condition results are then compared with the experimental data in Section 6.4. For all of these results, the code was first run to a converged condition (constant maximum and minimum fluctuations) using small amplitude mass flow forcing. The mass flow oscillation was then turned off and the heat release response function was applied.

### 6.3.1. Initial Trials with an Inflow Boundary

For these initial trials, the response function mean amplitude ( $\mu$ ) is placed at the injector/chamber interface. The standard deviation is set at 0.394 inches. This means that within 1.5 inches in either direction, more than 99.9% of the heat release source has been applied. All of the trials are for a chamber length of 25 inches and are output near the injector/chamber interface (position 2). The only parameter that is varied is the  $\beta$  parameter, which controls  $\alpha$  and the heat release.

It is first necessary to confirm that the response function responds as predicted. This was done by running single frequency, small amplitude forcing (1% of the mean mass flow-rate) to a converged condition (constant maximum and minimum fluctuations). The experimental unstable frequency of 1650 Hz was used for the forcing. At about 0.06 seconds, the mass-flow forcing was set to zero and a  $\beta$  value of 2250 was applied. Growth and a non-linear limit cycle developed due to the response function. At about 0.12 seconds, the  $\beta$  value was set to zero and the pressure oscillation decayed. By 0.14 seconds, the pressure oscillation had decayed to zero. This pressure response is shown in Figure 6.2.

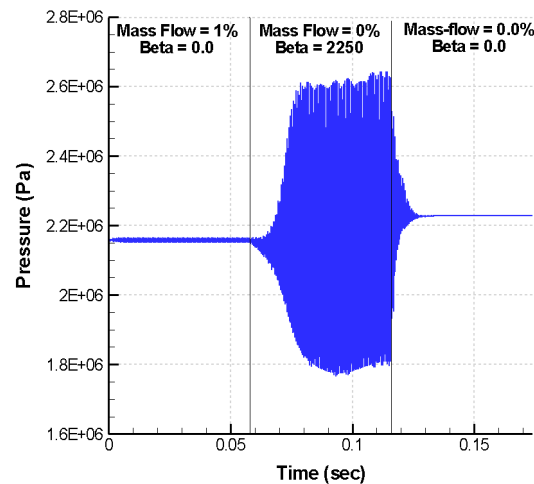


Figure 6.2: Pressure history plot for an inflow boundary with small amplitude mass-flow forcing (first region), a response function applied (second region), and neither mass-flow forcing nor the response function applied (third region)

There is rapid decay in the third region because both the mass flow forcing and the response function amplitude have been set to zero. In the absence of damping, the pressure should continue to oscillate due to the reflection and feedback of pressure oscillations. However, damping is present in the system due to acoustic and particle waves traveling outside of the domain through the nozzle ( $u$  and  $u+c$  waves) and the inflow boundary ( $u-c$  waves). The response function appears to produce the expected results.

By running various values of  $\beta$ , it was confirmed that the pressure response would decay or grow depending on the size of  $\beta$ . These two cases are shown in Figure 6.3 for  $\beta$  values of 100 (left) and 2250 (right). As with Figure 6.2, the initial converged region was obtained by first forcing at 1650 Hz with 1% mass flow forcing.

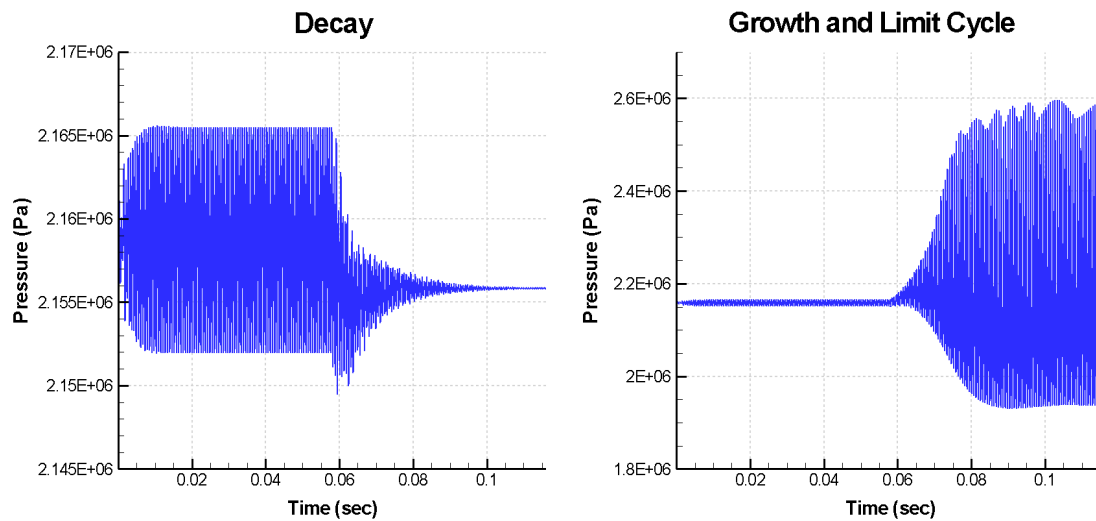


Figure 6.3: Pressure history plots for  $\beta = 100$  (left) showing decay, and  $\beta = 2000$  (right) showing growth and limit cycle behavior

When the input was large enough to cause growth, the pressure response either grew to a limit cycle or began to diverge. When divergence occurred, the code terminated abruptly and limit cycle behavior was not able to develop. With the inflow boundary condition applied, the maximum allowable  $\beta$  value was found

to be 2350. Above this value, divergence occurs. This divergence is believed to be numerical in nature and represents the limit at which the computational model will give physically realistic results. Since the limit cycle that is obtained for the possible values of  $\beta$  is still highly non-linear, the computational model should be able to match the experimental data qualitatively. The computational results may be quantitatively smaller than the experimental data due to the limit imposed by numerical divergence.

### 6.3.2. Results with an Injector Head-end Wall Boundary

An injector head-end wall boundary condition was developed in CHAPTER 5 and is believed to better represent the conditions of the experiment. Because of the different damping characteristics between an inflow boundary (which allows acoustic waves to leave the domain) and a wall boundary (which reflects acoustic waves), it is also believed that the upstream boundary condition may have an impact on the stability of the system. As was shown in the previous section, damping determined when decay or growth occurred and thus was a large factor in determining instability. More detailed analysis of the heat release response function is now done with the wall boundary condition applied so that the computational model can approximate the experimental setup as closely as possible.

As was done in the previous section, the beta values necessary for decay, growth, and divergence were found. Representative plots for each are shown in Figure 6.4. The initial 'converged' region was obtained by forcing at 1650 Hz and 1% of the mass flow-rate.

The transition between decay and growth occurs at a  $\beta$  value of about 1500. Divergence (and termination) of the code occurs at a  $\beta$  value of 2110, and the maximum allowable  $\beta$  value is found to be 2100. Just like the results of the previous section, the instability of the system for an upstream wall boundary is directly dependent on the magnitude of  $\beta$ .

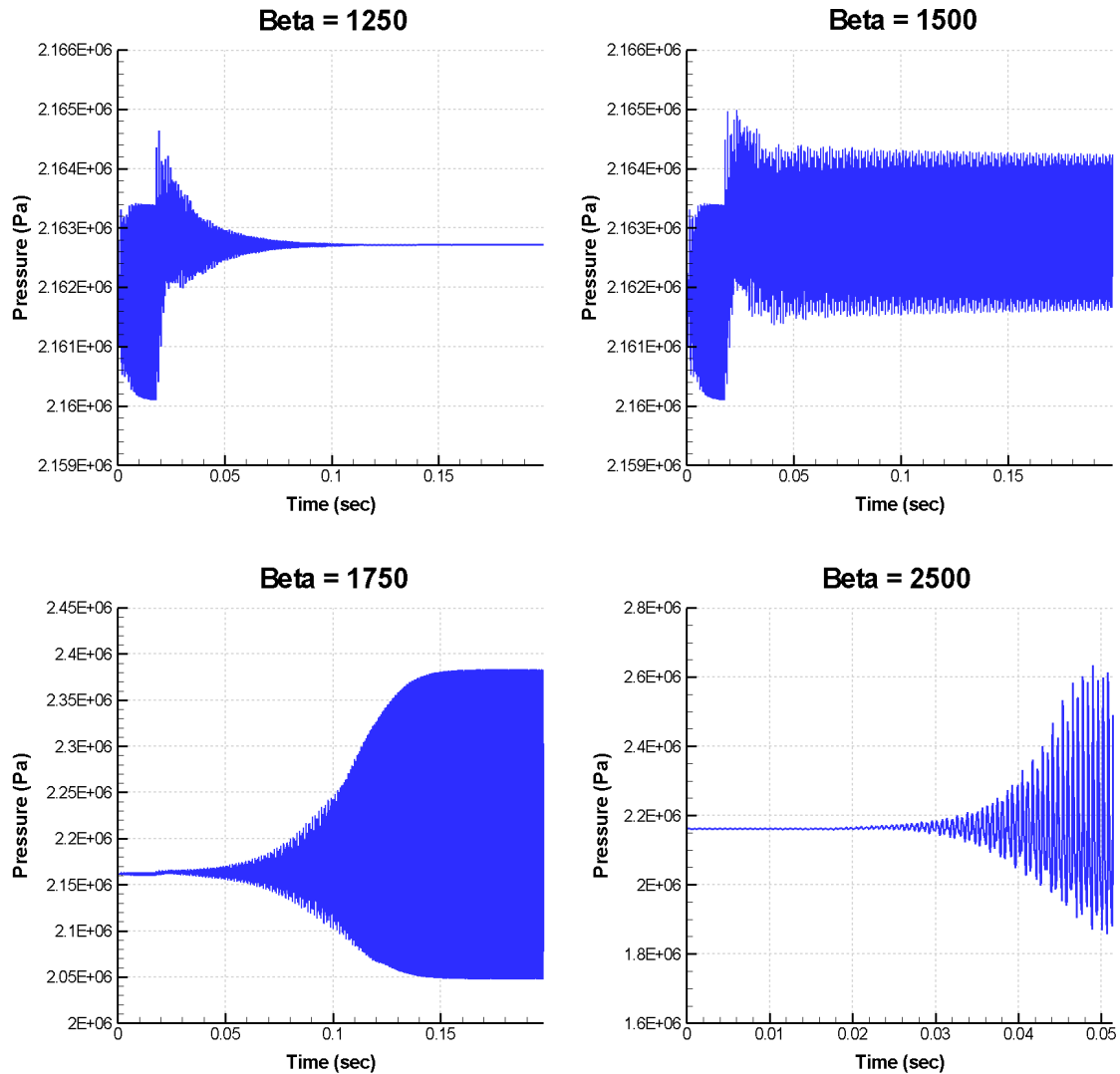


Figure 6.4: Variation of beta values for an upstream wall boundary condition, resulting in 1) decay, 2) 'converged' conditions, 3) growth and limit cycle, 4) numerical divergence

The results in Figure 6.2 - 6.3 were obtained by first forcing the code at 1650 Hz with 1% mass flow forcing. Broadband forcing at 0.01% mass flow forcing is now applied to simulate initial noise. As with the previous analysis, once this has reached a converged condition the mass flow forcing will be turned off and the response function will be turned on. Unlike the previous single frequency forced results, the code can now go unstable at any acoustic mode, or

even multiple modes. The response function was applied to a 25 inch chamber after the initial small amplitude broadband forced oscillation was established. The broadband mass flow forcing was set to zero at about 0.1 seconds, at which point a  $\beta$  value of 2050 was applied. The result is shown in Figure 6.5. The growth and limit cycle appear similar to the previous plots.

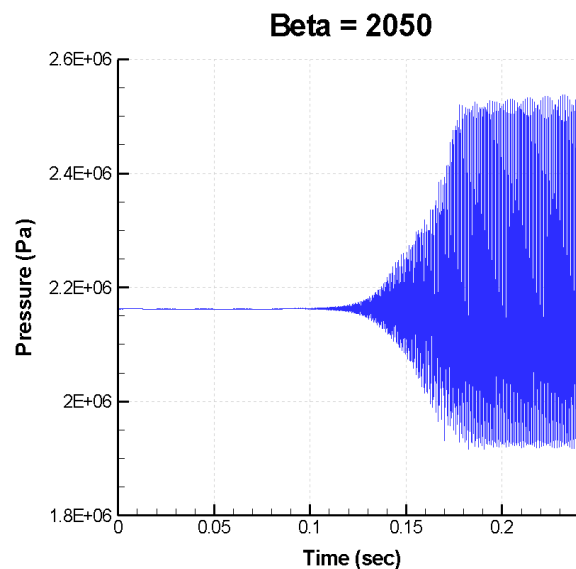


Figure 6.5: Growth and limit cycle due to the application of the response function. The chamber length is 25 inches,  $\beta = 2050$ , and broadband forcing was used to simulate the initial noise.

The frequency response of the limit cycle can be determined with a power spectral density (PSD) plot. The PSD plot is shown in Figure 6.6. The highest peak occurs at 1650 Hz, corresponding to the experimental unstable frequency. The next two highest peaks are at 3250 Hz and 4900 Hz, corresponding to the first two higher harmonics of the unstable frequency. Other, lower amplitude, modes can also be seen. The first small peak occurs at 750 Hz, which is the first chamber mode. Not all of the low amplitude peaks correspond to previously identified acoustic modes.

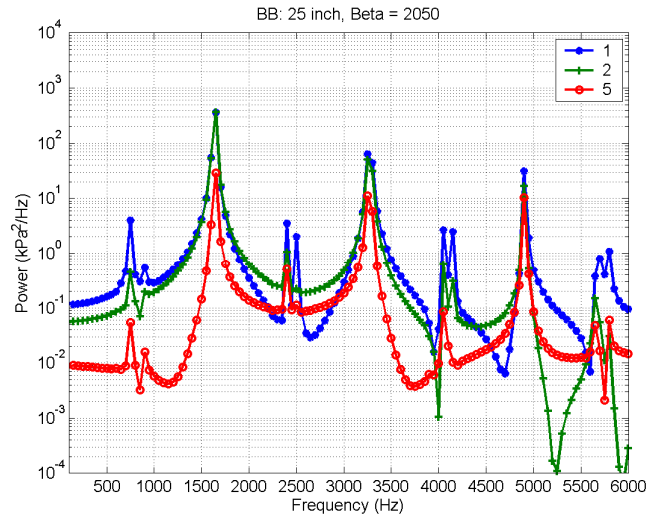


Figure 6.6: PSD plot of the limit cycle region in Figure 6.5 for positions 1, 2, and 5

By performing PSD analysis at various times along the pressure trace of Figure 6.5, better understanding can be gained of how the instability developed. These time slices are identified in Figure 6.7 by vertical red lines and correspond to times of 0.084, 0.14, 0.16, 0.18, and 0.24 seconds.

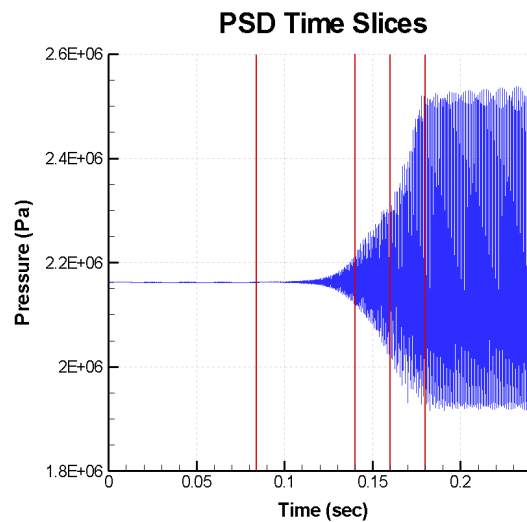


Figure 6.7: Time slices taken during the small amplitude forcing (0.084 seconds), the growth region (0.14 and 0.16 seconds), and the limit cycle region (0.18 and 0.24 seconds) for PSD analysis



A frequency analysis is first done at a time of 0.084 seconds. This is the small amplitude, broadband forced region (simulated noise). A similar FFT plot was examined in detail in Section 5.3.3. The plot is now done using PSD analysis and has been plotted on a log scale. This is shown in Figure 6.8. As expected, it shows a small amplitude response with all of the acoustic modes represented.

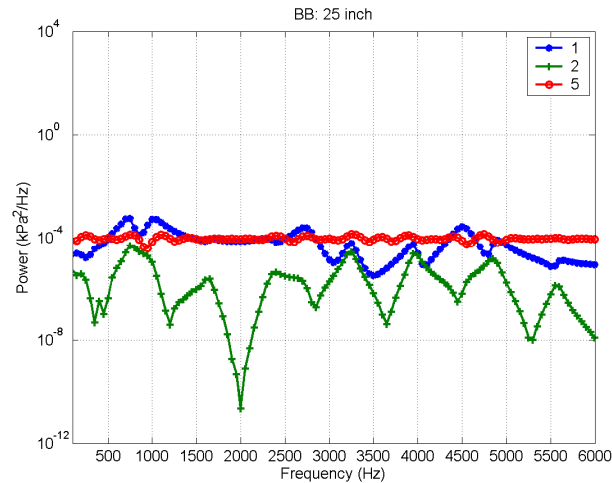


Figure 6.8: PSD plot at 0.084 seconds in the noise region of the pressure trace of Figure 6.5 for positions 1, 2, and 5

A frequency analysis is then done at a time of 0.14 seconds in the pressure trace of Figure 6.5. This is relatively early in the growth region. The PSD result is shown in Figure 6.9. At 0.14 seconds, many modes can be identified in the PSD plot. The highest peak occurs at 3950 Hz. The next highest peak occurs at 1650 Hz, which is the unstable frequency in the limit cycle region. Peaks at 750 Hz, 2350 Hz and 5600 Hz can also be clearly seen. The plot appears to show linear characteristics, as no significant higher harmonics can be distinguished.

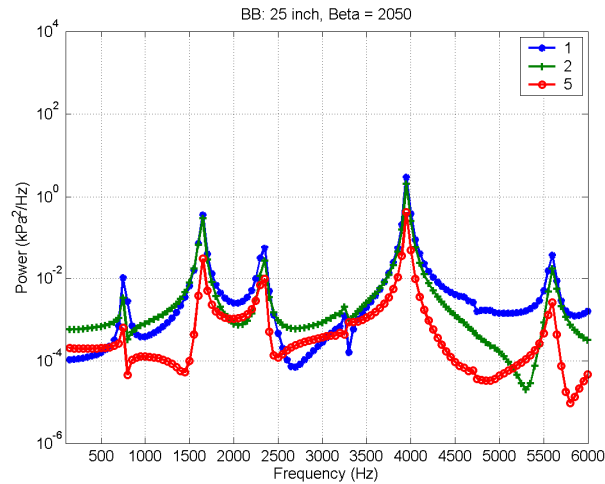


Figure 6.9: PSD plot at 0.14 seconds in the growth region of the pressure trace of Figure 6.5 for positions 1, 2, and 5

The PSD analysis is then done at 0.16 seconds. This is towards the latter part of the growth region. This result is shown in Figure 6.10.

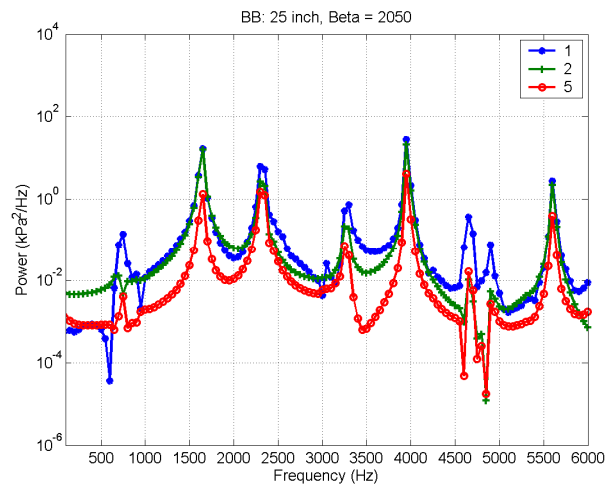


Figure 6.10: PSD plot at 0.16 seconds in the growth region of the pressure trace of Figure 6.5 for positions 1, 2, and 5

At 0.16 seconds, the amplitudes of the peaks have increased significantly. Most of the same modes from Figure 6.9 are still apparent, along with some additional ones. The response now appears to be non-linear, as higher

harmonics of the 1650 Hz mode can now be seen at 3300 Hz and 4900 Hz. A higher harmonic of the 2350 Hz mode can also be seen at 4650 Hz. Higher harmonics of the 3950 Hz and 5600 Hz modes would also be seen if the frequency analysis was extended beyond 6000 Hz. It is interesting to note that the response at 1650 Hz has increased almost two orders of magnitude over the past 0.02 seconds, while the response at 3950 Hz has only increased about one order of magnitude.

The PSD analysis is then done at 0.18 seconds, where the growth has just started to level off. This corresponds to the beginning of the limit cycle. The PSD plot at 0.18 seconds is shown in Figure 6.11.

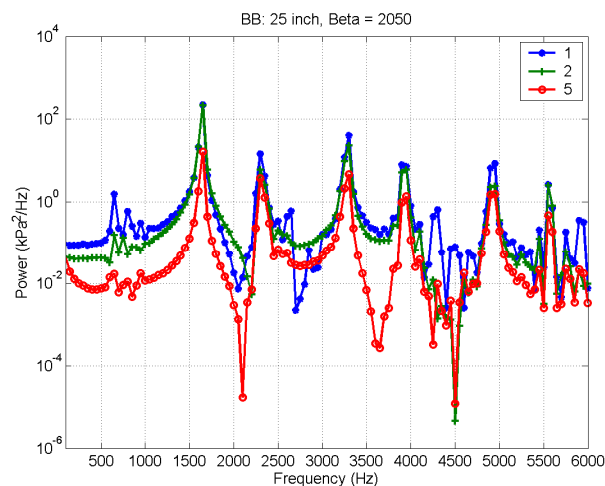


Figure 6.11: PSD plot at 0.18 seconds of the pressure trace of Figure 6.5 for positions 1, 2, and 5

At 0.18 seconds, the unstable frequency (1650 Hz) and its higher harmonics are dominating the pressure response. The amplitudes of some of the other modes are actually decreasing now, especially the peak at 3950 Hz. It is conjectured that as the unstable mode and its higher harmonics increase in amplitude, they are extracting energy from the other modes. This causes the unstable mode and its higher harmonics to grow while the other modes are decreasing as the limit cycle continues.

The results from the broadband forcing analysis are significant because they show that the computational model causes a particular acoustic mode to go unstable, just like actual spontaneous combustion instability. In this case, it was the actual unstable mode from the experiment (comparisons for all chamber lengths will be done in Section Figure 6.5). The reasons why the model caused instability at this particular mode is not entirely clear. Very complex combustion processes are occurring in the experimental configuration, which are not modeled in these one-dimensional Euler computations. Since only a simple response function is being used to simulate the complicated unsteady combustion, it is surprising that instability would occur at the same acoustic mode as the experiment. This suggests that the system acoustics (which are modeled fairly well by the computations) play a significant role in determining the mode at which instability will occur. Specifically, the acoustic mode coupling between the injector and chamber may have a major impact on determining which acoustic mode will go unstable.

A similar application of the response function was performed for the other chamber lengths (15, 20, and 35 inches). The pressure history and PSD results for these chamber lengths are shown side-by-side in Figure 6.12 - Figure 6.14. The PSD analysis was performed in the limit cycle region for each case. For the 15 inch case, a  $\beta$  value of 2000 was used because higher values caused divergence. The  $\beta$  value for the other cases is 2050.

The pressure trace and limit cycle PSD plot for the 15 inch chamber are shown in Figure 6.12. The 15 inch case shows interesting growth behavior. After the initial growth, the pressure oscillation appears to level off somewhat at about 0.14 seconds. At this point, many frequencies are apparent. At about 0.17 seconds, the pressure oscillation starts to grow rapidly again until a limit cycle is reached. The PSD for the 15 inch case shows instability at the same acoustic mode as the experiment. Higher harmonics of the unstable frequency are also visible. Note that there are no small amplitude, broadband peaks as there was with the 25 inch chamber case. It appears that the unstable frequency completely

dominates the other frequencies in the limit cycle region, causing other modes to be damped out.

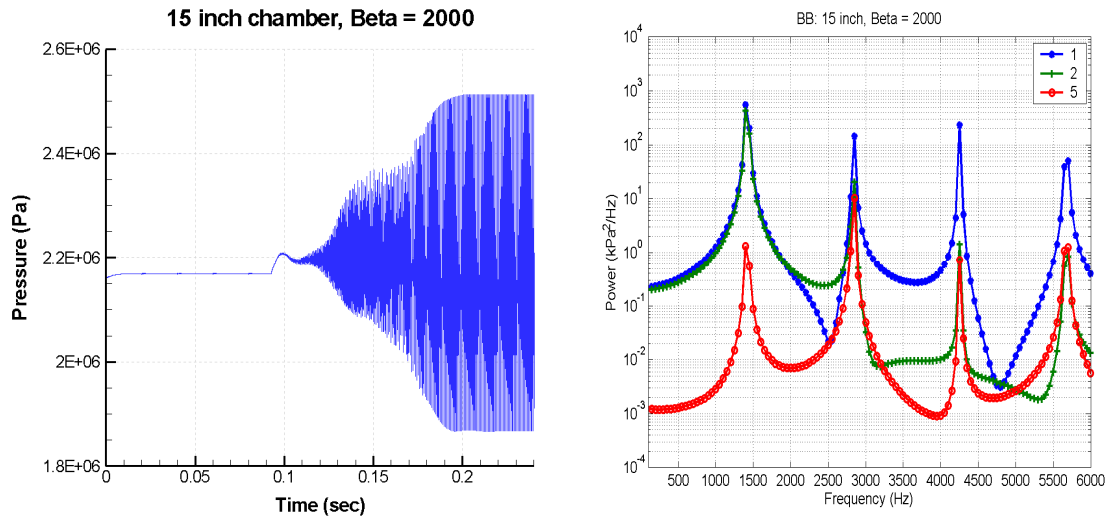


Figure 6.12: Pressure history plot (left) and PSD plot (right) for a 15 inch chamber and  $\beta = 2000$ . The unstable frequency is 1400 Hz.

The pressure trace and limit cycle PSD plot for the 20 inch chamber are shown in Figure 6.13.

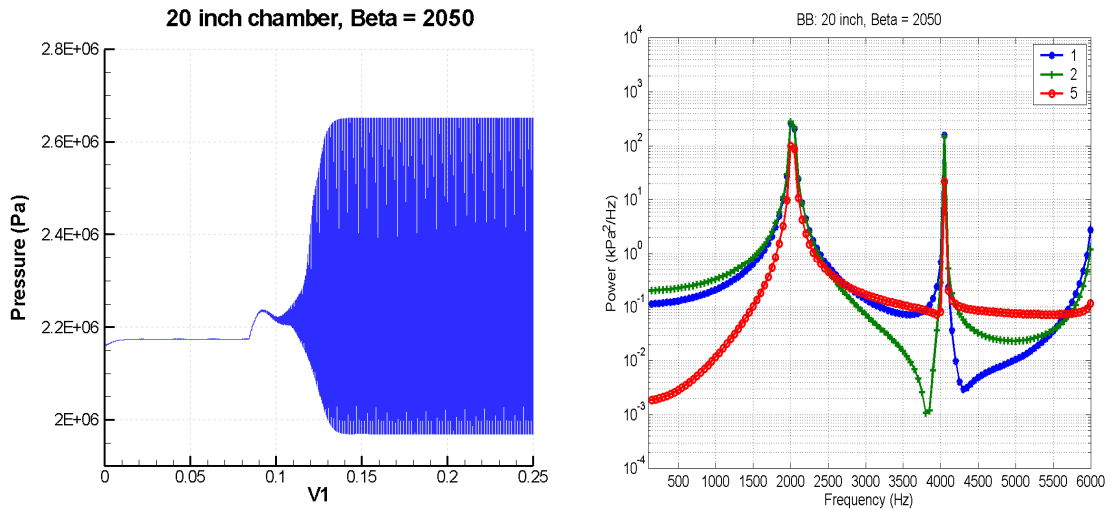


Figure 6.13: Pressure history plot (left) and PSD plot (right) for a 20 inch chamber and  $\beta = 2050$ . The unstable frequency is 2000 Hz.

The growth of the pressure oscillation occurs much more rapidly for the 20 inch case than for the 15 inch case. The limit cycle is developed in less than 0.06 seconds from the time the response function was applied. The 15 inch case required twice as long for a limit cycle to develop. Unlike the 15 and 25 inch cases, the 20 inch chamber case does not go unstable at same acoustic mode as the experiment. Instead it goes unstable at the next highest mode of 2000 Hz. Higher harmonic behavior is apparent in the PSD plot and there are also no small amplitude broadband peaks. The pressure trace and PSD plot at maximum growth for the 35 inch chamber are shown in Figure 6.14.

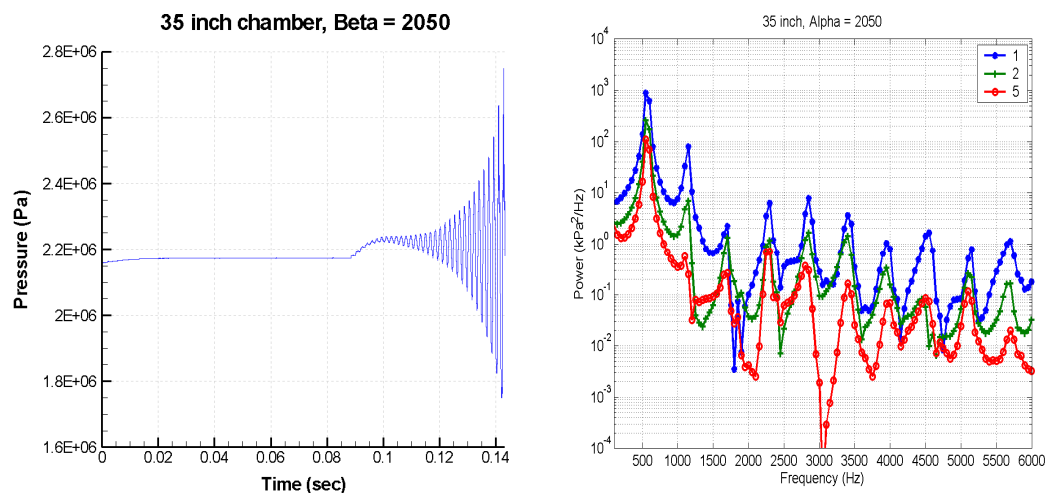


Figure 6.14: Pressure history plot (left) and PSD plot (right) for a 35 inch chamber and  $\beta = 2050$ . The unstable frequency is 550 Hz.

The pressure trace for the 35 inch chamber shows only growth without the development of a limit cycle, due to numerical divergence at all values of  $\beta$  that caused growth. The PSD plots shows instability at 550 Hz, which is different than the experiment. Because the unstable mode is the first mode, it is difficult to determine which peaks are higher harmonics and which are other modes.

#### 6.4. Instability Validation

The results of the previous section are now compared to the experimental PSD plots at position 2. These were obtained by first applying small amplitude, broadband forcing of the mass flow to simulate noise. Once a converged result was achieved, the mass flow forcing was turned off and the response function was activated by setting  $\beta$  to a non-zero value. For a  $\beta$  value of 2050 (or 2000 for the 15 inch case), all of the cases showed growth and the formation of a non-linear limit cycle except the 35 inch case. The computational and experimental PSD plots are shown side-by-side in Figure 6.15 for the 15, 20, and 25 inch cases and in Figure 6.16 for the 35 inch case (both early and late instabilities).

The 15 and 25 inch cases went unstable at 1400 Hz (1<sup>st</sup> chamber mode) and 1650 Hz (2<sup>nd</sup> chamber mode), which are the same unstable acoustic modes as the experiment. The 20 and 35 inch cases went unstable at 2000 Hz (2<sup>nd</sup> chamber mode) and 550 Hz (1<sup>st</sup> chamber mode), which are different from the unstable modes of the experiment. Note that the power peaks are much wider than the peaks of the large amplitude, single frequency forced results shown in Figure 4.17. This wider peak is most likely due to low amplitude acoustic modes (other than the unstable mode) which are present in the oscillating pressure signal. The results of CHAPTER 5 show a very narrow peak because only the forced frequency is present in the signal. The wider peak matches more closely with the experimental data.

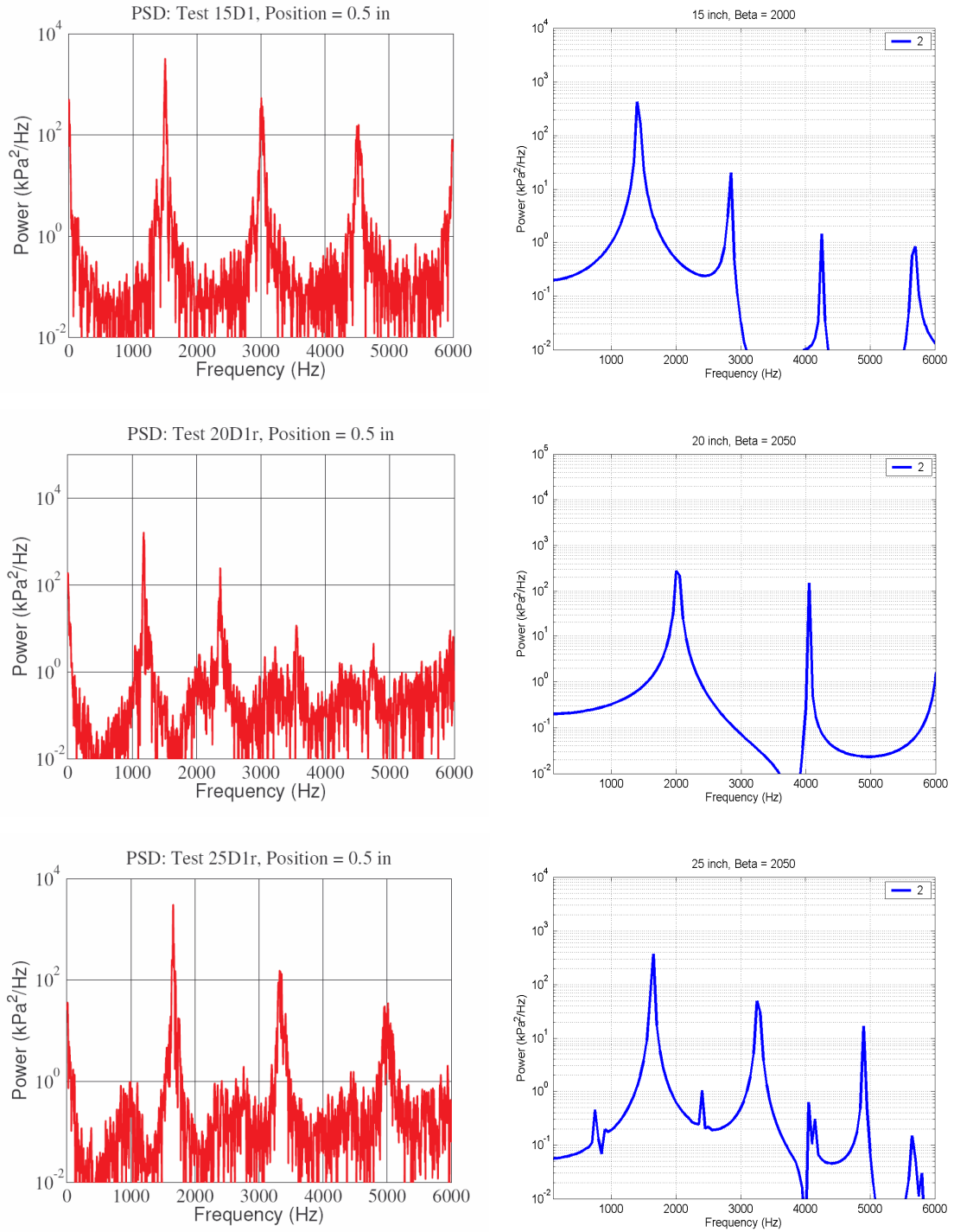


Figure 6.15: Experimental (left) and computational (right) PSD plots at position 2 for the 15, 20, and 25 inch cases. A response function was applied to the computational model to cause instability.



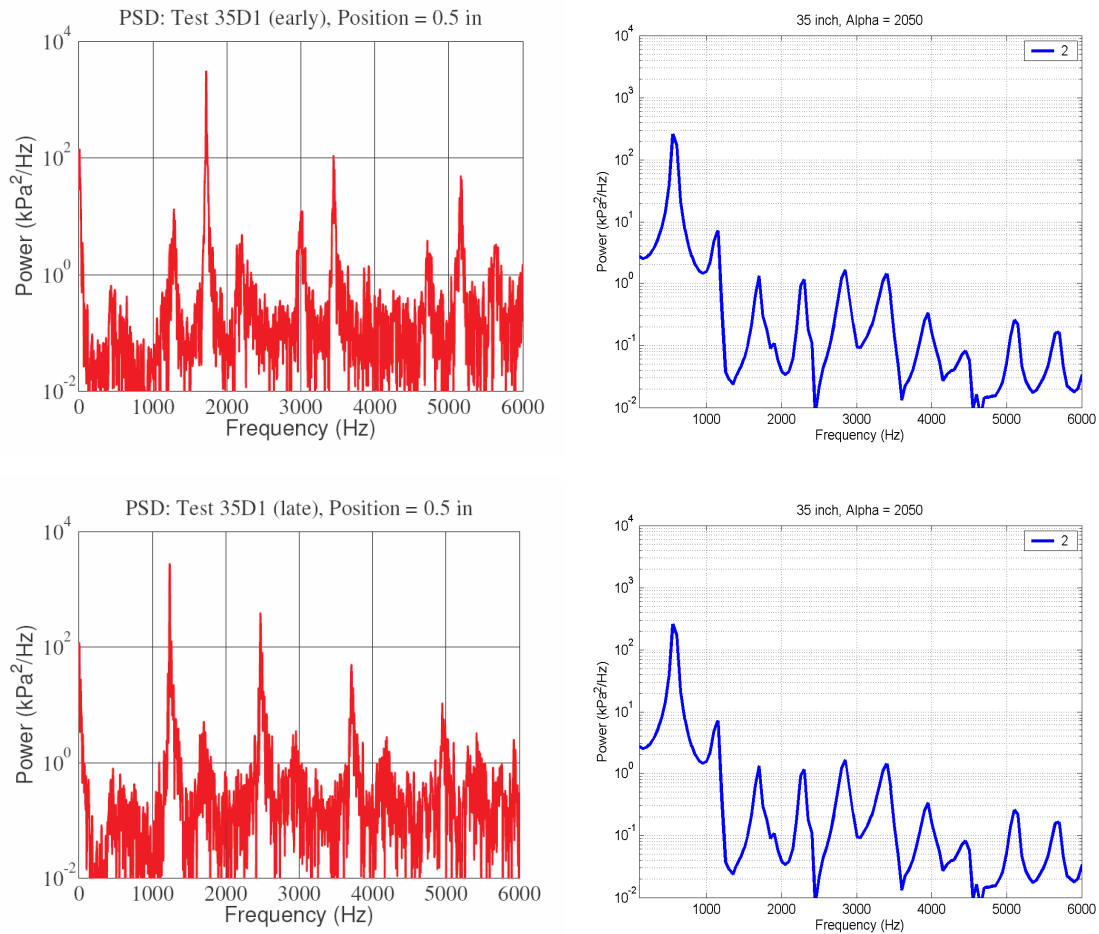


Figure 6.16: Experimental (left) and computational (right, repeated) PSD plots at position 2 for the 35 inch case. The experimental PSD plots show both the early and late instabilities. A response function was applied to the computational model to cause instability.

Although not performed in this thesis, it is speculated that using a more detailed heat release response function would change the unstable frequencies. A more representative response function would include a parameter that accounts for the phase relationship between the heat release and the dependent flow mechanism. It would also be modeled after a particular combustion mechanism, such as vortex shedding. Using response functions based on

different flow mechanisms may give an indication as to which mechanism has the largest impact on combustion instability.

The computational results for all of the chamber length cases show lower power amplitudes than the experimental data. This is due to the numerical divergence that occurs when a  $\beta$  value that is too large is applied. The code is terminated before the amplitude is able to increase to the experimental values. However, the  $\beta$  values are large enough for non-linear limit cycle behavior to develop.

## CHAPTER 7. SUMMARY AND CONCLUSIONS

### 7.1. Summary of Results

A one-dimensional CFD model was designed to investigate and simulate high frequency longitudinal combustion instability. The geometry and conditions of the model were based on a single-element liquid rocket engine experiment performed at Purdue which successfully produced spontaneous combustion instability over a range of frequencies. The computational model is based on the Euler equation and approximates steady combustion by using a single step reaction source term. Unsteady, broadband oscillations are introduced by oscillating the inlet mass flow-rate.

After verifying that the mean conditions were comparable to the experimental conditions, the mass flow was oscillated at small amplitude to investigate the acoustic behavior of the system. Using Fourier transform analysis, the acoustic modes of the system were determined from the oscillating pressure history. The code was first verified using a constant area duct geometry with cold flow. A simplified version of the computational model, containing only an injector and chamber with low Mach number flow, was then compared with an analytical model with similar geometry and no mean flow. The acoustic frequencies and mode shapes matched within 3.5% for all modes.

The full computational model was then employed in order to perform acoustic validation against the experimental data. The experimental unstable frequencies were matched by the computational results within 4% for each chamber length. The computational mode shapes showed fairly good agreement with the experimental data inside of the chamber, especially near the

injector/chamber interface. Also, Mach number effects on the acoustic modes were shown to be significant. Increasing the Mach number decreased the frequency of the mode while also changing the mode shape. This was shown in the injector region, where the Mach number was 0.38.

The mass flow forcing was increased to large amplitudes in order to simulate the non-linear behavior of the experiments. For each chamber length, the inlet mass flow was forced at the computational acoustic mode nearest to the unstable frequency shown in the experiments. For example, the 25 inch chamber was forced at 1650 Hz, which corresponded to the experimental unstable frequency of 1660 Hz. The maximum forcing that was used was 70% of the mean mass flow-rate. Above this value the code tended to diverge. Validation of the computational model was done by comparing the power spectral density (PSD) plots of the experiments and computations forced at 70% of the mean mass flow-rate at position two. The computational results compared well to the experimental results, showing the same non-linear behavior of higher harmonic excitation. The amplitudes of the computational power peaks were within an order of magnitude of the experimental results for all chamber lengths. The pressure history plots were also compared, showing similar wave steepening behavior in both. It was concluded that non-linear behavior similar to the experimental limit cycle oscillations could be simulated by applying the appropriate amount of forcing.

The boundary conditions of the original model were modified to test the accuracy of lower order models and to better match the experimental configuration. For these studies, the downstream nozzle was replaced by both a  $u' = 0$  (reflecting) condition and a short nozzle admittance condition. Broadband, small amplitude forcing with the approximate boundary conditions showed excellent agreement with the full nozzle configuration results. However, when the forcing was increased to large amplitudes, the solutions diverged significantly (especially for off-resonance frequencies). It was concluded that the application

of these approximate boundary conditions in analytical models is appropriate for linear analysis, but not for non-linear analysis.

The upstream boundary was also changed from an inflow to a wall boundary in order to match the experimental injector head-end boundary. This has an impact on the damping of the system, as waves are more fully reflected from a wall than an inflow boundary. Because of the one-dimensionality of the model, the flow could no longer be introduced at the inlet and thus had to be introduced through the use of an additional source term. This source term was added at the same axial location as the oxidizer in the experiment. By correctly defining this source term, the conditions in the chamber and nozzle matched the previous inflow boundary results while the conditions in the injector appeared to more closely represent the experimental flow conditions. This new wall boundary/oxidizer source configuration was then used for the rest of the instability studies.

Combustion instability was simulated through the use of basic response functions. The heat release was assumed to be exactly in phase with the pressure oscillations, which meant that only one parameter ( $\beta$ ) was necessary to define the relationship between heat release and pressure. Once a small amplitude converged pressure oscillation was established by forcing the mass flow at the unstable frequency (to simulate noise), the mass flow forcing was set to zero and  $\beta$  was set to a non-zero value. Depending on the size of  $\beta$ , the small amplitude pressure oscillation decayed, grew to a limit cycle, or caused the code to diverge.

For smaller values of  $\beta$ , the pressure oscillation decayed. This was attributed to the damping of the nozzle being greater than the amount of heat release of the response function. For larger values of  $\alpha$ , the pressure oscillations grew, eventually reaching a limit cycle if given enough time. The growth was attributed to the heat release being larger than the amount of damping of the system. The limit cycle is due to non-linear effects. This shows the capability of the computational model to simulate the general behavior of

spontaneous combustion instability. The divergence (when  $\beta$  is too large) is thought to be due to numerical instability.

The response function was also applied with initial broadband small amplitude noise. In all but one case, this resulted in the growth and development of a non-linear limit cycle. The resulting PSD analysis of the limit cycle region showed that in each case, a particular acoustic mode dominated the frequency response, similar to the experimental data. The computational model predicted the same unstable acoustic mode as the experiment in two of the four chamber length cases. The computational PSD plots showed higher harmonic excitation as before, but in some cases also showed smaller excitation of other acoustic modes. The distributions of the computational power peaks were also wider than the previous large amplitude, single frequency forced results of CHAPTER 5. This indicates that additional acoustic modes may be present other than just the unstable mode. Although the computational power peaks were somewhat lower in amplitude (by about an order of magnitude), the qualitative behavior was very similar.

## 7.2. Recommendations for Future Work

The next step in developing the computational model would be to extend the basic response function that was developed in CHAPTER 6. As discussed in the introduction, both amplitude and phase are influential in causing combustion instability. Therefore, another parameter should be added to the response function to account for the phase difference between the heat release and the pressure oscillations. A stability regime can then be determined for the amplitude and phase parameters. These parameters can be empirically determined from the experimental data, which would allow for direct and quantitative comparison between the computational and experimental results. Other parameters can also be varied, such as the location and width of the heat release, to determine the effect on stability. Methods of increasing the high amplitude forcing of the code

(so that divergence does not occur) may also be investigated in order to better match the amplitude range of the experimental data.

The response functions should be based on actual combustion heat release mechanisms (such as vaporization, atomization, mixing, etc.). For example, one mechanism that has been looked at in depth for longitudinal chambers is vortex shedding. The response model for this type of mechanism involves defining the heat release in terms of velocity instead of pressure. By modeling response functions after combustion mechanisms, the relative impact of that mechanism on instability can be determined. This would allow the computational model to become more useful as a tool for predicting combustion instability.

Modeling of response functions should be accompanied by higher order computational simulations. This involves using two or three-dimensional detailed unsteady dynamics computations to simulate the particular combustion mechanisms. In the case of vortex shedding, detailed simulations would be able to give the frequency of the shedding and an indication as to where most of the mixing occurs. These could be used as inputs for the phase and location of the response function. The simulations can help to guide and calibrate the development of these response functions. Continued experimental validation is also essential for accurate response function modeling.

## LIST OF REFERENCES

1. Sutton, G. P., and Biblarz, O., Rocket Propulsion Elements, 7<sup>th</sup> ed, John Wiley & Sons, New York, 2001.
2. Harrje, D. T., and Reardon, F. H. (eds.), *Liquid Propellant Rocket Combustion Instability*, NASA SP-194, Washington, D.C., 1972.
3. Oefelein, J. C., and Yang, V., "Comprehensive Review of Liquid-Propellant Combustion Instabilities in F1 Engines," *Journal of Propulsion and Power*, Vol. 9, No. 5, Sep-Oct 1993, pp. 657-677.
4. Smith, R., Nugent, N., Sisco, J., Xia, G., Anderson, W., Sankaran, V., Merkle, C. L., "Experimental and Computational Investigation of Combustor Acoustics and Instabilities, Part I: Longitudinal Modes," AIAA 2006-0537, 44<sup>th</sup> AIAA Aerospace Sciences Meeting and Exhibit, Reno, NV, January 2006.
5. Yang, V., and Anderson, W. E. (eds.), *Liquid Rocket Engine Combustion Instability*, AIAA, Washington, D.C., 1995.
6. Strutt, J. W., Lord Rayleigh, The Theory of Sound, Vol. 2, 2<sup>nd</sup> ed. Dover Publication, 1945.
7. Chu, B. T., "Stability of Systems Containing a Heat Source – The Rayleigh Criterion," NACA RM 56D27, Washington, D.C., June 1956.
8. Polifke, W., "Combustion Instabilities," VKI Lecture Series, "Advances in Acoustics and Applications," Brussels, Belgium, March 15-19, 2004.
9. Culick, F. E. C., and Yang, V., "Chapter 1: Overview of Combustion Instabilities in Liquid-Propellant Rocket Engines," in Yang, V, and Anderson, W. E., *Liquid Rocket Engine Combustion Instability*, AIAA, Washington, D.C., 1995.
10. Miller, K. J., "Experimental Study of Longitudinal Instabilities in a Single Element Rocket Combustor," M.S. Thesis, School of Aeronautics and Astronautics, Purdue Univ., West Lafayette, IN, May 2005.



11. Miller, K. J., Nugent, N., Sisco, J. and Anderson, W., Experimental Study of Combustion Instabilities In a Single-Element Coaxial Swirl Injector, 41<sup>st</sup> AIAA/ASME/SAE/ASEE Joint Propulsion Conference, Tucson, AZ, July, 2005.
12. Yang, V., Wicker, J. M., Yoon, M. W., "Chapter 13: Acoustic Waves in Combustion Chambers," in Yang, V., and Anderson, W. E., *Liquid Rocket Engine Combustion Instability*, AIAA, Washington, D.C., 1995.
13. Morse, P. M., Ingard, K. U., Theoretical Acoustics, McGraw-Hill, New York, 1968.
14. Sisco, J. C., Smith, R. J., Sankaran, V., Anderson, W. E., "Examination of Mode Shapes in an Unstable Model Rocket Combustor," 42<sup>nd</sup> AIAA/ASME/SAE/ASEE Joint Propulsion Conference, Sacramento, CA, July, 2006.
15. Culick, F. E. C., "Combustion Instabilities in Liquid-Fueled Propulsion Systems – an Overview," AGARD, CP-450, 1989.
16. Crocco, L., and Cheng, S-I, Theory of Combustion Instability in Liquid Propellant Rocket Motors, Butterworths, London, 1956.
17. Crocco, L., "Section 4.2: The Sensitive Time Lag Theory," in Harrje, D.T., and Reardon, F. H., *Liquid Propellant Rocket Combustion Instability*, NASA SP-194, Washington, D.C., 1972.
18. Portillo, J. E., Sisco, J. C., Corless, M. J., Sankaran, V., Anderson, W. E., "Generalized Combustion Instability Model," 42<sup>nd</sup> AIAA/ASME/SAE/ASEE Joint Propulsion Conference, Sacramento, CA, July, 2006.
19. Grenda, J. M., Venkateswaran, S., and Merkle, C., "Chapter 19: Application of Computational Fluid Dynamics Techniques to Engine Instability Studies," in Yang, V., and Anderson, W. E., *Liquid Rocket Engine Combustion Instability*, AIAA, Washington, D. C., 1995.
20. Habiballah, M., Dubois, I., "Chapter 18: Numerical Analysis of Engine Instability," in Yang, V., and Anderson, W. E., *Liquid Rocket Engine Combustion Instability*, AIAA, Washington, D.C., 1995.
21. Xia, G., Sankaran, V., Li, D., Merkle, C. L., "Modeling of Turbulent Mixing Layer Dynamics in Ultra-High Pressure Flows," AIAA 2006-3729, 36<sup>th</sup> AIAA Fluid Dynamics Conference and Exhibit, San Francisco, CA, June 2006.

22. Li, D., Xia, G., Sankaran, V., Merkle, C. L., "Computational Framework for Complex Fluids Applications," 3<sup>rd</sup> International Conference on Computational Fluid Dynamics, Toronto, Canada, July 12-16, 2004.
23. Sankaran, V., Xia, G., Ellis, M., Merkle, C. L., "CFD Simulations of Acoustic Wave Phenomena in Combustion Chambers," 3<sup>rd</sup> International Conference on Computational Fluid Dynamics, Toronto, Canada, July 12-16, 2004.
24. Li, D., Sankaran, V., Lindau, J., Merkle, C. L., "A Unified Formulation for Multi-Component and Multi-Phase Flows," AIAA-2005-1391, AIAA 43<sup>rd</sup> Aerospace Sciences Meeting and Exhibit, Reno, NV, January 10-13, 2005.
25. Ellis, M., Xia, G., Sankaran, V. and Merkle, C. L., "Acoustic Mode Simulations in Experimental Rocket Chambers," AIAA-2005-4300, 41<sup>st</sup> AIAA/ASME/SAE/ASEE Joint Propulsion Conference, Tucson, AZ, July, 2005.
26. Merkle, C. L., "AAE 512: Computational Aerodynamics," unpublished Purdue Course Lecture Notes, 2005.
27. Crocco, L., "Aspectos of Combustion Stability in Liquid Propellant Rocket Motors .1. Fundamentals – Low Frequency Instability with Monopropellants," *Journal of the American Rocket Society*, Vol. 21, No. 6, 1951, pp. 163-178.
28. Bloxsidge, G. J., Dowling, A. P., Langhorne, P. J., "Reheat Buzz: An Acoustically Coupled Combustion Instability. Part 2. Theory," *Journal of Fluid Mechanics*, Vol. 193, 1988, pp. 445-473.
29. Dowling, A. P., "A Kinematic Model of a Ducted Flame," *Journal of Fluid Mechanics*, Vol. 394, 1999, pp. 51-72.
30. Dowling, A. P., Stow, R. S., "Acoustic Analysis of Gas Turbine Combustors," *Journal of Propulsion and Power*, Vol. 19, No. 5, 2003, pp. 751-763.
31. Matveev, K. I., "Vortex-Acoustic Instability in Chambers with Mean Flow and Heat Release," *Electronic Journal, Technical Acoustics* [online database], URL: [HTTP://WEBCENTER.RU/~EEAA/EJTA](http://webcenter.ru/~eeaa/ejta) [cited 18 October 2004].

32. Smith, D. A., Zukoski, E. E., "Combustion Instability Sustained by Unsteady Vortex Combustion," AIAA-85-1248, 21<sup>st</sup> AIAA/ASME/SAE/ASEE Joint Propulsion Conference, Monterey, CA, July, 1985.
33. Sterling, J. D., Zukoski, E. E., "Longitudinal Mode Combustion Instabilities in a Dump Combustor," AIAA-87-0220, AIAA 25<sup>th</sup> Aerospace Sciences Meeting, Reno, NV, Jan, 1987.
34. Suresh, M., Jou, W., "Large-Eddy Simulations of Combustion Instability in an Axisymmetric Ramjet Combustor," *Combustion Science and Technology*, Vol. 75, 1991, pp. 53-72.
35. Ghoniem, A. F., Park, S., Wachsman, A., Annaswamy, A., Wee, D., Altay, H. M., "Mechanism of combustion dynamics in a backward-facing step stabilized premixed flame," *Proceedings of the Combustion Institute* 30, 2005, pp. 1783-1790.
36. Long, M. R., Bazarov, V. G., Anderson, W. E., "Main Chamber Injectors for Advanced Hydrocarbon Booster Engines," AIAA Paper No. 2003-4599.
37. Vasin, A., et al., United States Patent, US 6,244,041 B1, Jun. 12, 2001.
38. Figliola, R. S., and Beasley, D. E., Theory and Design for Mechanical Measurements, 3<sup>rd</sup> ed., John Wiley & Sons, New York, 2000.
39. Brigham, E. O., The Fast Fourier Transform, Prentice-Hall, New Jersey, 1974.
40. Heath, M. T., Scientific Computing, An Introductory Survey, 2<sup>nd</sup> ed., McGraw-Hill, New York, 2002.
41. Sirignano, W. A., "Section 3.6: Unsteady Flow in Exhaust Nozzles," in Harrje, D. T., and Reardon, F. H. (eds.), *Liquid Propellant Rocket Combustion Instability*, NASA SP-194, Washington, D.C., 1972.
42. Feller, W., An Introduction to Probability Theory and its Applications, Vol. 1, 3<sup>rd</sup> ed., Wiley, New York, 1968.
43. Turns, S. R., An Introduction to Combustion: Concepts and Applications, 2<sup>nd</sup> ed., McGraw-Hill, New York, 2000.
44. Van Loan, C. F., Computational Frameworks for the Fast Fourier Transform, SIAM, Philadelphia, 1992.

# Appendix A. Tabulated Acoustic Modes (for an Inflow BC)

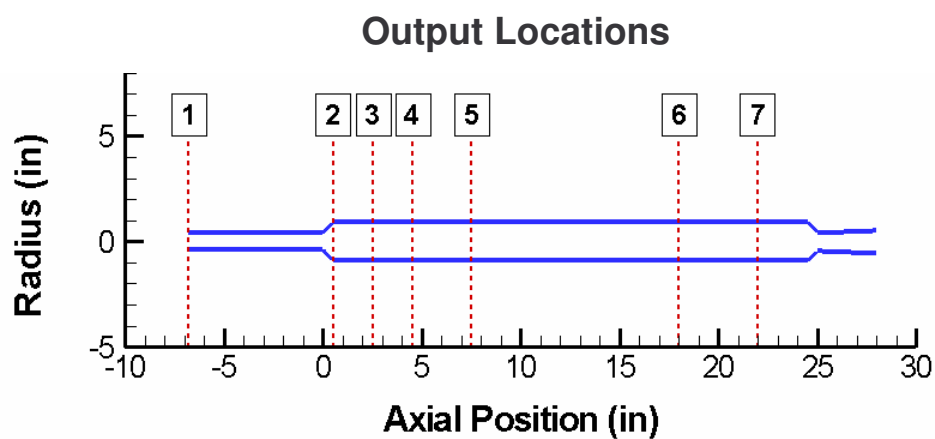


Figure A.1: Axial output locations for acoustic frequency analysis

Table A.1 Acoustic modes up to 7000 Hz for a 15 inch chamber with an inflow boundary condition. Output locations are specified in Figure A.1.

Mode	Output Location (All Frequencies in Hz)				
	1	2	3	4	5
1	800	850	—	750	750
2	1450	1400	1400	1400	—
3	2300	2300	2250	2300	2300
4	2800	2750	2750	2700	2750
5	3750	3800	3800	3800	3800
6	4200	4200	4200	4200	—
7	5150	5150	5150	5200	5150
8	5750	5700	5750	5750	5750
9	6500	6500	6500	6500	6500



Table A.4 Acoustic modes up to 7000 Hz for a 35 inch chamber with an inflow boundary condition. Output locations are specified in Figure A.1.

Mode	Output Location (All Frequencies in Hz)						
	1	2	3	4	5	6	7
1	500	550	600	600	600	—	550
2	800	—	750	800	800	800	—
3	1250	1200	1200	1200	1250	1200	1200
4	1700	1750	1750	1800	1750	1700	1750
5	2200	2250	—	2250	2250	2250	2250
6	2500	2450	2500	2500	2450	2500	2500
7	2950	2900	2950	2900	2900	2900	2900
8	3450	3450	—	3450	3500	3450	3450
9	3900	3950	3900	3950	3900	3900	3900
10	4200	4150	4200	4150	—	4150	4200
11	4650	4650	4600	4650	4600	4650	4650
12	5150	5150	5150	5200	5150	5150	5150
13	5600	5650	5600	5600	5550	—	—
14	5850	5850	5850	5850	5850	5850	5850
15	6350	6350	6350	6350	6300	6350	6350
16	6850	6900	6900	6850	6850	6900	6850

## Appendix B. Acoustic Analysis (for a Wall BC)

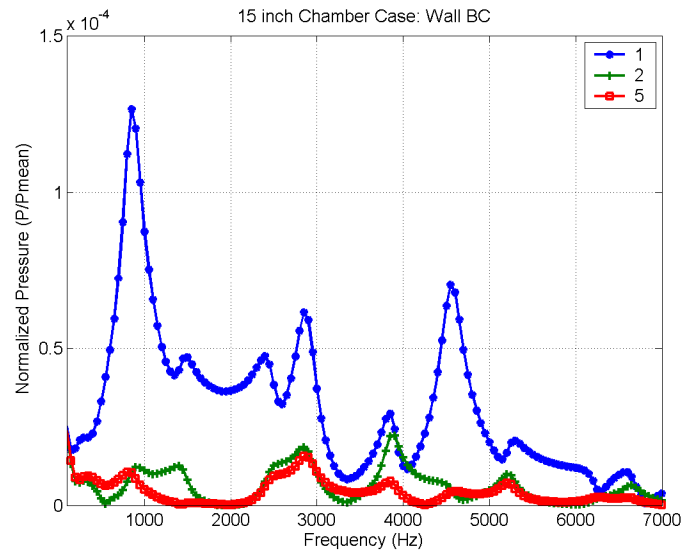


Figure B.1: FFT plot of the 15 inch chamber case forced with small amplitude, broadband mass-flow forcing. The upstream wall boundary condition is applied with an oxidizer source term.

Table B.1 Acoustic modes up to 7000 Hz for a 15 inch chamber with a wall boundary condition. Output locations are specified in Figure A.1.

Mode	Output Location (All Frequencies in Hz)				
	1	2	3	4	5
1	850	900	—	800	750
2	1500	1400	1400	1450	—
3	2400	—	—	2500	—
4	2850	2850	2900	—	2850
5	3850	3900	3800	3850	3850
6	4550	—	4550	4500	4600
7	5300	5200	5200	5250	5200
8	—	—	—	6250	6250
9	6600	6650	6650	6600	6600

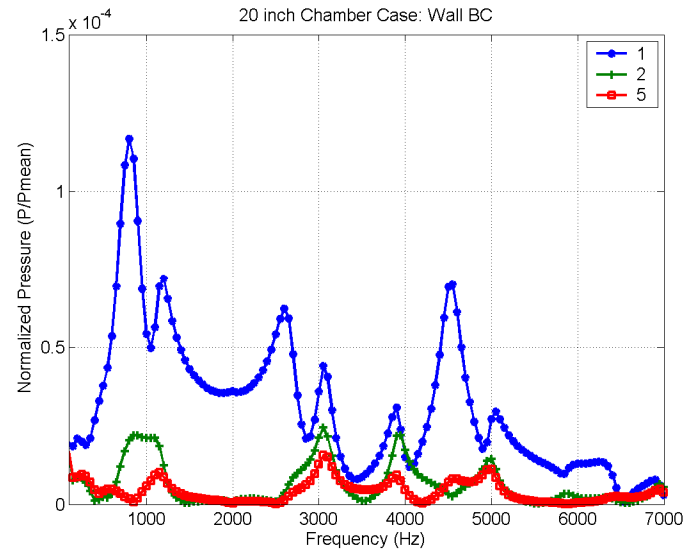


Figure B.2: FFT plot of the 20 inch chamber case forced with small amplitude, broadband mass-flow forcing. The upstream wall boundary condition is applied with an oxidizer source term.

Table B.2 Acoustic modes up to 7000 Hz for a 20 inch chamber with a wall boundary condition. Output locations are specified in Figure A.1.

Mode	Output Location (All Frequencies in Hz)					
	1	2	3	4	5	6
1	800	900	—	—	—	850
2	1200	1100	1100	1100	1150	1100
3	2000	—	—	—	—	—
4	2600	—	2650	2700	—	2700
5	3050	3050	3100	3050	3050	3050
6	3900	3950	3900	3900	3900	3900
7	4550	—	4550	—	4550	4500
8	5050	5000	4950	5000	5000	4950
9	—	5900	5850	5800	—	—
10	6250	6350	—	—	—	—
11	6900	6950	6950	6950	6950	6950



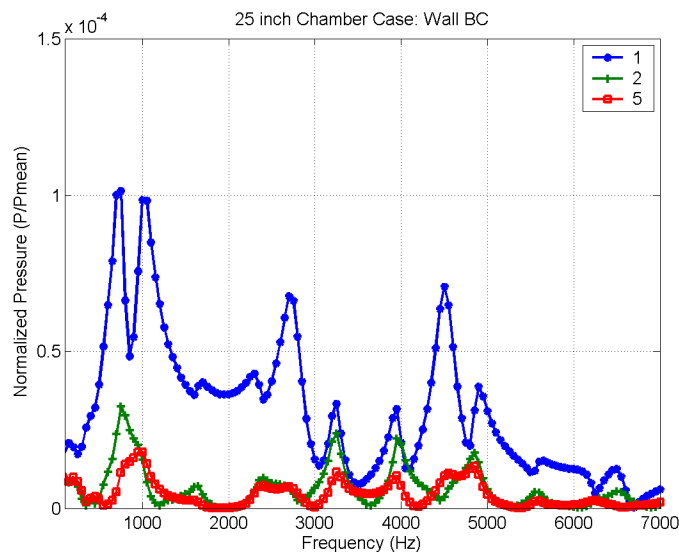


Figure B.3: FFT plot of the 25 inch chamber case forced with small amplitude, broadband mass-flow forcing. The upstream wall boundary condition is applied with an oxidizer source term.

Table B.3 Acoustic modes up to 7000 Hz for a 25 inch chamber with a wall boundary condition. Output locations are specified in Figure A.1.

Mode	Output Location (All Frequencies in Hz)						
	1	2	3	4	5	6	7
1	750	750	750	800	—	750	750
2	1000	—	—	950	1000	—	950
3	1700	1650	1650	1650	—	1650	1650
4	2300	2400	—	2350	2400	2400	2400
5	2700	—	2750	2800	2700	2750	2750
6	3250	3250	3300	3250	3250	3250	3250
7	3950	3950	3950	3950	3950	3950	4000
8	4500	—	4500	—	4550	—	4550
9	4900	4850	—	4850	4850	4850	4850
10	5650	5550	5550	—	5600	5550	5550
11	—	—	—	6250	6250	6250	6250
12	6500	6500	6500	—	—	6500	6550



## LIST OF REFERENCES

## APPENDICES